

MEMS PIEZORESISTIVE PRESSURE SENSOR ON FLEXIBLE SUBSTRATE
USING NICHROME AND CNT/POLYIMIDE NANOCOMPOSITES
AS PIEZORESISTORS

by

GAVIRAJ NADVI

Presented to the Faculty of the Graduate School of
The University of Texas at Arlington in Partial Fulfillment
of the Requirements
for the Degree of

MASTER OF SCIENCE IN ELECTRICAL ENGINEERING

THE UNIVERSITY OF TEXAS AT ARLINGTON

August 2010

Copyright © by Gaviraj Nadvi 2010

All Rights Reserved

ACKNOWLEDGEMENTS

I would like to express my sincere gratitude to my advisor Professor Donald Butler for his continuous direction, encouragement and support throughout my M.S. He patiently guided me with his excellent ideas and creativity which helped me getting the best out of my research.

I like to thank Dr. Zeynep Çelik-Butler, and Dr. Michael Vasilyev for taking part in my thesis committee. I am especially grateful to Dr. Zeynep Çelik-Butler for her valuable guidance and clever suggestions with any kind of problems I had in my research.

I am thankful to all Nanofab staff, especially Dr. Nader Hozhabri, Dennis Bueno and Eduardo Maldonado for their prompt attendance to equipment troubles no matter how busy they are.

I like to thank all my friends and co-workers in Nanofab, especially Bhargav, Rohit, Suraj, Erkin, Murali, Clement, Shahriar, Moinuddin, Iqbal, Mukti and Madhumita for the fruitful discussions we had and all their help. And also I would like to thank Erkin for designing masks which I used for the fabrication.

I would like express the most of my gratitude to my parents, my father Maregoud.S.N and my mother Geetha.S.N who have been a constant source of inspiration. Thank you all for your support.

July 16, 2010

ABSTRACT

MEMS PIEZORESISTIVE PRESSURE SENSOR ON FLEXIBLE SUBSTRATE USING NICHROME AS PIEZORESISTOR AND MICRO PRESSURE SENSOR USING CNT/POLYIMIDE NANOCOMPOSITES AS PIESORESISTIVE MATERIAL

Gaviraj Nadvi, M.S

The University of Texas at Arlington, 2010

Supervising Professor: Donald P. Butler

Micro pressure sensors using nichrome as piezoresistor were fabricated on silicon and flexible substrates. The pressure sensors on flexible substrate can be used for prosthetic skin applications. The devices were successfully tested using different methods.

Micromachined pressure/force sensors using nickel chromium piezoresistors have been investigated experimentally and through finite element mesh analysis. The pressure/force sensors were designed using a suspended aluminum oxide membrane with optimally placed piezoresistors to measure the strain in the membrane when deflected with an applied force or pressure. Different devices, each with varying size and shape of both the membrane and the piezoresistors were designed, fabricated, and characterized. The piezoresistors were placed into a Wheatstone bridge configuration with two active and two

passive nickel chromium resistors to provide temperature drift compensation. The measured results showed a 12% maximum change in resistance when the membrane is fully deflected from its original position due to the application of an applied load. Finally Gauge factor for thin film nichrome was found out using the combination of experimental and simulation results.

Nanocomposites using CNT and polyimide were developed for pressure sensing application which can be deposited using spin-coat method. Electrically conductive CNT/polyimide nanocomposites were achieved after depositing on the wafer using spin-coat method by varying the concentration of CNTs and polyimide. The deposited CNT/polyimide nanocomposites was patterned using the combination of RIE as well as liftoff technique to form the piezoresistive structure on top of the aluminum oxide membrane. The micro pressure sensor using CNT/polyimide nanocomposites as piezoresistor was fabricated and the individual resistance of the piezoresistor across Wheatstone bridge network was measured.

TABLE OF CONTENTS

ACKNOWLEDGEMENTS.....	iii
ABSTRACT.....	iv
LIST OF ILLUSTRATIONS.....	viii
LIST OF TABLES	xii
Chapter	Page
1. INTRODUCTION	1
1.1 Introduction to Micro-Electro-Mechanical Systems	1
1.2 Flexible Substrate	1
1.3 Pressure Sensors	2
1.4 Piezoresistivity	3
1.5 Polymer Nanocomposites	4
1.6 Carbon Nanotubes	4
2. DESIGN AND SIMULATION	6
2.1 Theory of Operation.....	6
2.2 Wheatstone-Bridge circuit	7
2.3 Design and Simulation.....	13
2.4 Procedure for Simulations	16
2.5 $\Delta R/R$ Calculation	24
2.6 Gauge Factor Calculations	26
2.7 Mask Layouts.....	33

3. FABRICATION AND CHARACTERIZATION OF PIEZORESISTIVE MEMS PRESSURE SENSOR USING NICHROME AS PIEZORESISTOR	44
3.1 Introduction	44
3.2 Fabrication	44
3.3 Oxidation of Nichrome	49
3.4 Sheet resistance	51
3.5 Characterization	53
3.6 Using Probe station	55
3.7 Using Load-cell	57
3.8 Results and discussion	59
4. PRESSURE SENSOR FOR PROSTHETIC SKIN APPLICATION	66
4.1 Introduction	66
4.2 Fabrication	67
4.3 Characterization	74
5. DEVELOPMENT OF MICRO PRESSURE SENSOR USING CNT/POLYMER NANOCOMPOSITES AS PIEZORESISTOR	84
5.1 Introduction	84
5.2 Methodology	84
5.3 Preparation of CNT/Nanocomposite	85
5.4 Fabrication	93
6. CONCLUSIONS	104
REFERENCES	105
BIOGRAPHICAL INFORMATION.....	109

LIST OF ILLUSTRATIONS

Figure	page
2.1 Top View of 3D model of Pressure Sensor	7
2.2 Wheat-stone Bridge Circuit.....	8
2.3 Boundary conditions for pressure sensor simulations.....	14
2.4 Piezoresistors at high strain region of displaced membrane.....	15
2.5 Mask layout for one of the pressure sensors, illustrating different layers used to create a 3-D model.....	17
2.6 Process flow for pressure sensor simulations.	18
2.7 Solid model of the some of the designed pressure sensors a) device T2 b) device T3 and c) device T4.	19
2.8 Meshed 3-D solid model of pressure sensor.	20
2.9 Mesher settings for the pressure sensor simulations. Extruded bricks with parabolic elements were used for simulations. Mesh size was kept as 2.5 μm	21
2.10 MemMech settings used for pressure sensor simulations.	22
2.11 Parametric study options where the boundary conditions were defined for pressure sensor simulations.	23
2.12 Surface boundary conditions for pressure sensor simulations.....	23
2.13 U and Y shaped piezoresistors. Different regions for strain calculations are shown.	24
2.14 Process flow to create a patch on top of the membrane for pressure sensor simulations.	27
2.15 Solid model of the some of the designed pressure sensors a) device T2 b) device T3 and c) device T4.....	28

2.16 Simulation results for membranes displaced by 5.4 μm to determine average strain on piezoresistors.....	29
2.17 Membrane mask to fabricate membrane structure.....	33
2.18 Piezoresistor mask to fabricate piezoresistors.	34
2.19 Metallization mask to create metal interconnects.....	34
2.20 Ashing cover mask to protect piezoresistors form getting oxidized during ashing.....	34
2.21 Membrane dimension for Device T1.....	35
2.22 Membrane dimension for Device T2.....	36
2.23 Membrane dimension for Device T3.....	37
2.24 Membrane dimension for Device T4.....	38
2.25 Membrane dimension for Device T5.....	39
2.26 Membrane dimension for Device B1.	40
2.27 Membrane dimension for Device B2.	41
2.28 Membrane dimension for Device B3.	42
2.29 Membrane dimension for Device B4.	43
3.1 Cross sectional view of the pressure sensor at different steps during the fabrication process.....	45
3.2 Membrane layer after the liftoff a) simulated b) fabricated.	46
3.3 Piezoresistive layer after the liftoff a) simulated b) fabricated.	47
3.4 Metallization contact layer after the liftoff a) simulated b) fabricated.	48
3.5 Top view of the 3D model of Pressure sensor and SEM image of Membrane suspended on the Polyimide layer after complete ashing.	49
3.6 Change in resistance of nichrome due to oxidation during ashing.....	50
3.7 Resistivity vs. thickness of nichrome deposited by rf magnetron sputtering.	52

3.8 Illustration of the setup to measure pressure sensor response.	54
3.9 Testing using Probe station setup.	56
3.11 Description of typical device types.	61
3.12 Load-cell result showing change in output voltage vs. pressure applied on the membrane for different types of devices.	63
3.13 Load-cell result showing change in output voltage vs. force applied on the membrane for different types of devices.	64
4.1 Membrane layer after liftoff.	68
4.2 Piezoresistive layer after nichrome liftoff.	69
4.3 Contact layer after aluminum liftoff.	70
4.4 SEM image showing the suspended membrane structure after ashing.	70
4.5 Device after peeling off from the silicon substrate.	71
4.6 picture of the live display on the screen during the membrane deflection a) before the membrane is deflected b) during the membrane deflection.	73
4.7 Typical plot showing liner I-V characterizations.	74
4.8 Description of the T3 device used for the characterization.	75
4.9 Description of the T4 device used for the characterization.	76
4.10 Load-cell result showing change in output voltage vs. pressure applied on the membrane for device T3.	80
4.11 Load-cell result showing change in output voltage vs. force applied on the membrane for device T3.	81
4.12 Load-cell result showing change in output voltage vs. pressure Applied on the membrane for device T4.	82
4.13 Load-cell result showing change in output voltage vs. force applied on the membrane for device T4.	83
5.1 PVDF pattern after 90 min. of RIE etch.	86

5.2 PVDF pattern after 120 min of RIE etch.	87
5.3 CNT/polyimide conductivity test at different areas of the sample	90
5.4 SEM images of device pattern in the increasing order of the magnification form top- left to bottom-right.	91
5.5 Chromium layer liftoff.	95
5.6 Aluminum oxide mask layer liftoff.	96
5.7 Confocal images of device sample at different areas on the sample showing different devices after 2 hours of RIE etch.	97
5.8 Another sample after 100 min. of RIE etch.	98
5.9 After 10 min of chromium etch used as liftoff technique.	99
5.10 After complete device fabrication.	100
5.11 IV curve of individual resistors of device 1.	102
5.12 IV curve of individual resistors of device 2.	103

LIST OF TABLES

Table	Page
2.1 Young's modulus and Poisson's ratio of different materials used for pressure sensors in this work.....	10
2.2 Actual gauge factor values calculated using measured $\Delta R/R$ for non-flexible devices. ..	30
2.3 Actual gauge factor values calculated using measured $\Delta R/R$ for non-flexible devices for 16nm thick piezoresistor.	31
2.4 Actual gauge factor values calculated using measured $\Delta R/R$ for non-flexible devices for 24nm thick piezoresistor.	31
2.5 Actual gauge factor values calculated using measured $\Delta R/R$ for non-flexible devices for 32nm thick piezoresistor.	32
2.6 Actual gauge factor values calculated using measured $\Delta R/R$ for flexible devices of device type T3.....	32
2.7 Actual gauge factor values calculated using measured $\Delta R/R$ for flexible devices of device type T4.....	33
3.1 Process details of photoresists that were used in pressure sensor fabrication.....	53
3.2 Average $\Delta R/R$ and Maximum $\Delta R/R$ for different types of devices which are tested using probe station.	60
3.3 Description and dimension of different types of devices fabricated	62
3.4 Sensitivity of the different devices which were characterized using Load-cell Measurement at two different regions which can be seen in the Figure 3.12 and Figure 3.13	65
4.1 Complete description of the T3 device characterized.	77
4.2 Complete description of the T4 device characterized.	79

CHAPTER 1

INTRODUCTION

1.1 Introduction to Microelectromechanical systems

Microelectromechanical systems (MEMS) are defined as devices with the combination of mechanical and electrical components that have the characteristic length of less than 1 mm but more than 1 micron which can be fabricated using integrated circuit batch fabrication techniques [1].

Some of the applications of MEMS devices are pressure sensors, accelerometers for automobile airbags, keyless entry systems, dense arrays of micro-mirrors for high definition optical displays, scanning electron microscope tips to image single atoms, micro heat exchangers for cooling of electronic circuits, reactors for separating blood cells, blood analyzers, microducts used in infrared detectors and diode lasers, micropumps used for ink jet printing and electronic cooling. Some of the applications of MEMS in medical field are lab-on-a-chip and development of artificial pancreas [1].

1.2 Flexible Substrate

Presently, most of the MEMS fabrication is done on rigid silicon substrates. The devices fabricated on silicon substrate have significant disadvantages due to mechanical problems associated with it such as non-conformality on host surface and fracture due to brittleness [2]. Recently there has been lot of interest in the fabrication of MEMS devices on flexible substrates due to its potential applications such as electronic textiles, smart tags, artificial skin and prosthetic devices [3]. The requirements for flexible substrates are that they

should be chemically inert, have high elastic modulus, comparable thermal expansion coefficients to the films formed on top, and they should also be electrically insulating [4].

So far device fabrication on flexible substrates has been done using three different types of substrates such as glass [5], polymer [6] and metal [7]. Thinned glass plate substrates are ideally suited for optical applications since they retain their optical properties after thinning but the disadvantage in using them is that they are difficult to handle due to their fragility and high cost. Device fabricated using metal foils as substrates are also good for optical applications as well as those requiring thermal and mechanical durability but the disadvantage in using them is that they are conductive and have high surface roughness and hence require insulating coatings as well as surface polishing. Polymers are flexible and also much cheaper but they are not suitable for high temperature processes [4].

1.3 Pressure Sensors

A pressure sensor is a device which is used to detect change in pressure. There are three different kinds of pressure measurements, namely absolute pressure, differential pressure and gauge pressure. Absolute pressure is measured relative to perfect vacuum. Differential pressure measures the pressure between two different points and gauge pressure is measured relative to atmospheric pressure. The same device can be used to measure different kinds of pressures [8].

Some of the common MEMS pressure sensors are capacitive pressure sensor and piezoresistive pressure sensor. In capacitive pressure sensors, change in the capacitance occurs when the gap between capacitor plates is changed due to pressure application where as in piezoresistive pressure sensors, there will be change in resistance due to strain induced on the piezoresistive material when pressure is applied on top of it. The advantages of piezoresistive pressure sensors are that they are easily fabricated with high linearity in the

sensitivity and the output signal is available in the form of voltage, making them ideal for the read-out mechanism. Some of the problems associated with piezoresistive pressure sensors are that they are highly sensitive to temperature. Capacitive pressure sensors on the other hand are less sensitive to temperature variations but some of the disadvantages are that they are electronically more complicated and need integrated electronics [9]. A good pressure sensor is the one with high sensitivity, good resolution, quick response to detect pressure changes and reproducibility [10].

1.4 Piezoresistivity

Piezoresistivity is a material property, where resistivity changes under an applied stress. It was first discovered in germanium and silicon by Smith [11] and Adams [12] in Bell Labs in 1954.

Both metals and semiconductors are known to have piezoresistive effect [13,14 and 15]. The resistivity of a material depends on its internal atom positions and their motions. Due to application of strain, these arrangements will change resulting in change in resistivity. For a metal, piezoresistive effect is suggested to be a result of dimensional change due to strain [16]. The change in dimension changes the inter-atomic positions resulting in distortion of energy bands slightly. Hence there will be small change in the amount of conduction when subjected to the applied electric field [16,17], whereas for a semiconductor strain gauge, it is proposed to be due to a change in carrier density related to shifting in band positions under applied stress [18].

1.5 Polymer Nanocomposites

Although the term nanocomposites represent new fields, such materials have actually been used for centuries and have always existed in nature. Some of the examples of such materials are bone, tooth and nacre which offer excellent mechanical properties compared to those of their constituent materials. However it is only in recent years that these materials have been used in a controlled method. If a composite material consists of at least one of the dimensions of one of its constituents in nanometer scale, then it is said to be nanocomposite material [19]. The mechanical properties become increasingly insensitive to flaws at nanometer scale which allows the usage of nanomaterial to provide the maximum theoretical strength of the material [20].

Carbon nanotubes (CNTs) have attracted particular interest due to their remarkable mechanical and physical properties. The combination of these properties with very low densities suggests that CNTs are ideal candidates for high performance polymer composites. CNTs are used as fillers in the polymer matrix due to its small size results in high-strength and high-stiffness polymer composites. Some of the challenges involved in usage of manufacture of polymer nanocomposites are in achieving a good dispersion of the nanoscale filler in the composite irrespective of filler shape and aspect ratio. Due to improper dispersion, filler aggregates tend to act as defect sites which limit the mechanical performance [22].

1.6 Carbon Nanotubes

CNTs have typical dimensions of 1 nm to 50 nm and lengths of many microns. They are made up of cylindrical structure made up of graphene sheet wrapped into one or more concentric cylinders. If a CNT is made up of one cylinder then that is called single-wall carbon nanotube (SWCNT). In SWCNT, a single graphene sheet is rolled in different

orientations along two-dimensional lattice which maps into circumference of the resulting cylinder and the orientation of the lattice defines chirality or helicity of the nanotube [21]. If a CNT is made up of two or more coaxial cylinders, each rolled out of single sheets of graphene, then those CNTs are called multi-wall carbon nanotube (MWCNTs). The outer diameter of MWCNTs typically varies between 2nm to 50nm [22].

CHAPTER 2

DESIGN AND SIMULATION

2.1 Theory of Operation

The design of micro piezoresistive pressure sensors extensively utilizes finite element mesh (FEM) analysis to predict the stress distribution to properly place the micro-piezoresistors to provide good sensitivity. T. Pancewicz et al. used FEM analysis to compare the output of the pressure sensor and with the experiment data [23]. Peng Chih-Tang et al also applied FEM analysis to evaluate the system output sensitivity of a pressure sensor [24]. The finite element method was used to simulate the stress distributions of different piezoresistor locations and piezoresistor arrangement pattern.

The piezoresistive pressure sensor is typically made up of three parts. The first part is the Membrane, which converts the pressure into mechanical strain. The second part is the piezoresistors, which convert the mechanical strain created by membrane into a resistance change. And finally this resistance change will be converted into differential output voltage by the Wheatstone bridge.

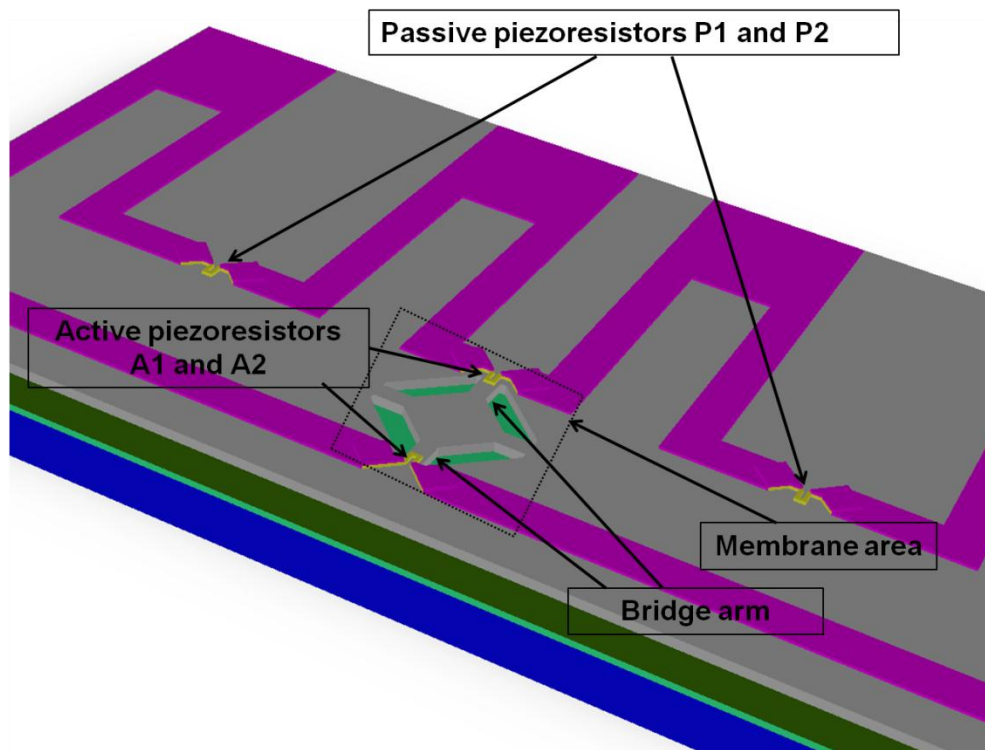


Figure 2.1 Top View of 3D model of Pressure Sensor

2.2 Wheatstone-Bridge circuit

The circuit diagram of a Wheatstone bridge is shown in Figure 2.2. Four resistors which are denoted as A1, A2, P1 and P2 correspond to the piezoresistors in a pressure sensor.

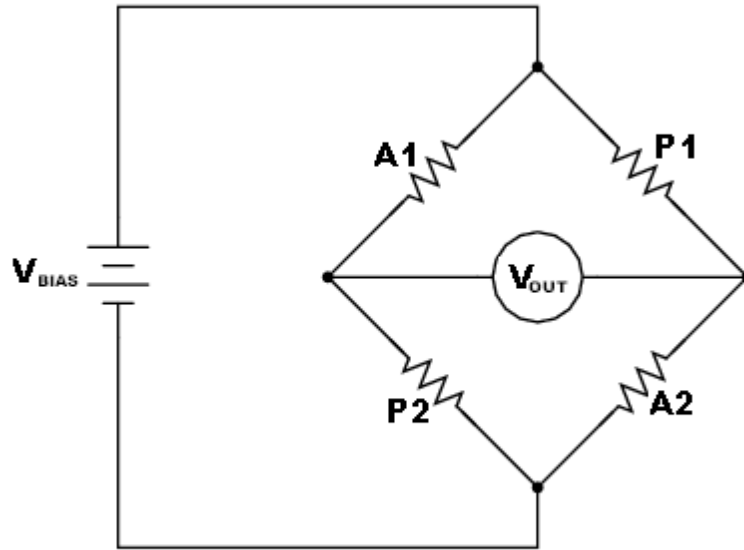


Figure 2.2 Wheat-stone Bridge Circuit

Where V_{BIAS} is the bias voltage given to the circuit and V_{out} is the output voltage measured across the Wheatstone bridge as shown in Eq. 2.1.

$$V_{out} = \left[\frac{P_2}{A_1 + P_2} - \frac{A_2}{A_2 + P_1} \right] V_{BIAS} = \frac{P_1 P_2 - A_1 A_2}{(A_1 + P_2)(A_2 + P_1)} V_{BIAS} \quad (2.1)$$

When the resistance of all the resistors in the Wheatstone bridge circuit is equal, then the voltage V_{out} will be zero. When there is a small change in the resistances of any of the resistor, then V_{out} will be nonzero and can be represented as shown in Eq. 2.2

$$V_{out} + \Delta V_{out} = \frac{(P_1 + \Delta P_1)(P_2 + \Delta P_2) - (A_1 + \Delta A_1)(A_2 + \Delta A_2)}{(A_1 + \Delta A_1 + P_2 + \Delta P_2)(A_2 + \Delta A_2 + P_1 + \Delta P_1)} V_{BIAS} \quad (2.2)$$

Where ΔV_{out} is change in output voltage; ΔA_1 , ΔA_2 , ΔP_1 and ΔP_2 are change in resistances of A1, A2, P1 and P2 respectively.

A typical structure of membrane based piezoresistive pressure sensor is shown in Figure 2.1. Here the piezoresistors are connected in the Wheatstone bridge fashion, where each resistor is made-up of piezoresistive material and are connected to each other with the conductive metal lines. As the pressure is applied on the membrane, the membrane will deflect and there will be a change in the stress across the bridge arms. The stress change in the bridge arm of membrane causes the resistance of the piezoresistors to change. As shown in Figure 2.1, two resistors which are present on the suspended portion of the membrane are called active piezoresistors A1 and A2. These resistors are called active because they change their resistance when the pressure is applied on the membrane. The other two resistors are passive piezoresistors P1 and P2, which are present far away from the membrane area and hence do not change their resistance value when the pressure is applied on the membrane and therefore $\Delta P_1 = \Delta P_2 = 0$. Hence the Eq. 2.2 can be written as shown in Eq. 2.3.

$$V_{out} + \Delta V_{out} = \frac{P_1 P_2 - (A_1 + \Delta A_1)(A_2 + \Delta A_2)}{(A_1 + \Delta A_1 + P_2)(A_2 + \Delta A_2 + P_1)} V_{BIAS} \quad (2.3)$$

Four different materials were used in modeling the sensor structures. Aluminum oxide and nichrome were chosen as the membrane layer and the piezoresistive material, respectively. All materials were assumed to be linear, elastic and isotropic. Aluminum was used as the metallization layer connecting the Wheatstone-bridge resistors. The material

data such as the Young's modulus, and Poisson's ratio and layer thicknesses used for simulations are listed in Table 1. Aluminum oxide is attractive for MEMS structures and was selected here as the membrane material due to its robustness over a large temperature range. Aluminum oxide is a linear material until it reaches its maximum stress or its yield strength which is around 15.4 GPa. [29]

Table 2.1 Young's modulus and Poisson's ratio of different materials used for pressure sensors in this work [25,26,27,28,29,30, 31].

Material	Young's modulus (Gpa)	Poisson's ratio	Thickness (μm)
Silicon nitride	304	0.24	0.4
PI2611 (sacrificial polyimide)	7.5	0.35	4
Alumina	344.83 to 408.99	0.21 to 0.27	1.2
Nichrome	18.6	0.38	0.016 to 0.032
Aluminum	30	0.33	0.3

CoventorWare® CAD tool was used to design and simulate the different pressure sensors based on the different size and shape of both the membrane and the piezoresistor. The model was meshed with extruded bricks, and mesh size was changed iteratively to achieve convergence. Finite-element analysis (FEA) was performed on the three-dimensional model after applying required boundary conditions. All degrees of freedom were constrained on the patch while a pressure from 0 to 100 kPa was applied uniformly in steps of 10 kPa on the top surface of the membrane. The maximum stress and maximum membrane displacement were noted. By knowing the displacement of the membrane, we can estimate the trench thickness needed beneath the membrane to support the membrane

from breaking when the applied pressure is greater than 1 Mpa. The thickness of the sacrificial layer was thereby determined to be 1.2 μ m.

During the simulation a uniform normal pressure of 0 to 100 kPa was applied on top of the membrane and parameters such as maximum stress, strain and membrane displacement were obtained. Then $\Delta R/R$, the relative change in the resistance due to pressure, and ΔV , the Wheatstone bridge differential output voltage for $V_{BIAS} = 1V$ were calculated. To obtain the strain values from the piezoresistor, a local coordinate system was implemented in CoventorWare®. The total strain obtained was then divided by the total area of the piezoresistor to obtain average strain (ϵ_{AVG}). [32]

$$\epsilon_{AVG} = \frac{\epsilon_{total}}{A} = \frac{\iint [\epsilon_x + \epsilon_y] dxdy}{\iint dxdy} \quad (2.4)$$

Where, ϵ_x is the transverse strain, ϵ_y is the longitudinal strain, ϵ_{total} is the total strain and A is the area of the piezoresistor. A gauge factor (GF) of 2.8 was assumed for Nichrome in the case of our simulations [33]. $\Delta R/R$ was then obtained using,

$$\frac{\Delta R}{R} = \epsilon_{AVG} * GF \quad (2.5)$$

When the applied pressure is zero, ideally the half-Wheatstone bridge is balanced with the output voltage V_{out} is taken to be V_1 and given by,

$$V_{out} = V_1 = \left[\frac{P_2}{A_1 + P_2} - \frac{A_2}{A_2 + P_1} \right] * V_{BIAS} \quad (2.6)$$

Here, P_1 , A_1 , P_2 and A_2 are the resistances of the four piezoresistors. In our design, all the four resistors are assumed to have the same values. When pressure or force is applied to the sensor, the output voltage changes and is taken as V_2 and calculated using the formula;

$$V_{out} = V_2 = \frac{(P_1 + \Delta P_1)(P_2 + \Delta P_2) - (A_1 + \Delta A_1)(A_2 + \Delta A_2)}{(A_1 + \Delta A_1 + P_2 + \Delta P_2)(A_2 + \Delta A_2 + P_1 + \Delta P_1)} V_{BIAS} \quad (2.7)$$

In the calculation, V_{BIAS} was chosen as 1 V. ΔP_1 , ΔA_1 , ΔP_2 and ΔA_2 are the changes in resistances resulting from the deformation of each resistor. The sensor area which deforms due to the applied normal pressure is referred to as the active area, shown in Figure 2.1. In our case, resistors A_1 and A_2 are called active resistors that lie within the active area and deform due to the normal pressure applied. This deformation induces strain within the piezoresistor resulting in the resistance change. Since the resistors P_1 and P_2 lie outside the active area and therefore do not change their resistance when the pressure is applied on the membrane, so $\Delta P_1 = \Delta P_2 \approx 0$. Then the Eq. 2.7 can be modified as Eq. 2.8.

$$V_{out} = V_2 = \frac{P_1 P_2 - (A_1 + \Delta A_1)(A_2 + \Delta A_2)}{(A_1 + \Delta A_1 + P_2)(A_2 + \Delta A_2 + P_1)} V_{BIAS} \quad (2.7)$$

Assuming change in resistor ΔA_1 and ΔA_2 are equal, the Eq. 2.8 can be written as,

$$V_{out} = V_2 = \frac{P_1 P_2 - (A_1 + \Delta R)(A_2 + \Delta R)}{(A_1 + \Delta R + P_2)(A_2 + \Delta R + P_1)} V_{BIAS} \quad (2.8)$$

Where $\Delta R = \Delta A_1 = \Delta A_2$

The change in output voltage ΔV due to load application on the membrane is calculated using Eq. 2.10

$$\Delta V = V_2 - V_1 \quad (2.9)$$

2.3 Design and Simulation

CoventorwareTM has been used to design, optimize and analyze various pressure sensors through finite element analysis. Initially two dimensional layouts were created, which were then transferred to three dimensional solid models through a process flow. Ten pressure sensor structures composed of square membranes were created each varying in size and shape of membrane as well as piezoresistor shape and size. Each membrane was supported by four bridge arms on the corners, housing two piezoresistors in a half Wheatstone bridge configuration. As seen in Figure 2.1, the area below the membrane called sacrificial layer is removed isotropically from the edges of trenches.

Extruded bricks were used for meshing during the simulations and the mesh size was changed iteratively to achieve convergence. As the name indicates, for the extruded brick, first the meshing is applied on the x and y axis and then extended into z axis.

Simulations were performed using MemMech module of CoventorwareTM by applying uniform pressure of 0 to 100 kPa on top of whole surface after meshing and constraining the sides of the membrane as shown in Figure 2.3. During the simulation, the amount of membrane displacement was in proportion to the amount of load applied on top of the membrane. By knowing the displacement of the membrane, the optimum amount of trench thickness needed for the fabrication were determined so that it can support the membrane from braking due to a sudden increase in load.

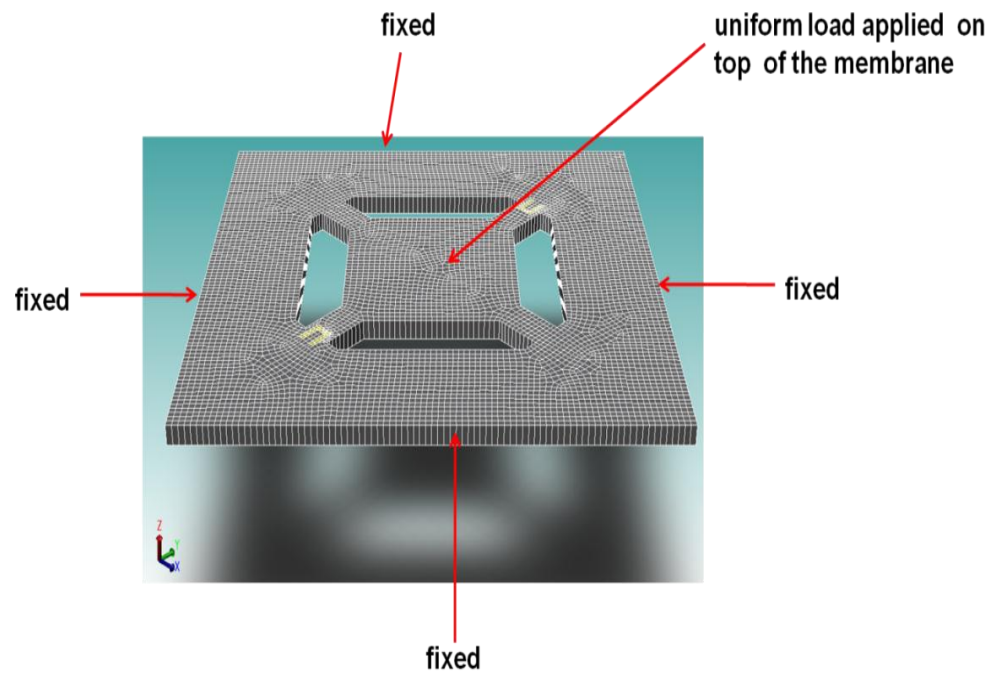


Figure 2.3 Boundary conditions for pressure sensor simulations.

High strain regions where the

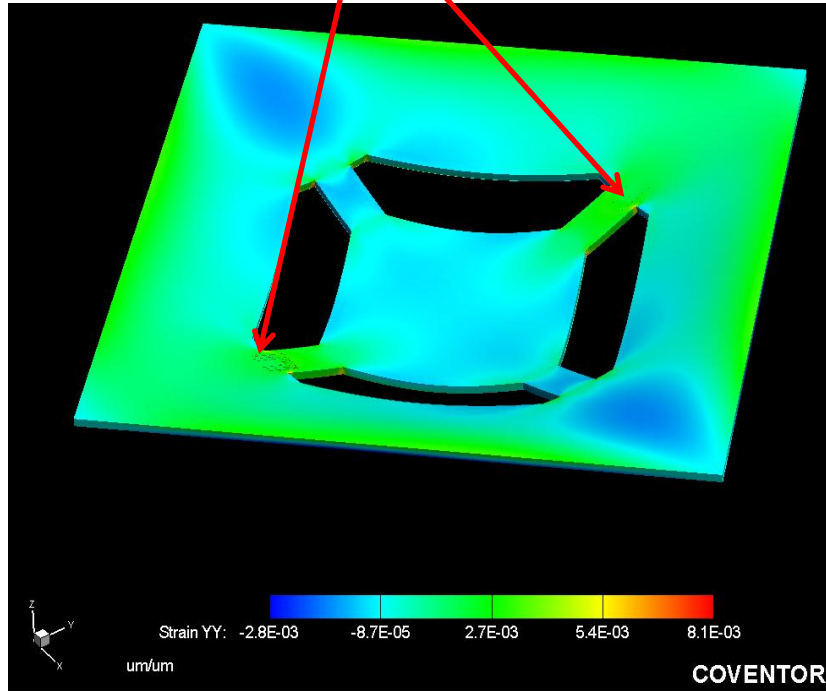


Figure 2.4 Piezoresistors at high strain region of displaced membrane.

After the simulations, post simulation calculations were performed to find values such as average strain, $\Delta R/R$ and ΔV_{out} . To calculate average strain, U-shaped piezoresistors were divided into three regions and Y-shaped piezoresistors were divided into five regions to calculate transverse (ϵ_{xx}) and longitudinal (ϵ_{yy}) strains. Axis transformation was applied for Y-shaped piezoresistors using Eq. 2.11.

$$\epsilon_x = \epsilon_{xx} \cos^2 \theta + \epsilon_{yy} \sin^2 \theta + \gamma_{xy} \sin \theta \cos \theta \quad (2.10)$$

where, ε_{xx} , ε_{yy} and γ_{xy} are transverse, longitudinal and shear strains respectively. The angle θ is the angle between the transferred axis and the global axis. Using the strain data, the average strain was calculated using Eq. 2.12.

$$Strain_{AVG} = \frac{Strain_{total}}{Area_{total}} = \frac{\iint [\varepsilon_{xx} + \varepsilon_{yy}] dxdy}{\iint dxdy} \quad (2.11)$$

Using the calculated average strain value, the normalized change in resistance was found assuming a gauge factor (GF) of 2.8 for nichrome [33] and using

$$\frac{\Delta R}{R} = Strain_{AVG} * GF \quad (2.12)$$

2.4 Procedure for Simulations

For the design, first a layout was designed with the actual planned sizes as shown in Figure 2.5. The layout consisted of four layers, namely a substrate mask, a sacrificial polyimide mask for undercut, a membrane mask to define membrane area and piezoresistor mask to define piezoresistors.

Next, a process flow was created. In the process flow, type of layer depositions, layer thicknesses, resist polarity and masks to pattern deposited layers were defined. A process layer for the layout, given in Figure 2.5. is shown in Figure 2.6.

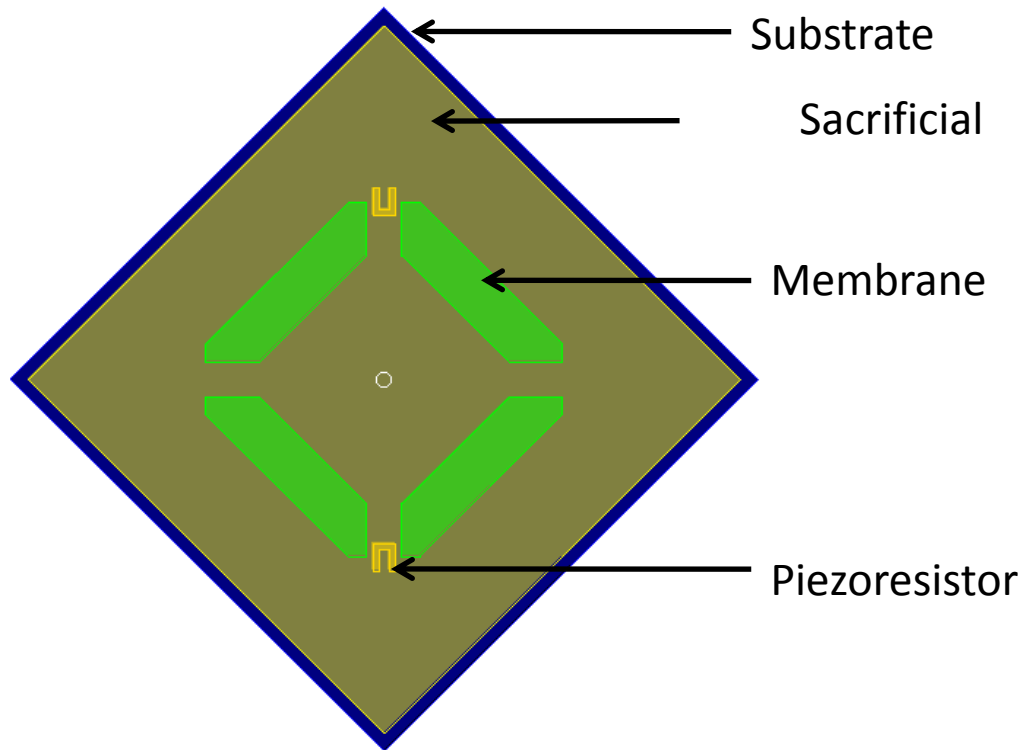


Figure 2.5 Mask layout for one of the pressure sensors, illustrating different layers used to create a 3-D model.


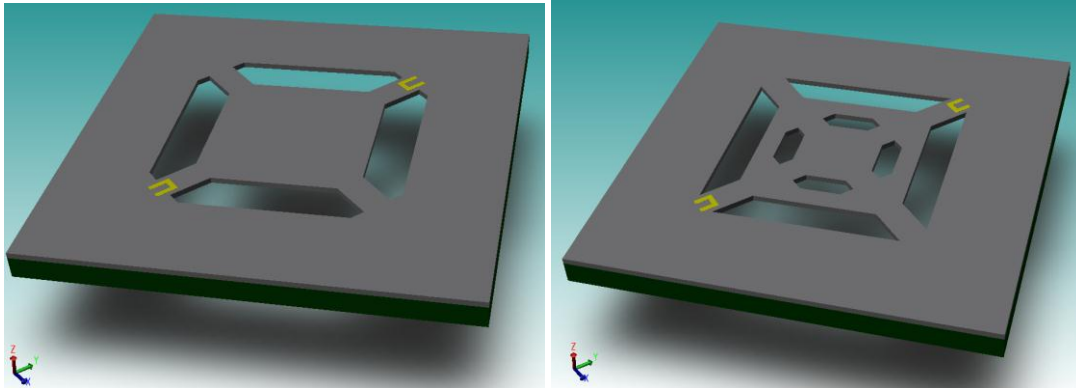
File Edit View Tools Windows Help				
				
Number	Step Name	Layer Name	Material Name	Thickness
0	Substrate	Substrate	SILICON	40
1	passivation layer	passivation	SI3N4	0.4
2	sacrificial polyimide	polyimide layer	POLYIMIDE	5.4
3	Stack Material	Membrane	AL2O3	1.4
4	Conformal Shell	piezoesistors	NICHROME	0.02

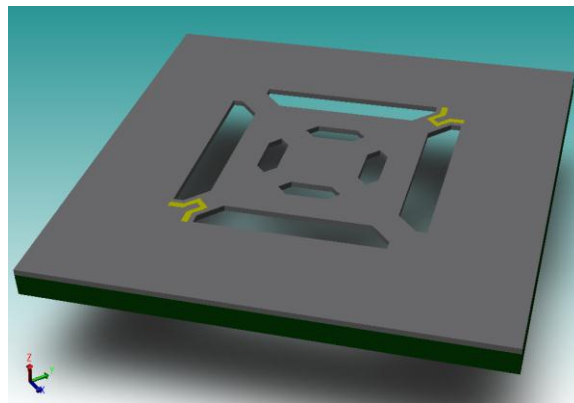
Figure 2.6 Process flow for pressure sensor simulations.

By the combination of the layout and process file, a 3-D solid model was created as shown in Figure 2.7.



a)

b)



c)

Figure 2.7 Solid model of the some of the designed pressure sensors a) device T2 b) device T3 and c) device T4.

Next, the layers that are necessary for simulation were transferred into mesh model and meshed using extruded brick with a mesh size of $2.5 \mu\text{m}$. The meshed 3-D model and meshing parameters are given in Figure 2.8 and Figure 2.9 respectively. After meshing, the boundaries that will be used during simulations are defined. All sides of the membrane in the

model were fixed and the entire top surface of the membrane was selected for pressure application. An illustration of the boundary conditions is given in Figure 2.3.

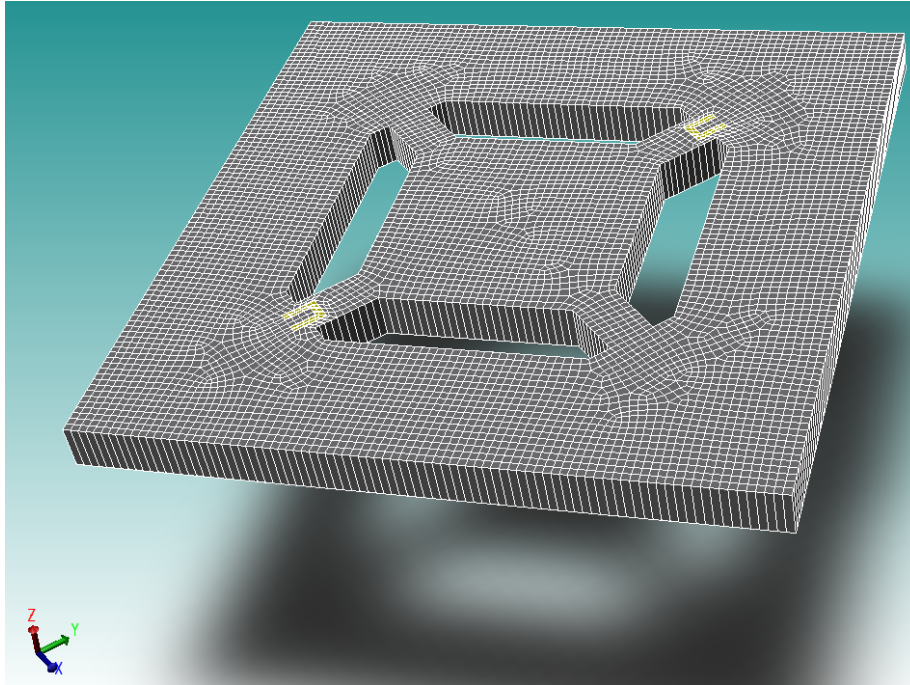


Figure 2.8 Meshed 3-D solid model of pressure sensor.

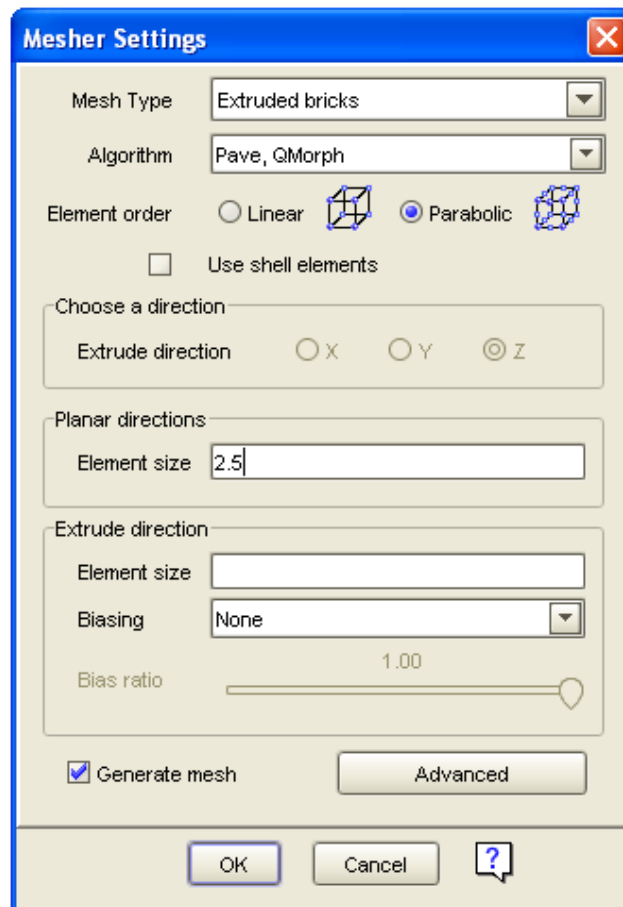


Figure 2.9 Mesher settings for the pressure sensor simulations. Extruded bricks with parabolic elements were used for simulations. Mesh size was kept as 2.5 μm .

For simulations, MemMech module of Coventorware™ was used. In the module settings, mechanical analysis was selected. Simulations were done assuming linear and steady state properties. No additional analysis was selected. An image of the settings window is given in Figure 2.10.

After settings, in the parametric study options, surface boundary conditions were selected to define the amount of load applied on the top surface of membrane as shown in Figure 2.11. For membrane deflection, surface boundary conditions were used by fixing all sides denoted as fixed and applying 0.1 MPa, which is the default unit, to the top. Surface boundary conditions are shown in Figure 2.12.

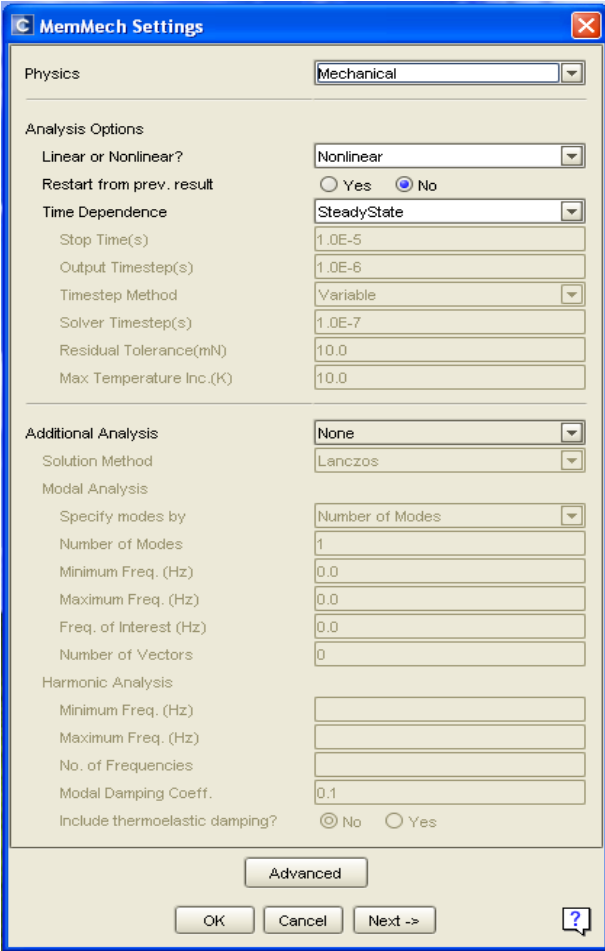


Figure 2.10 MemMech settings used for pressure sensor simulations.



Figure 2.11 Parametric study options where the boundary conditions were defined for pressure sensor simulations.

SurfaceBCs	FixType	Patch1	and1	Patch2	and2	Patch3	LoadValue	Variable	Transient
Set1	fixAll	Fixed	and	none	and	none	Scalar 0.0	Fixed	Fixed
Set2	LoadPatch	Top	and	none	and	none	Scalar 3	Fixed	Fixed
Set3	none	none	and	none	and	none	Scalar 0.0	Fixed	Fixed
Set4	none	none	and	none	and	none	Scalar 0.0	Fixed	Fixed

Figure 2.12 Surface boundary conditions for pressure sensor simulations.

2.5 $\Delta R/R$ Calculation

After the simulations, average strain was calculated using Eq. 2.12. Simulation results were used to find strain values, ϵ_{xx} and ϵ_{yy} . U shaped piezoresistors were divided into three regions, while Y shaped ones were divided into five regions. The images of piezoresistors are given in Figure 2.13.

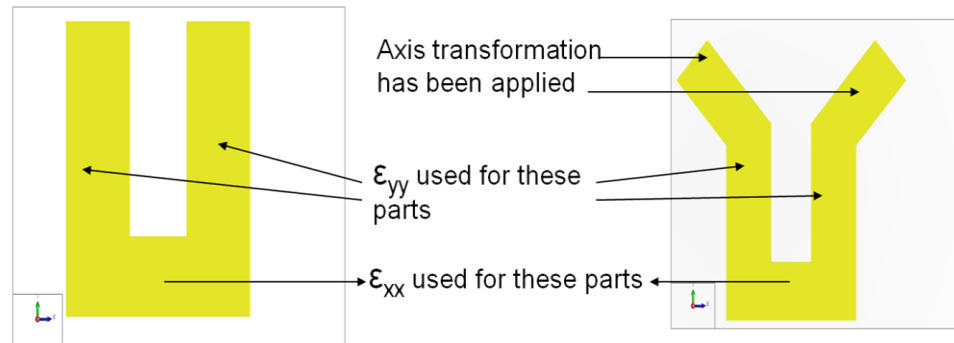


Figure 2.13 U and Y shaped piezoresistors. Different regions for strain calculations are shown.

Using point extraction, at least 200 data points were extracted from each region in the form of a text file. Then, these text files were converted into excel files. Using the following Matlab™ code and excel file data, average strain and total area of the piezoresistor were calculated.

```
% reads an excel file and extracts useful data to plot
% also reads the data headers that precede the data

%reading the xls file (in the same directory)
[raw_data,header_info] = xlsread('t4_strain_xy_y.xls')

%data in the xls file is arranged as
% Col 3, Col 4, Col 2
% X      Y      strain
X=raw_data(:,1); %column 1
Y=raw_data(:,2); % column 2
```

```

strain=raw_data(:,3); % column 3

mydata = [X Y strain];

minX=min(X); minY=min(Y);
maxX=max(X); maxY=max(Y);

% Define the grid density
m=200;% No. of rows
n=200;% No. of columns

% Make a X x Y grid, called [Xi,Yi]
x1 = linspace(minX,maxX,n);
y1 = linspace(minY,maxY,m);
[Xi,Yi] = meshgrid(x1,y1);

%map mag on to the grid
straini=griddata(X,Y,strain,Xi,Yi);

%generate the mesh plot or just the contours
%[C,h]=contour(y1,z1,magi), title('Device 1b4 Area Scan 8'),...
mesh(x1,y1,straini), title('Plot of strain_y as a function of X and Y'),...
xlabel('x (microns)'),ylabel('y (microns)'),zlabel('Strain_Y');
%set(axes_handle,'YGrid','on')
%clabel(C,h);
view([-37.5,30]);

minstr = min(min(straini));
maxstr = max(max(straini));
TotalStr = 0;
TotalArea = 0;
for i = 1:199
    for j = 1:199
        if mean(straini(i:i+1, j:j+1)) >= minstr & mean(straini(i:i+1, j:j+1)) <= maxstr
            TotalStr = TotalStr + mean(straini(i:i+1, j:j+1)) * (Xi(i, j+1) - Xi(i, j)) * (Yi(i+1, j) - Yi(i, j));
        end
        TotalArea = TotalArea + (Xi(i, j+1) - Xi(i, j)) * (Yi(i+1, j) - Yi(i, j));
    end
end
TotalArea
TotalStr

```

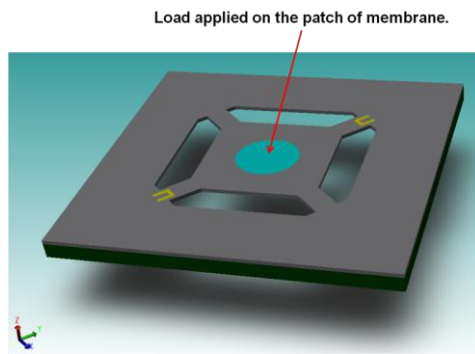
2.6 Gauge Factor Calculations

Gauge factors of measured samples were calculated using probe station measurement results in combination with simulations.

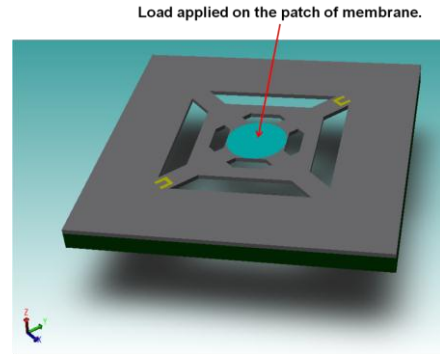
During the device characterization using probe station, the membrane was fully displaced, which corresponds to a distance of 5.4 μm . Using CoventorwareTM, computer models of measured samples were displaced by 5.4 μm to match with the characterized result which are explained in chapter 3. For the gauge factor calculation, the mask layouts for individual devices were altered by adding a circular patch of 20 μm radius on the center of the membrane. Then a new process flow was created with the added process as shown in Figure 2.14 to create a patch of 20 μm radius on the 3D model as shown in the Figure 2.15. During the simulation, pressure was applied only on the top the patch created at the center of the membrane, rather than the whole membrane surface and all sides of the membrane were fixed. That approach was implanted with the purpose of replicating membrane deflection using a probe. The meshing of the layers were done using extruded bricks with the mesh size of 2.5 μm . Pressure values shown in Figure 2.16 are only simulation settings which were required to displace each structure by 5.4 μm .

File Edit View Tools Windows Help										
Number	Step Name	Layer Name	Material Name	Thickness	Mask Name	Photoresist	Depth	Mask Offset	Sidewall Angle	Comments
0	Substrate	Substrate	SILICON	40	SubstrateMask					
1	passivation layer	passivation	Si3N4	0.4						
2	sacrificial polyimide	polyimide layer	POLYIMIDE	5.4						
3	Stack Material	Membrane	AL2O3	1.4						
4	Straight Cut				Patch	-	1.4	0	0	
5	Planar Fill	Patch	AL2O3	0.1						
6	Straight Cut				Patch	+	0.1	0	0	
7	Straight Cut				Patch	-	0.1	0	0	
8	Conformal Shell	piezoresistors	NICHROME	0.02						
9	Straight Cut				piezoresistor	+	0.02	0	0	
10	Straight Cut				poly	-	0	0	0	
11	Straight Cut				Polyimide_5	-	0	0	0	

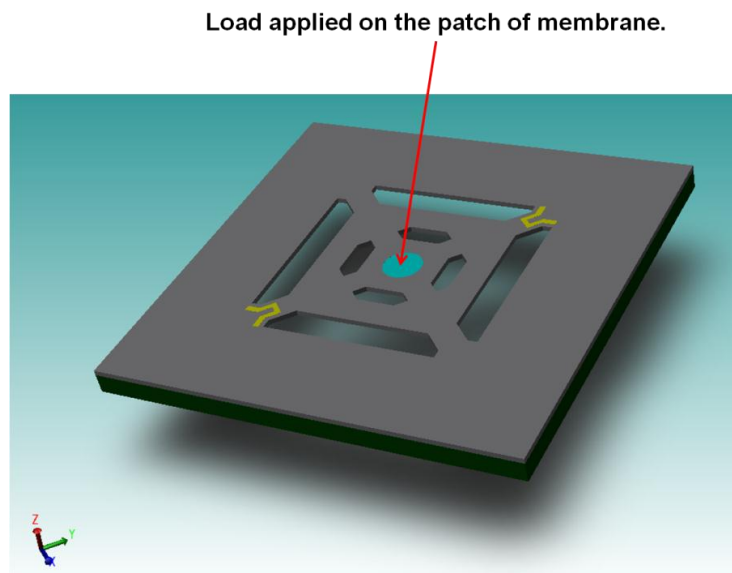
Figure 2.14 Process flow to create a patch on top of the membrane for pressure sensor simulations.



a)

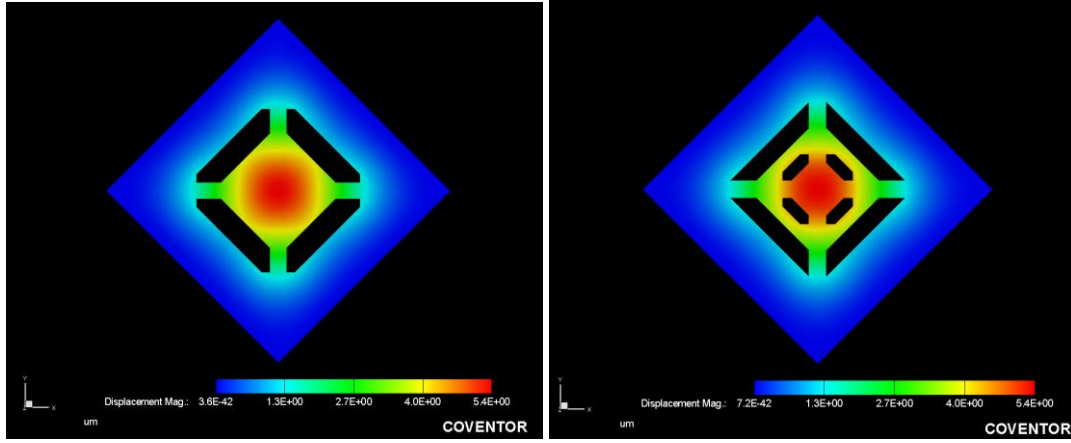


b)



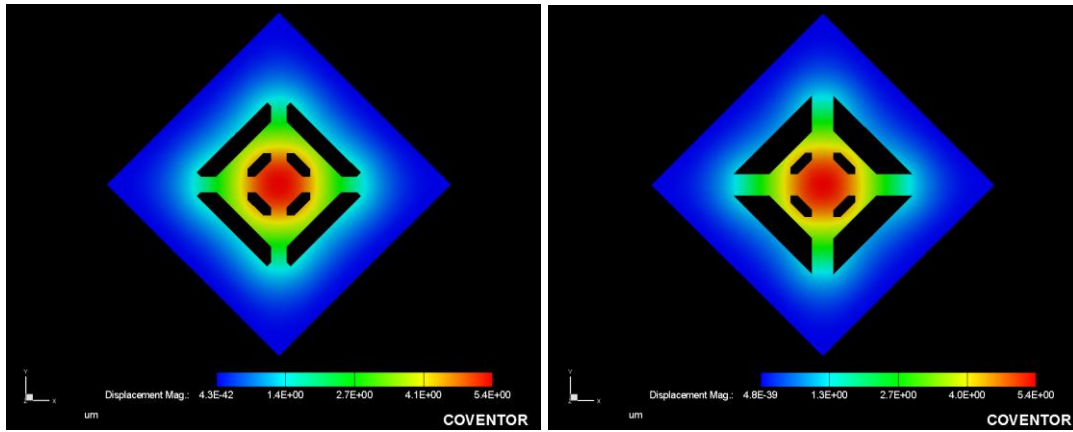
c)

Figure 2.15 Solid model of the some of the designed pressure sensors a) device T2 b) device T3 and c) device T4.



a)

b)



c)

d)

Figure 2.16 Simulation results for membranes displaced by 5.4 μm to determine average strain on piezoresistors. Pressures given are the values required to displace membrane by 5.4 μm . Gauge factor was calculated using $\Delta R/R$ obtained during the measurement for the input voltage of 1 V. a) $P=3.7\text{ MPa}$, $\epsilon_{\text{AVG}}=4.2 \times 10^{-2}$, b) $P=4.2\text{ MPa}$, $\epsilon_{\text{AVG}}=2.76 \times 10^{-2}$, c) $P=4.2\text{ MPa}$, $\epsilon_{\text{AVG}}=1.64 \times 10^{-2}$, d) $P=3.7\text{ MPa}$, $\epsilon_{\text{AVG}}=1.69 \times 10^{-2}$.

After simulations, strain analysis was performed to calculate average strain. Next the gauge factor was calculated using Eq. 2.14, by dividing $\Delta R/R$ by average strain. Calculated

gauge factor values are given in Table 2.2, Table 2.3, Table 2.4, Table 2.5, Table 2.6 and Table 2.7.

$$GF = \frac{\left(\frac{\Delta R}{R}\right)}{Strain_{AVG}} \quad (2.13)$$

Table 2.2 Actual gauge factor values calculated using measured $\Delta R/R$ for non-flexible devices.

Device Name	Maximum $\Delta R/R$	Average_strain	Maximum Guage Factor
T1	9.50%	0.0442	2.15
T2	12.00%	0.0276	4.35
T3	9.00%	0.0154	5.83
T4	10.30%	0.0169	6.09
T5	8.40%	0.0418	2.01
B1	7.00%	0.0262	2.67
B2	7.90%	0.0169	4.68
B3	8.00%	0.0369	2.17
B4	4.10%	0.0396	1.03

Table 2.3 Actual gauge factor values calculated using measured $\Delta R/R$ for non-flexible devices for 16nm thick piezoresistor.

16 nm Thick Piezoresistor					
Device Name	Average $\Delta R/R$	Maximum $\Delta R/R$	Average strain	Average Gauge Factor	Maximum Gauge Factor
T1	9.20%	9.20%	0.0442	2.08	2.08
T2	4.78%	9.20%	0.0276	1.73	3.34
T3	3.40%	3.40%	0.0154	2.20	2.20
T4	4.90%	7.20%	0.0169	2.90	4.26
T5	5.90%	6.60%	0.0418	1.41	1.58
B1	4.70%	5.80%	0.0262	1.79	2.21
B2	1.56%	1.77%	0.0169	0.92	1.05
B3	0.23%	0.23%	0.0369	0.06	0.06
B4	4.00%	4.00%	0.0396	1.01	1.01

Table 2.4 Actual gauge factor values calculated using measured $\Delta R/R$ for non-flexible devices for 24nm thick piezoresistor.

24 nm Thick Piezoresistor					
Device Name	Average $\Delta R/R$	Maximum $\Delta R/R$	Average strain	Average Gauge Factor	Maximum Gauge Factor
T1	8.95%	9.50%	0.0442	2.02	2.15
T2	9.53%	12.00%	0.0276	3.46	4.35
T3	6.85%	7.30%	0.0154	4.44	4.73
T4	8.85%	10.30%	0.0169	5.23	6.09
T5	5.40%	8.40%	0.0418	1.29	2.01
B1	4.90%	7.00%	0.0262	1.87	2.67
B2	7.90%	7.90%	0.0169	4.68	4.68
B3	4.87%	8.00%	0.0369	1.32	2.17
B4	3.40%	4.10%	0.0396	0.86	1.03

Table 2.5 Actual gauge factor values calculated using measured $\Delta R/R$ for non-flexible devices for 32nm thick piezoresistor.

32 nm Thick Piezoresistor					
Device Name	Average $\Delta R/R$	Maximum $\Delta R/R$	Average strain	Average Gauge Factor	Maximum Gauge Factor
T1					
T2					
T3	6.92%	9.00%	0.0154	4.48	5.83
T4	4.50%	5.70%	0.0169	2.66	3.37
T5	2.06%	3.50%	0.0418	0.49	0.84
B1					
B2					
B3					
B4	3.43%	3.60%	0.0396	0.87	0.91

Table 2.6 Actual gauge factor values calculated using measured $\Delta R/R$ for flexible devices of device type T3

Device Type T3					
Device Sample	Average Resistance	$\Delta R/R$	Average strain	Gauge Factor	
1	2594	-5.40%	0.0154	-3.50	
2	2626	-5.60%	0.0154	-3.63	
3	2675	-6.90%	0.0154	-4.47	
4	2889	-8.60%	0.0154	-5.57	

Table 2.7 Actual gauge factor values calculated using measured $\Delta R/R$ for flexible devices of device type T4.

Device Type T4				
Device Sample	Average Reistance	$\Delta R/R$	Average strain	Gauge Factor
1	2958	-10.80%	0.0169	-6.39
2	2952	-7.60%	0.0169	-4.49
3	3003	-7.10%	0.0169	-4.20
4	3205	-11.40%	0.0169	-6.74

2.7 Mask Layouts

For different masks were used to fabricate the device, each composing of an array of dies and each die consisted of 10 different device types. The mask layouts were shown in Figure 2.17, Figure 2.18, Figure 2.19 and Figure 2.20. All the masks that were used in fabrication are light field masks. The dimensions of the membrane are given in Figure 2.21 to Figure 2.29.

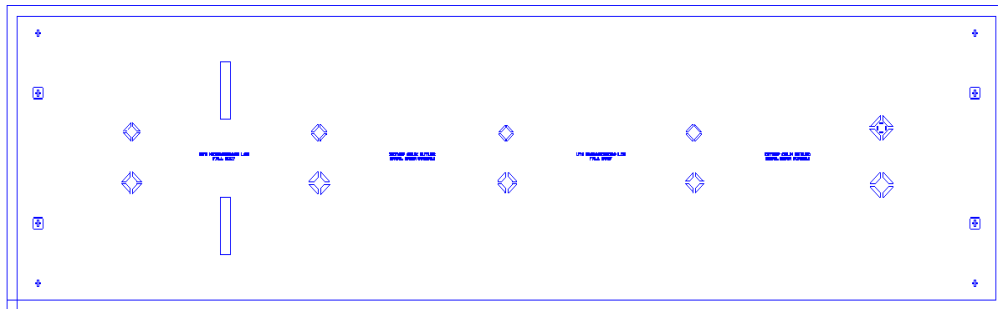


Figure 2.17 Membrane mask to fabricate membrane structure.

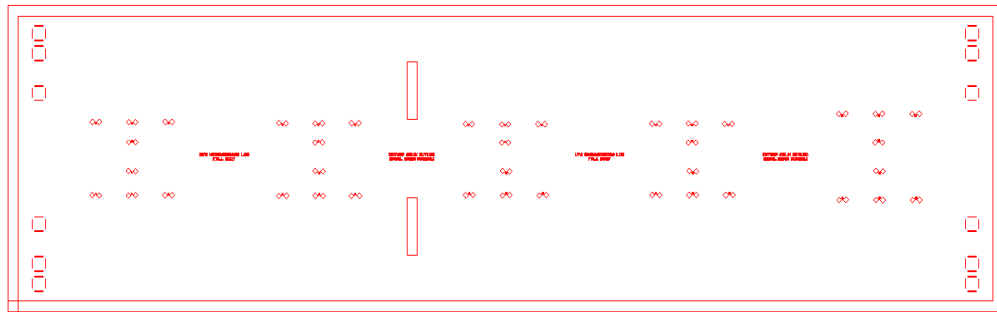


Figure 2.18 Piezoresistor mask to fabricate piezoresistors.

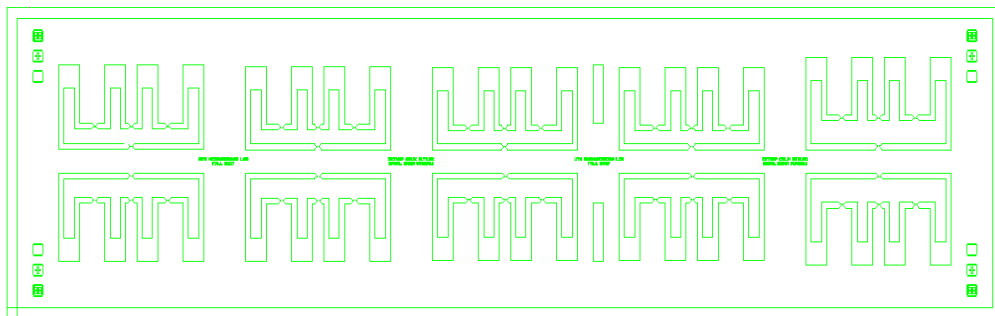


Figure 2.19 Metallization mask to create metal interconnects.

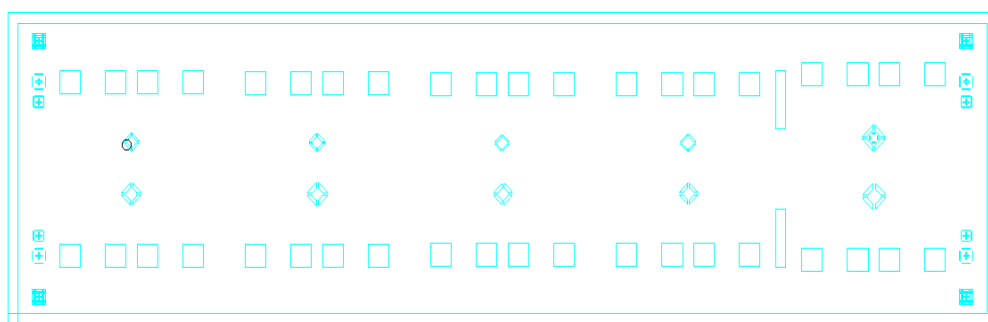


Figure 2.20 Ashing cover mask to protect piezoresistors from getting oxidized during ashing.

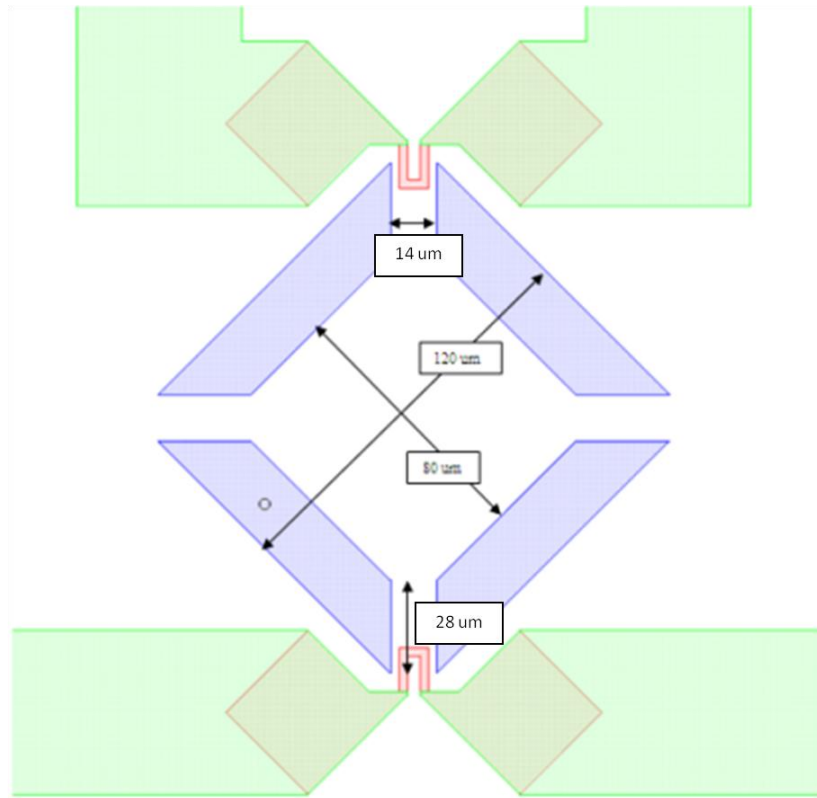


Figure 2.21 Membrane dimension for Device T1.

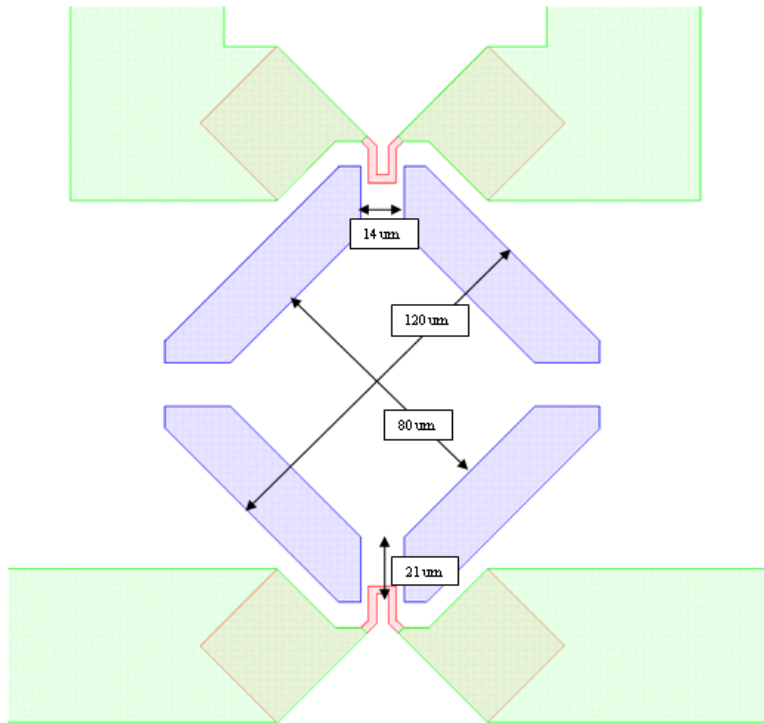


Figure 2.22 Membrane dimension for Device T2.

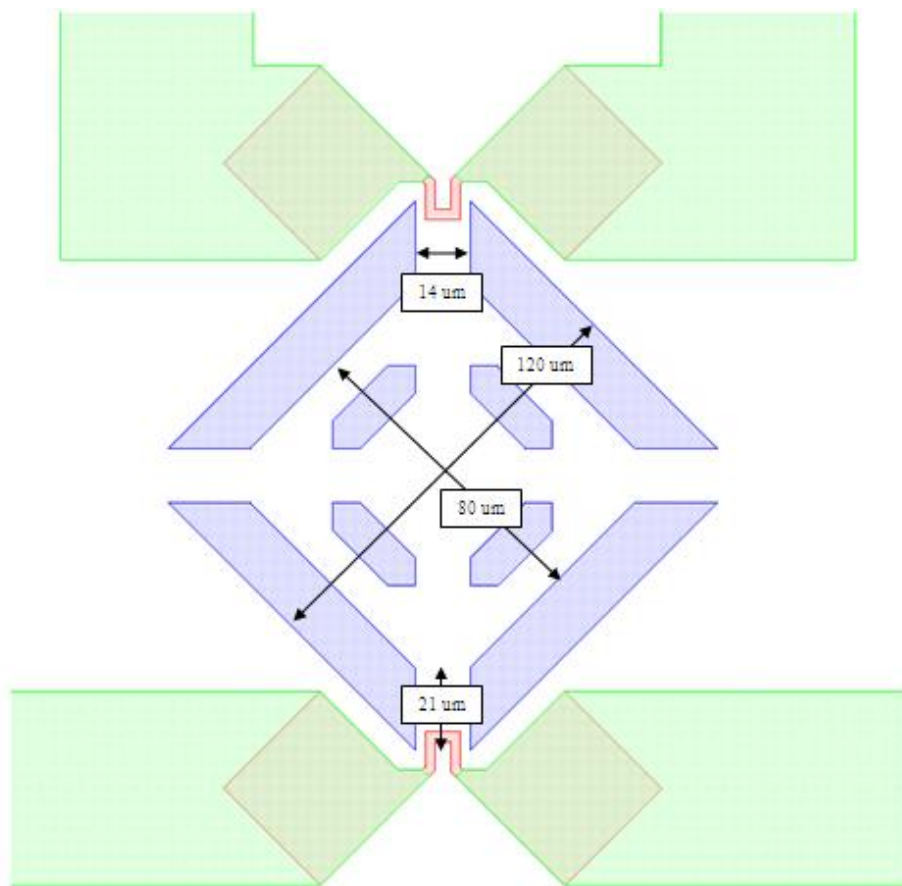


Figure 2.23 Membrane dimension for Device T3.

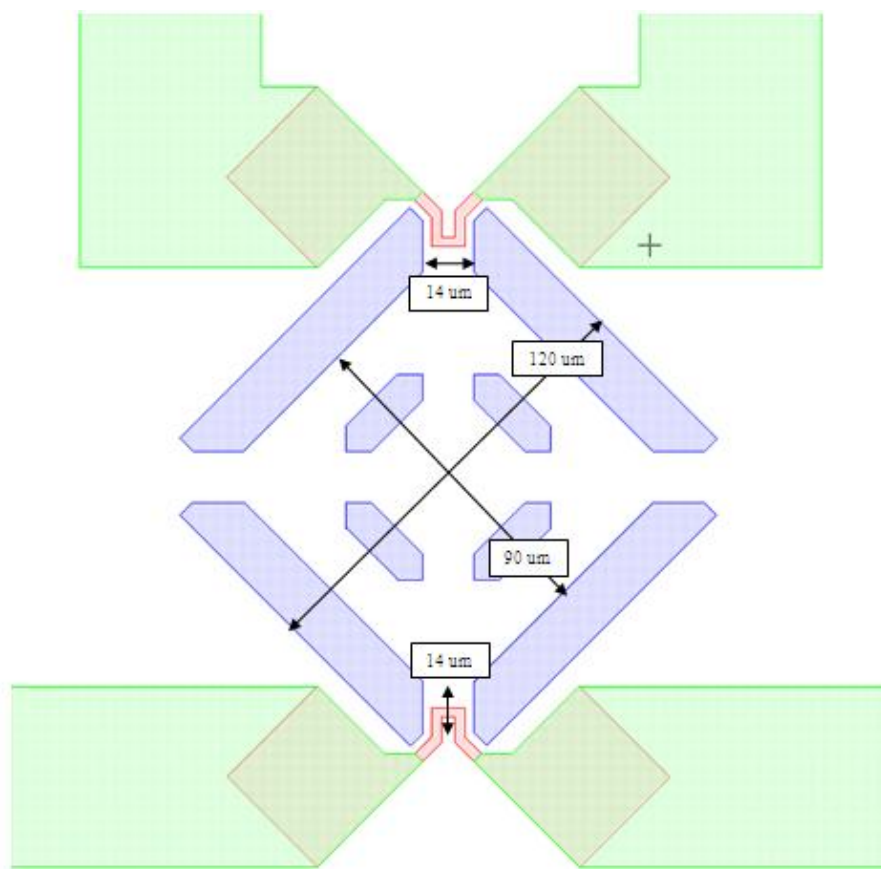


Figure 2.24 Membrane dimension for Device T4.

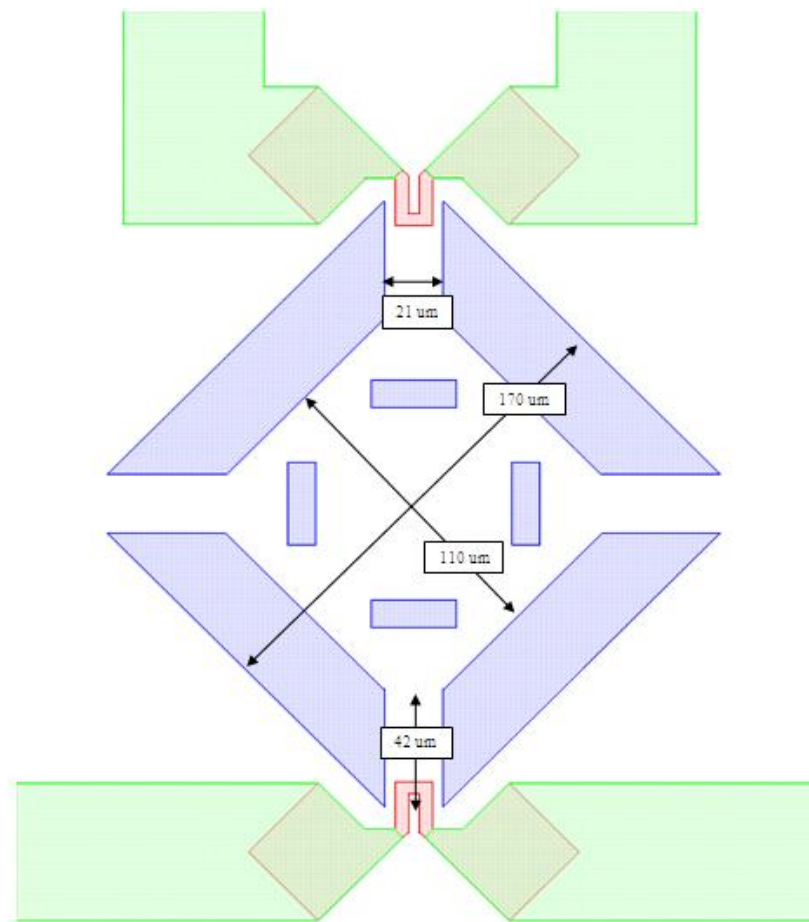


Figure 2.25 Membrane dimension for Device T5.

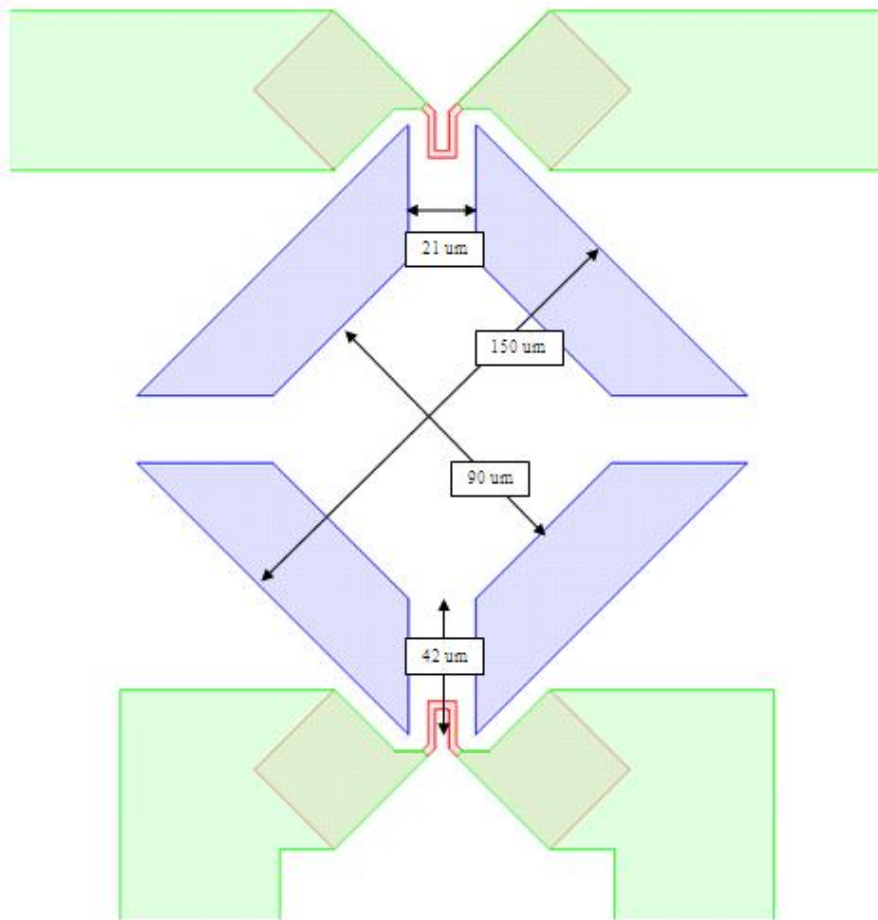


Figure 2.26 Membrane dimension for Device B1.

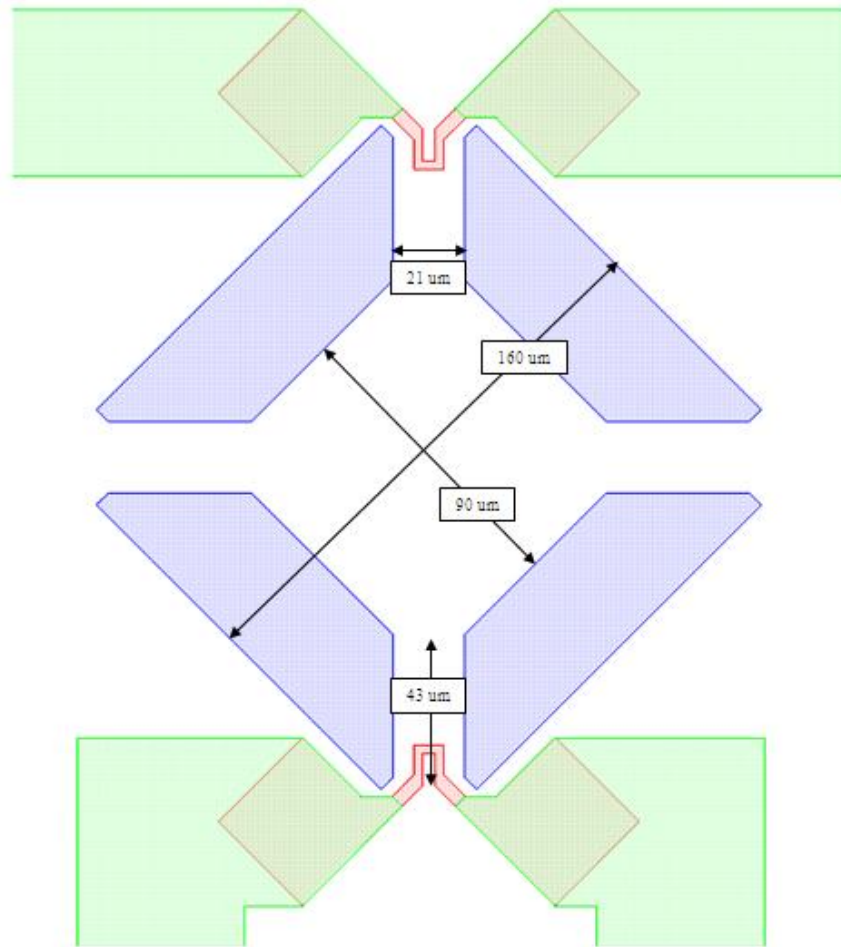


Figure 2.27 Membrane dimension for Device B2.

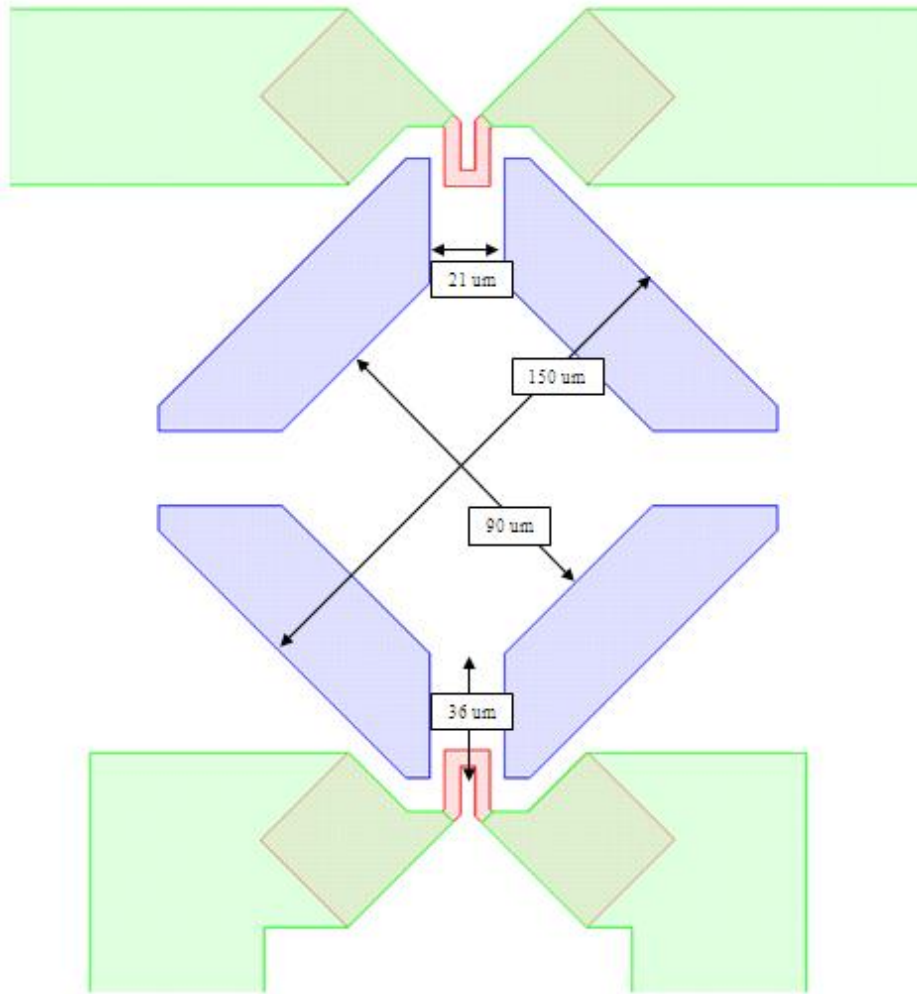


Figure 2.28 Membrane dimension for Device B3.

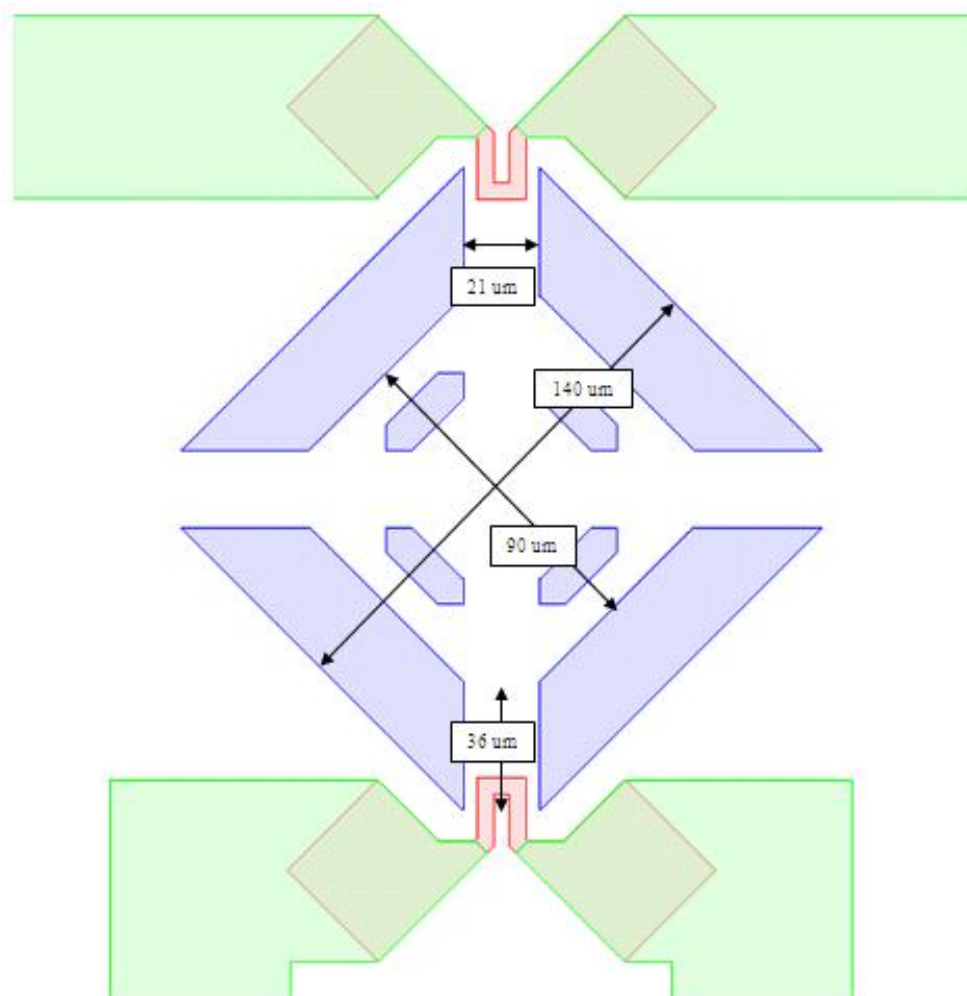


Figure 2.29 Membrane dimension for Device B4.

CHAPTER 3

FABRICATION AND CHARACTERIZATION OF PIEZORESISTIVE MEMS PRESSURE SENSOR USING NICHROME AS PIEZORESISTOR

3.1 Introduction

Different materials are used for thin film strain gauges such as metals, alloys, ceramics and semiconductors. The high resistivity of nickel chromium alloys (nichrome) along with their low temperature coefficient of resistance (TCR) and good temporal stability make them prime candidates for strain gauge application. Piezoresistive behavior of nichrome has been shown by Kazi et al [34]. Nichrome (NiCr 80/20 wt.%) is the most widely used alloy because of its high resistivity, low TCR, and low temperature dependence of gauge factor [35,36].

This chapter explains fabrication and characterization of piezoresistive MEMS pressure sensor using nichrome as piezoresistor.

3.2 Fabrication

The fabrication steps are illustrated in Figure 3.1. Before fabrication, wafers were degreased using trichloroethylene, followed by rinse in acetone, methanol and DI water. After that these wafers were undergone acid cleaning in 3:1 $\text{H}_2\text{SO}_4:\text{H}_2\text{O}_2$ and 6:1 BOE followed by DI water rinse and dehydration bake at 100 °C for 5 minutes. Before each fabrication step, wafers were cleaned in acetone and methanol, followed by DI water rinse and dehydration bake. Sputtering at room temperature was used for thin film deposition while etch and lift-off techniques were used to create structures. All photolithography was performed using OAI Model-806 i-line contact aligner. Details of all resist processes are given in Table 3.1.

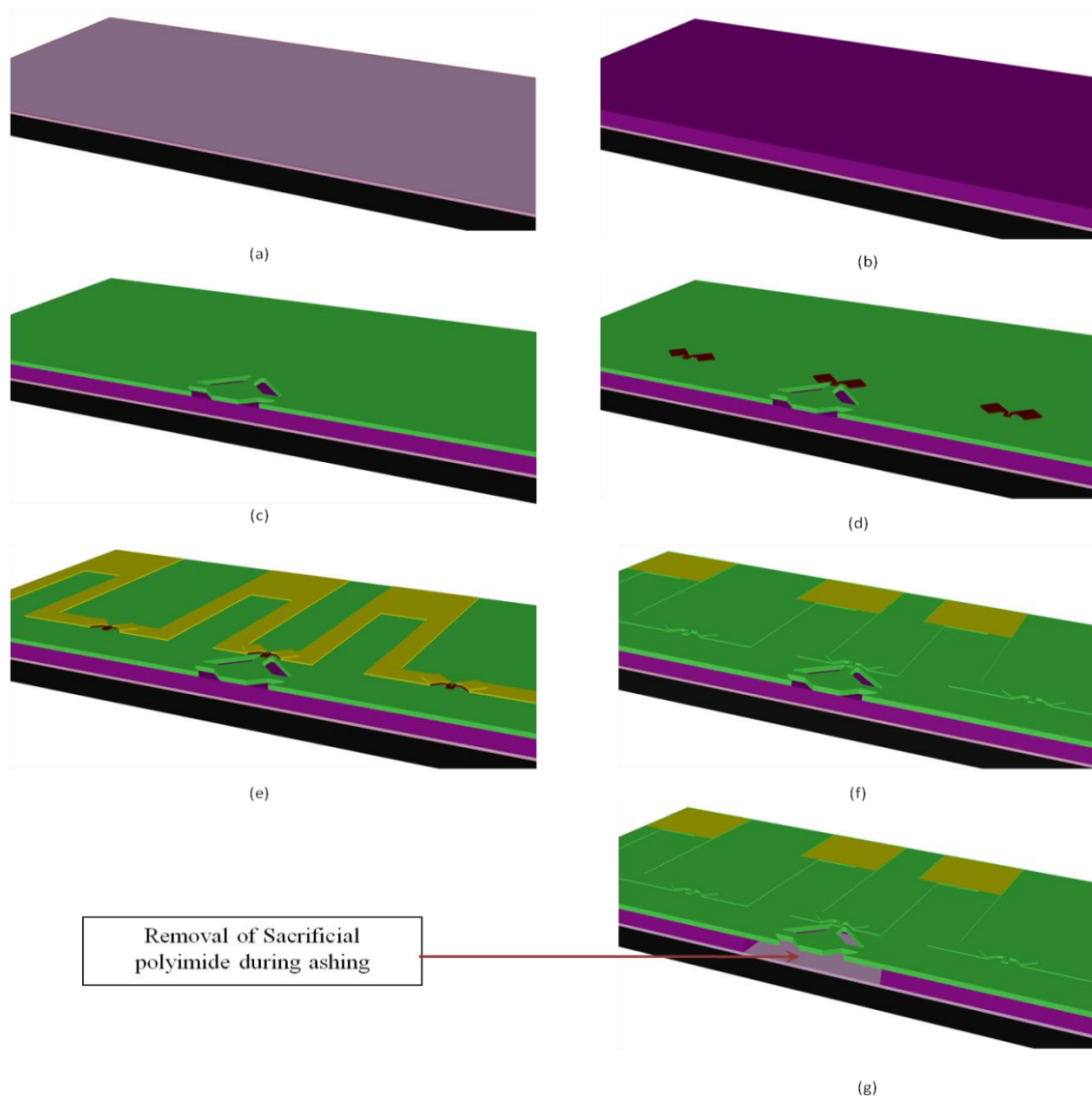


Figure 3.1 Cross sectional view of the pressure sensor at different steps during the fabrication process. (a) deposition of Silicon Nitrate layer, (b) deposition of sacrificial polyimide, (c) deposition and pattern of aluminum oxide as Membrane layer, (d) deposition and pattern of nichrome as Piezoresistor layer (e) deposition and pattern of aluminum as contact layer, (f) deposition of 100nm thick aluminum oxide layer to protect piezoresistors during ashing and (g) shows the removal of sacrificial polyimide beneath the membrane area during ashing.

Initially, 0.4- μm -thick silicon-nitride was deposited on silicon wafer using AJA ATC Orion series UHV sputter system at room temperature under the gas flow of 30 sccm of Argon and 5 sccm of N_2 with the chamber pressure of 2.8mT using 150 W RF power. This layer provides passivation as well as good adhesion for the subsequent polyimide layer. Next, the sacrificial polyimide PI 2611 (HD Microsystems) was spin coated at 4000rpm for 50 seconds followed by bake at 110 °C for 5 minutes on hot plate and cured at 300 °C for 8 hours in Nitrogen gas environment with a ramp up and ramp down rate of 1.5 °C/min, resulting in a final thickness of 5 μm .

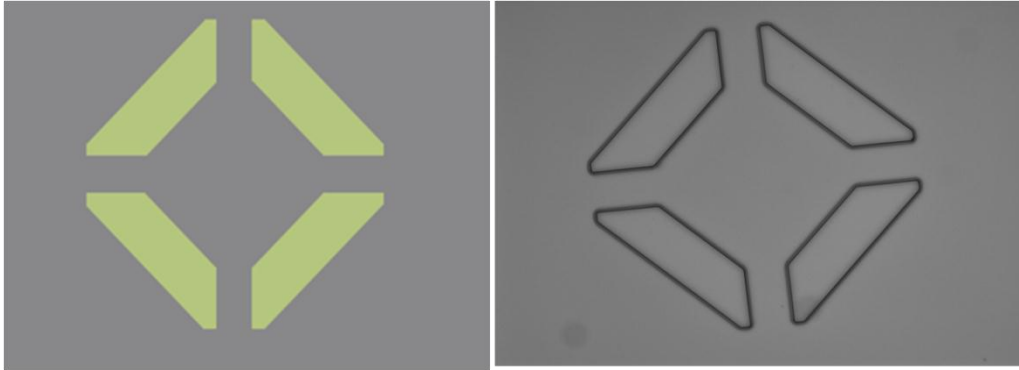


Figure 3.2 Membrane layer after the liftoff a) simulated b) fabricated.

Before depositing membrane layer, LOR 15B (Microchem) was spin coated at 2500 rpm for 40 seconds followed by hot plate bake at 150 °C for 3 minutes to act as undercut resist. Then S1813 (Shipley) positive photoresist was spin coated on top of LOR 15B at 2500 rpm for 40 seconds and patterned using membrane layer mask. Then, the 1.2- μm -thick aluminum oxide membrane layer was deposited by AJA ATC Orion series UHV sputter system at room temperature under the gas flow of 30 sccm of argon with the chamber

pressure of 5mT using 150 W RF power. After the deposition of membrane, trenches were opened by lift-off in Microposit Remover 1165 (Shipley). .



Figure 3.3 Piezoresistive layer after the liftoff a) simulated b) fabricated.

On top of this layer, NR-9 1500 PY (Futurrex) negative resist was spin coated and patterned with the piezoresistor layer mask. Then a very thin layer of nichrome (NiCr 80/20 wt.%) was deposited using RF magnetron sputtering (Home-built sputter system) at 10 mTorr chamber pressure using 60 W RF power supply with the gas flow of 50 sccm of Argon. Then the deposited nichrome was patterned by doing the liftoff process using Microposit Remover 1165 to form the piezoresistor layer.



Figure 3.4 Metallization contact layer after the liftoff a) simulated b) fabricated.

Three different samples varying the thickness of the nichrome piezoresistors from 10 nm to 40 nm were fabricated. Similarly, the interconnects connecting these piezoresistors in the Wheatstone bridge geometry was formed by patterning of NR-9 1500 PY resist with the metallization contact layer mask and then depositing 300-nm-thick aluminum which was deposited by AJA ATC Orion series UHV sputter system at 2.8 mTorr chamber pressure using 150 W RF power with the gas flow of 30 sccm of argon. Then aluminum layer is lifted off using Microposit Remover 1165 to form the interconnect layer. Then the sacrificial polyimide layer is removed by dry-etching using the plasma asher in the oxygen environment forming the suspended membrane structure shown in Figure 3.5.

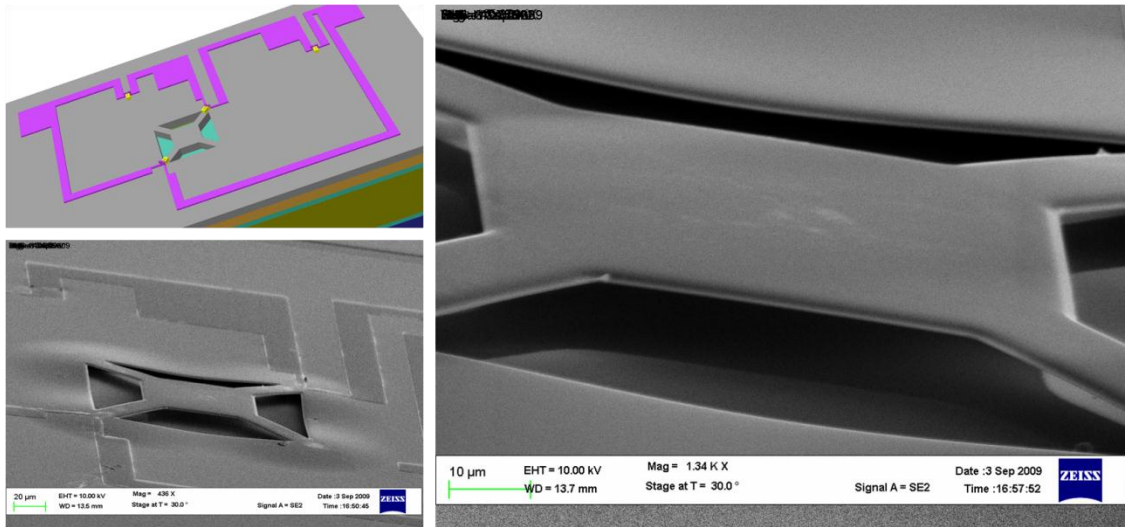


Figure 3.5 Top view of the 3D model of Pressure sensor and SEM image of Membrane suspended on the Polyimide layer after complete ashing.

3.3 Oxidation of Nichrome

The nichrome in devices fabricated like this got oxidized during ashing stage. The oxidation of unprotected nichrome was observed when the sample is exposed to oxygen in the plasma Asher as the temperature in the chamber reached to 300 °C and was documented by measuring the resistance as a function of the ashing time as shown in Figure 3.6.

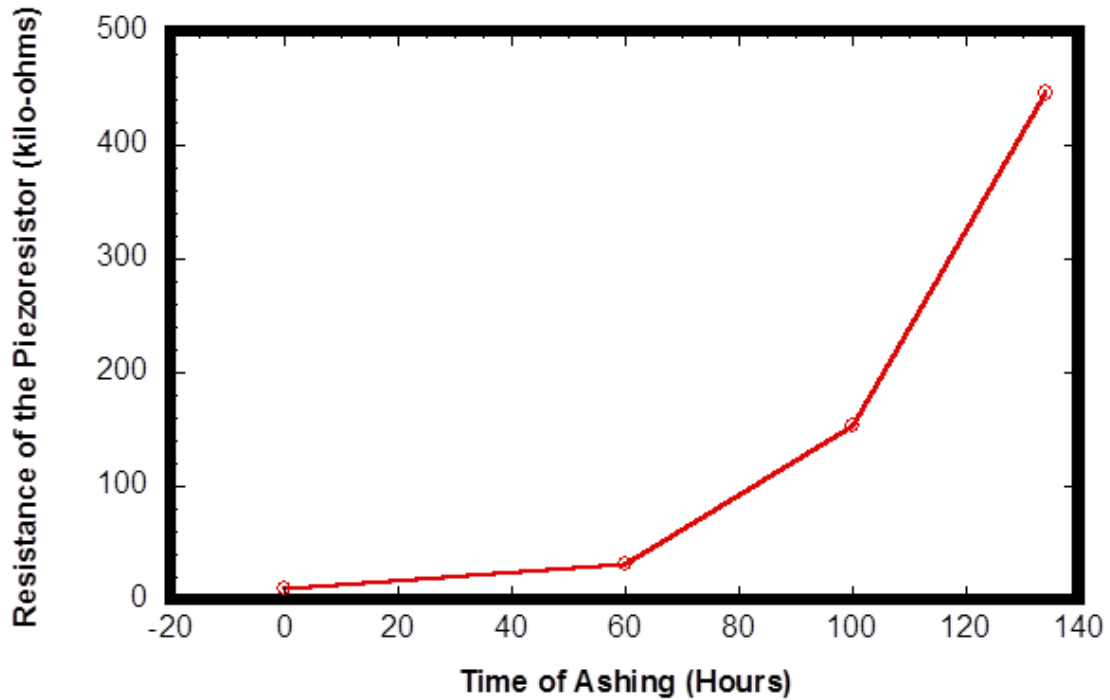


Figure 3.6 Change in resistance of nichrome due to oxidation during ashing.

To protect the piezoresistors from getting oxidized during ashing, the piezoresistors are covered with a very thin layer of 100-nm-thick aluminum oxide. The fabrication of this layer involves the deposition and pattern of NR-9 1500 PY photoresist using ashing cover layer mask and deposition of aluminum oxide layer using AJA ATC Orion series UHV sputter system at 2.8 mTorr chamber pressure using 150 W RF power with the gas flow of 30 sccm of Ar. Then the aluminum oxide is lifted off using Microposit Remover 1165 to form the structure covering the entire wafer except the trenches and the contact pads as shown in the Figure 3.1. After this, the sample is ashed in the plasma asher (Diener Electronics Asher) with the gas flow of oxygen under the chamber pressure of 0.6 mbarr using 150 W RF power for 100 hours. During this the machine is stopped for few hours per every 10 hours of

ashing. After this step membrane structure is released to form a suspended structure on top of polyimide layer as shown in the Figure 3.5.

3.4 Sheet resistance

Nichrome films of various thicknesses were RF magnetron sputtered on glass slides in an 100% argon environment at the chamber pressure of 10 mTorr and power of 60 W using a single target to determine the variation in the sheet resistance of the nichrome with film thickness. Simultaneously, a film was sputtered onto a piece of a silicon nitride coated silicon wafer with a photo-resist pattern. The nichrome film on the silicon wafer was patterned by lift off to determine the thickness of the films on both the silicon wafer and the glass slide. The sheet resistance and resistivity of the films and the corresponding film thickness were measured.

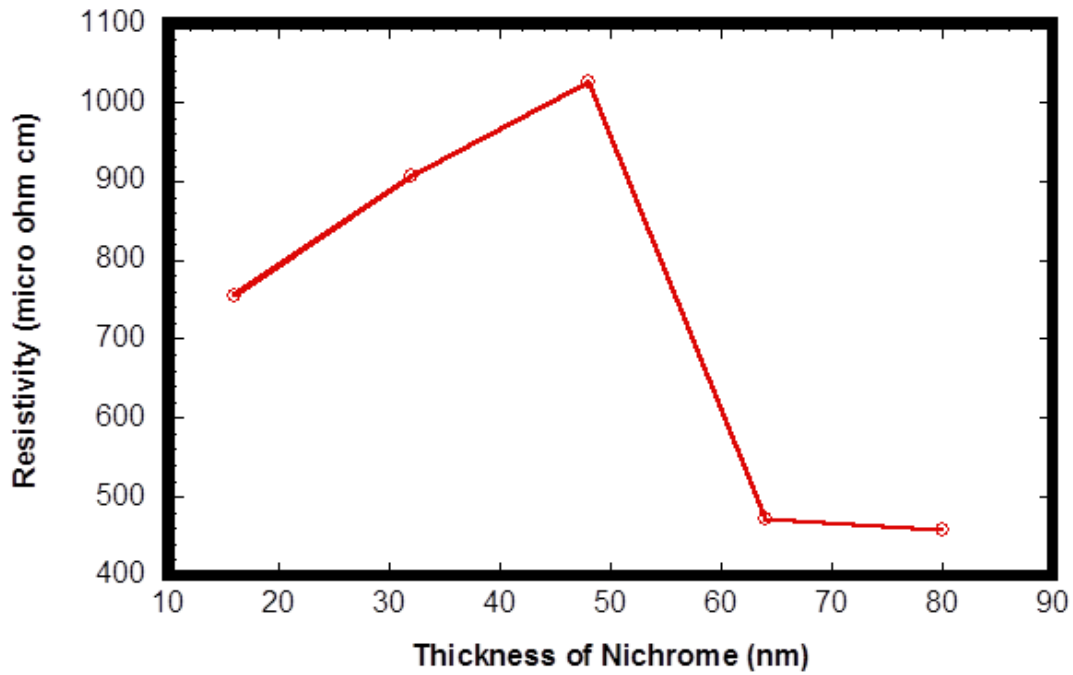


Figure 3.7 Resistivity vs. thickness of nichrome deposited by rf magnetron sputtering.

The sheet resistance is very high for small thicknesses, up to 472.66 Ω for 16 nm thick film, and decreases with increasing film thickness. This behavior is common for thin films [37,38] since the sheet resistance varies as the resistivity ρ divided by the thickness t (ρ / t). The variation of the resistivity with thickness is shown in Figure 3.7. The resistivity of the Nichrome is abruptly shifted to the higher value for the film thickness below 40 nm.

Table 3.1 Process details of photoresists that were used in pressure sensor fabrication

Resist	Spin Coating		Exposure Energy (mJ/cm ²)	Resist Bake (°C)		Development Time (sec)	Resist Thickness (μm)
	Rotation per minute	Duration (sec)		Pre-bake	Post-bake		
NR-9 1500PY	2500	40	295	150	100	15	1.76
S 1813	2500	40	90	100	none	30	1.2

3.5 Characterization

Three different samples, each varying the thickness of the Piezoresistor layer with the thickness of 16nm, 24nm and 32nm are fabricated and tested. Before testing the device, resistance of individual resistors, P1, A1, P2 and A2 is measured using Agilent 4155C semiconductor parameter analyzer connected to a probe station.

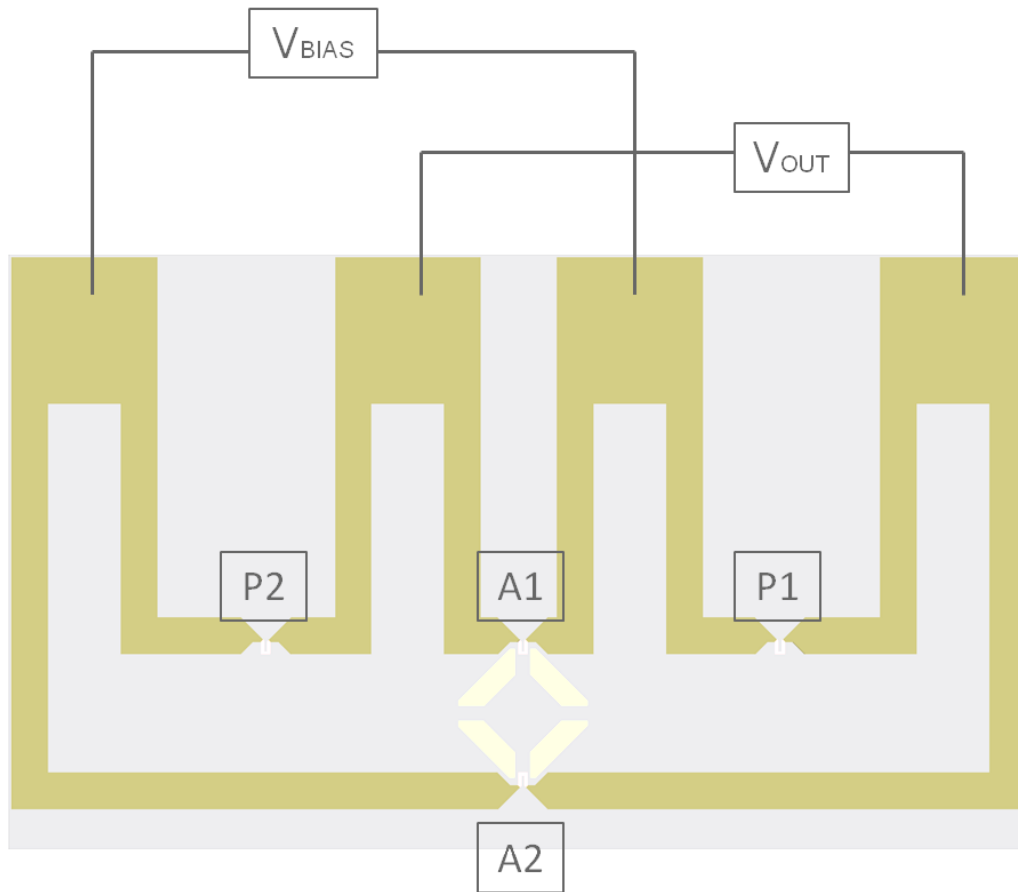


Figure 3.8 Illustration of the setup to measure pressure sensor response.

I-V characterizations were performed by probing bond pads and sweeping current between negative and positive 5×10^{-6} A using Agilent 4155C semiconductor parameter analyzer connected to a probe station. The resistance values were then found from the slope of obtained I-V charts. Resistances measured like this are denoted as total resistance since each direct measurement gives the resistance of the measured one in parallel with the series connection of other three. Then using a MathCAD code, the actual resistance values were calculated.

The testing of the fabricated pressure sensors is done using two different setups. One is using electrical probe station and another using load cell setup.

3.6 Using Probe station

The experimental setup is shown in the Figure 3.9. The input bias voltage V_{BIAS} is given using Agilent E3620A Power supply with constant DC Voltage of 1 to 4 V in steps of 1 V. The Output Voltage is measured using Keithley 2182A Nanovoltmeter. Input and output terminals are connected to the device by probing to bond pads with the help of 10 μ m probe tips and also the membrane is deflected using the similar type of probes as shown in the Figure 3.9. Membrane deflection is observed with the help of live display of the microscopic image provided by the measurement setup.

For every given input voltage two sets of output voltage is measured: one before the membrane deflection (V1) and the other when the membrane is fully deflected (V2) precisely with the help of live display and the change in voltage for full membrane deflection is calculated as $\Delta V = V1 - V2$. At first values of all the 4 resistors P1, P2, A1 and A2 are measured and then the offset voltage V_{offset} is calculated using the formula,

$$V_{offset} = V1 = \left[\frac{P_2}{A_1 + P_2} - \frac{A_2}{A_2 + P_1} \right] V_{BIAS}$$

The change in resistance is calculated using the formula,

$$V2 = \left[\frac{P_2}{A_1 + \Delta R + P_2} - \frac{A_2 + \Delta R}{A_2 + \Delta R + P_1} \right] V_{BIAS}$$

In the calculation it is assumed that change in resistance of A1 and A2 is equal and is taken as ΔR . The offset voltage V_{offset} obtained using the formula is compared to the output voltage V_1 obtained practically. If both the voltages are equal, then the device is further tested with load application. ΔV and $\Delta R/R$ for the maximum deflection of the membrane is obtained for different types devices and also for different thickness of piezoresistors.

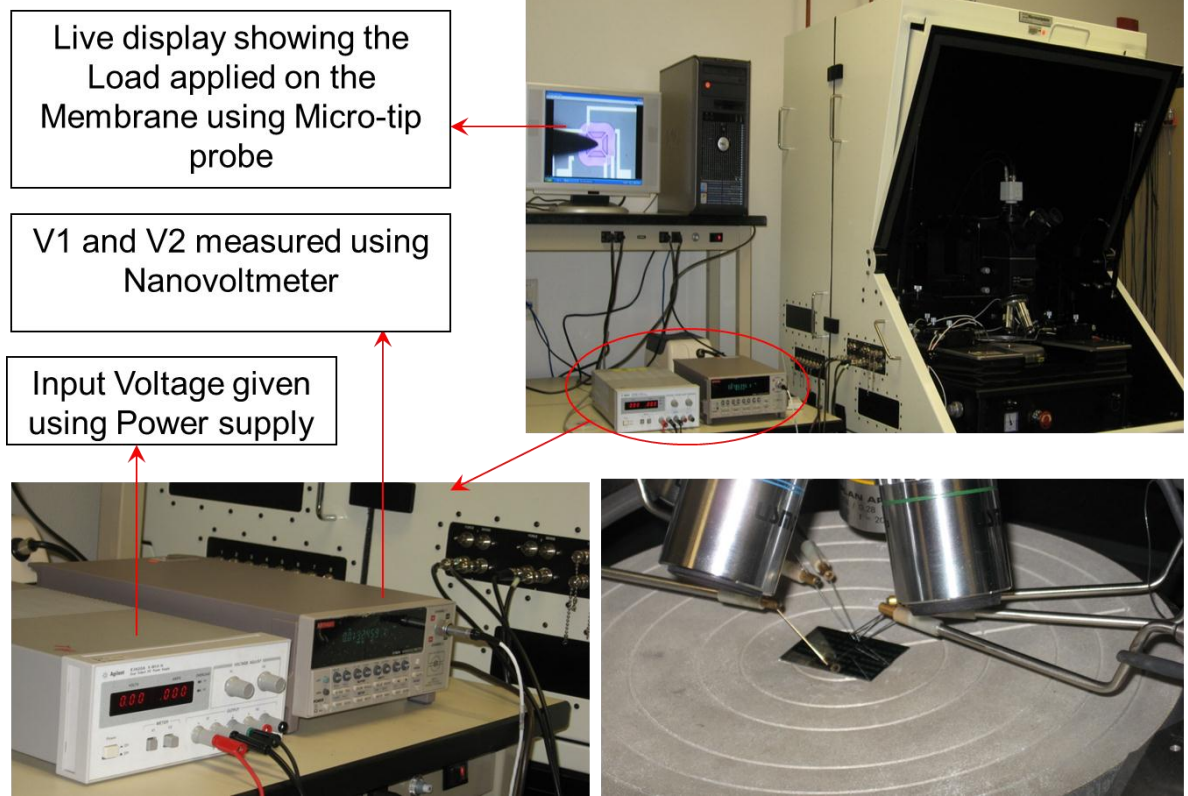


Figure 3.9 Testing using Probe station setup.

Four different connections

During the testing, change in voltage due to load application on the membrane for all the possible four different connections A+, A-, B+ and B- are tried. A+ Connection is as shown in Figure 3.8. If we interchange the terminals of the Input connection, then that connection is taken as A-. Similar combination can be achieved by interchanging the connections of input and output terminals, two different combinations B+ and B- are achieved. Ideally if all the resistors are equal then there should be no change in the results of all the four connections. And it is observed that the tested results match the closeness of the results for all four different connections to a large extent.

3.7 Using Load-cell

The load-cell apparatus is shown in Figure 3.10. The load-cell system consisted of a tensile mono-axial 10 gm load with a resolution of ± 0.005 gm, and a customized probe-tip holder to facilitate use of probe-tips with varying radius. This was attached to a PI-620 ZCD Nanopositioner with 0-50 μ m Z-axis travel and a minimum resolution of 0.2 nm. A micromanipulator stage that was capable of moving in the x, y and z-directions, was used for course movement. A rotary tilt stage was utilized to hold the sample and could be tilted from 0-45 degrees.

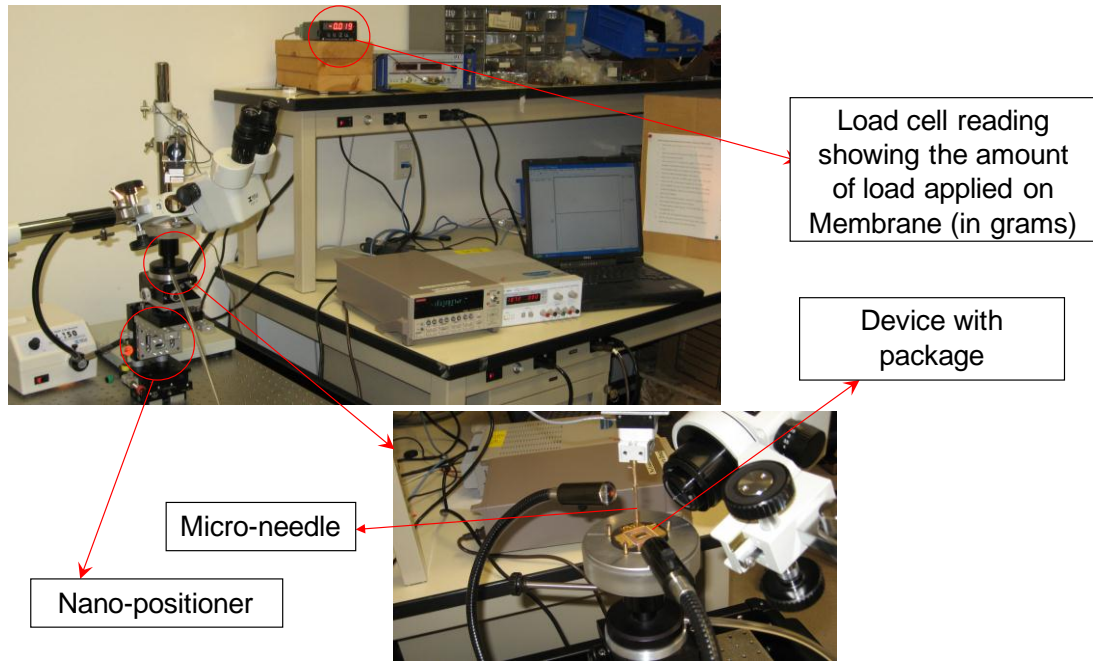


Figure 3.10 Testing using Load cell setup.

Before starting this test, the fabricated devices were cut into individual dies and then bonded to a package. The resistance of individual resistors was measured after bonding as a check. Each time, with the help of nanopositioner, the probe tip is moved for $0.2\mu\text{m}$ in z-direction and the corresponding reading of mass applied on the membrane (in grams) was taken. Thus, the amount of force applied each time on the membrane is calculated by using the formula, $F = m \times a$ where 'F' is the force applied on the membrane, 'm' is mass of the load applied on the membrane and 'a' is acceleration due to gravity (9.81m/sec^2).

The amount of pressure applied is then calculated using the formula given by S.K. Patil *et al.*, [39] $P = F/A$ where 'A' is the area of the contact area between the probe-tip and

the surface of the membrane. The contact area, 'A' was calculated by knowing the maximum deflection, 'd' of the Membrane for certain force using the formula,

$$A = \pi r^2 \sin^2 \theta$$

Where,

$$\theta = \cos^{-1} \left(\frac{r-d}{r} \right)$$

Where, 'r' is the radius of curvature of the probe tip.

3.8 Results and discussion

Consistency

With the probe station, the consistency of the measured ΔV result was observed when the load is applied and removed several times and each time the change in output voltage remained constant. The change in output voltage ΔV for the fully deflected membrane is also measured by changing the bias voltage. According to the experimental results, it is observed that the larger the bias voltage, the greater ΔV will be for the same amount of membrane deflection. But it has been observed that the device gets heated for the bias voltage greater than 2 V for the devices with 32-nm-thick nichrome. For the devices fabricated using 24-nm-thick nichrome, the device becomes significantly heated with bias voltages above 3 V and similarly for bias voltage greater than 4 V for 16-nm-thick nichrome. It has been observed that maximum ΔV was observed by using a 4V bias with 16-nm-thick piezoresistor devices.

Table 3.2 Average Resistance of all the Individual Piezoresistors of different devices, Standard Deviation of all the Individual Piezoresistors of different devices and Average $\Delta R/R$ and Maximum $\Delta R/R$ for different types of devices which are tested using probe station.

16 nm Thick Piezoresistor					
Device Name	Average Resistance of Individual Piezoresistor (Ω)	Standard Deviation	Standard Deviation/Average Resistance	Average $\Delta R/R$	Maximum $\Delta R/R$
T1	3995	128.05	3.21%	9.20%	9.20%
T2	3789	56.82	1.50%	4.78%	9.20%
T3	3213	25.05	0.78%	3.40%	3.40%
T4	3844	65.20	1.70%	4.90%	7.20%
T5	3230	57.46	1.78%	5.90%	6.60%
B1	3805	76.64	2.01%	4.70%	5.80%
B2	3623	77.29	2.13%	1.56%	1.77%
B3	2831	45.64	1.61%	0.23%	0.23%
B4	2791	56.22	2.01%	4.00%	4.00%
24 nm Thick Piezoresistor					
Device Name	Average Resistance of Individual Piezoresistor (Ω)	Standard Deviation	Standard Deviation/Average Resistance	Average $\Delta R/R$	Maximum $\Delta R/R$
T1	1763	58.70	3.33%	8.95%	9.50%
T2	1772	60.92	3.44%	9.53%	12.00%
T3	1312	28.73	2.19%	6.85%	7.30%
T4	1550	42.15	2.72%	8.85%	10.30%
T5	1158	26.58	2.30%	5.40%	8.40%
B1	2020	54.53	2.70%	4.90%	7.00%
B2	1727	94.82	5.49%	7.90%	7.90%
B3	1212	22.32	1.84%	4.87%	8.00%
B4	1084	15.55	1.43%	3.40%	4.10%
32 nm Thick Piezoresistor					
Device Name	Average Resistance of Individual Piezoresistor (Ω)	Standard Deviation	Standard Deviation/Average Resistance	Average $\Delta R/R$	Maximum $\Delta R/R$
T3	952	22.56	2.37%	6.92%	9.00%
T4	1086	18.58	1.71%	4.50%	5.70%
T5	881	6.26	0.71%	2.06%	3.50%
B4	911	10.14	1.11%	3.43%	3.60%

ΔV and $\Delta R/R$ (taken as the average of all the measured devices of single type) for the maximum deflection of the membrane were obtained for the 9 different types of devices investigated and also for the different thickness of the piezoresistor. Among the 9 different device types, devices designated T1 and T2 showed the maximum ΔV and $\Delta R/R$. The devices fabricated using 24-nm-thick piezoresistors showed the maximum ΔV and $\Delta R/R$ compared to devices of 16-nm and 32-nm-thick piezoresistors. According to the Table 3.2, the devices, fabricated using 24-nm-thick nichrome showed the maximum change in resistance on average with the maximum $\Delta R/R$ observed being 12%.

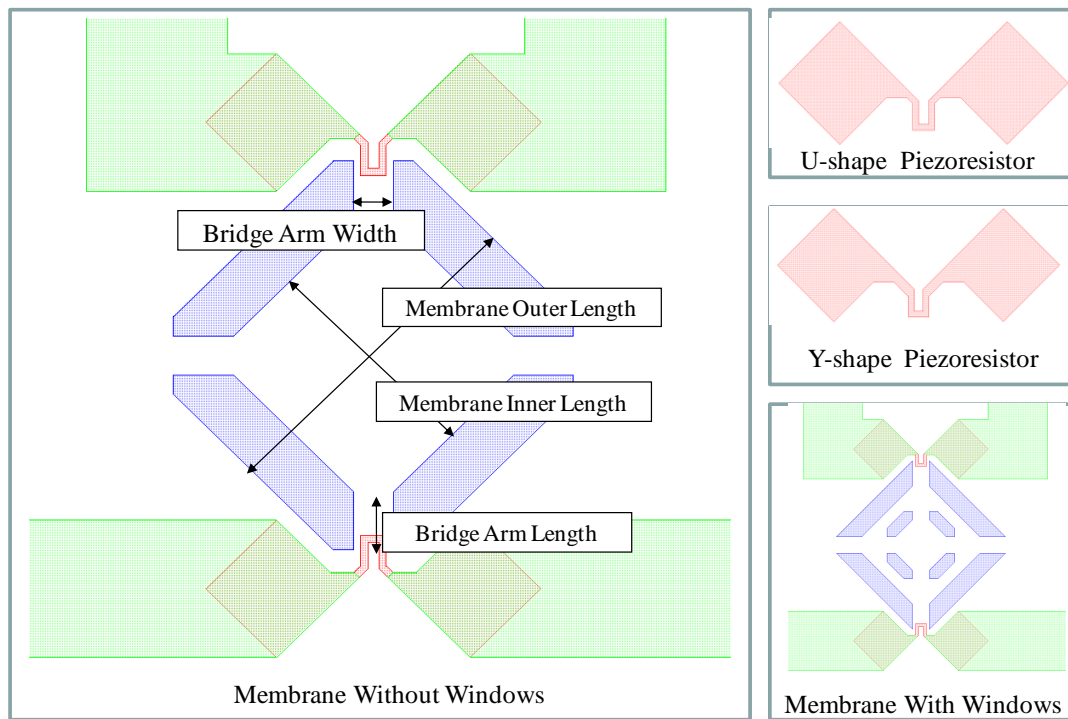


Figure 3.10 Description of typical device types.

Table 3.3 Description and dimension of different types of devices fabricated

Device Name	Structure	Type of Piezoresist or	Bridge Arm length/Width (μm)	Membrane Outer Length (μm)	Membrane Inner Length (μm)	Maximum $\Delta R/R$
T1	Without Windows	U	28/14	120	80	9.5%
T2	Without Windows	Y	22/14	120	80	12.0%
T3	With Windows	U	22/14	120	80	9.0%
T4	With Windows	Y	14/14	120	90	10.3%
T5	With Windows	U	43/21	170	110	8.4%
B1	Without Windows	U	43/21	150	90	7.0%
B2	Without Windows	Y	43/21	160	90	7.9%
B3	Without Windows	U	36/21	150	90	8.0%
B4	With Windows	U	36/21	140	90	4.1%

The average value of individual resistances and also standard deviation of the resistances of the devices which were tested listed in Table 3.2. Since the resistances of all the resistors in the Wheatstone bridge are very close, the offset voltage is small.

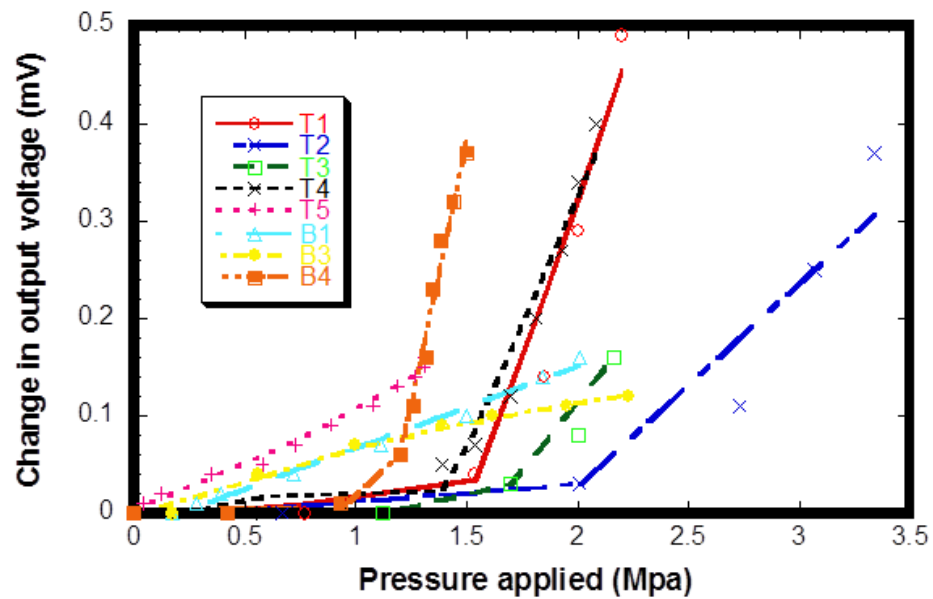


Figure 3.11 Load-cell result showing change in output voltage vs. pressure applied on the membrane for different types of devices.

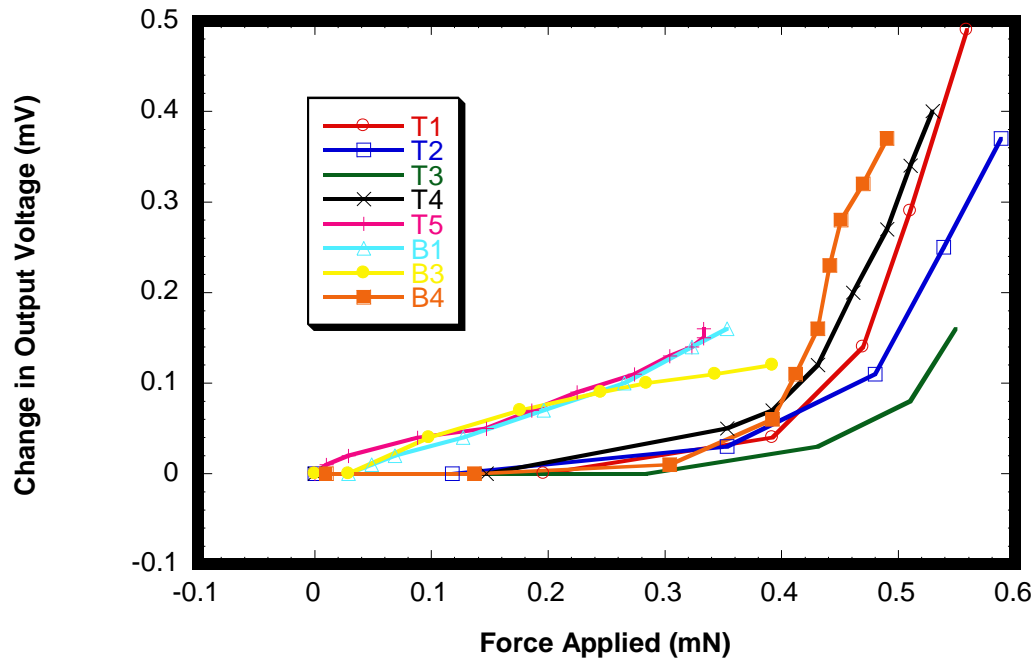


Figure 3.12 Load-cell result showing change in output voltage vs. force applied on the membrane for different types of devices.

The change in the output voltage versus the applied force and applied pressure was measured with the load cell for 8 different types of devices. This data is plotted in Figure 3.11 and Figure 3.12.

As shown in Figure 3.12, the change in output voltage is very less initially up to the certain force and then increases linearly as the force increases. The sensitivity of the device is characterized by taking the slope across two linear regions in Figure 3.11 and Figure 3.12 and has been listed in Table 3.4. The devices T5, B1 and B3 shows linear increase in voltage for the increase in force/pressure right from the start compared to the other devices. The devices T1 and T4 showed the best sensitivity compared to other ones. The variation in the sensitivity is primarily due to the difference in size and shape of the membrane forming

the pressure sensor causing the strain across the bridge arm is more compared to other devices for the same load applied on top of the membrane. The smaller membrane size devices show more sensitivity compared to the larger ones and also the membranes without windows showed better sensitivity compared to the devices with windows on membrane. The individual device description is shown in Figure 3.10.

Table 3.4 Sensitivity of the different devices which were characterized using Load-cell Measurement at two different regions which can be seen in the Figure 3.11 and Figure 3.12.

	Pressure		Force	
Device	Initial (mV/Mpa)	Final (mV/Mpa)	Initial Slope (mV/mN)	Final Slope (mV/mN)
T1	0.026	1.011	0.102	3.973
T2	0.016	0.424	0.091	2.411
T3	0.015	0.519	0.060	2.041
T4	0.063	0.750	0.246	2.947
T5		0.114		0.411
B1		0.086		0.491
B3		0.040		0.228
B4	0.043	0.881	0.135	2.698

CHAPTER 4

PRESSURE SENSOR FOR PROSTHETIC SKIN APPLICATION

4.1 Introduction

For so many years, most of the MEMS devices have been dominated by rigid components fabricated on silicon substrates. Only in the recent years, there has been substantial interest in the flexible MEMS devices due to abundant advantages such as lightweight, compact, portable, cost-effective, freedom of design, deformable and conform to non planer host surfaces. There is a huge demand for the sensors on flexible substrates having a wide range of applications in the field of defense, medicine, aerospace and commercial electronics. [40,41,42,43]

Problems associated with the current prosthesis

Prostheses have been used since the time of the ancient Egyptians in the fifteenth century BC and the earliest written evidence is said to be the Rig Veda, an ancient sacred poem of India written between 3500 and 1800 BC, where a warrior's lost leg was fitted with prosthesis fabricated from iron [44]. Since then there has been significant development in the prosthesis in its mobility and strength, still current prosthetic arms and limbs lack the feel of touch and there is lot of demand for the prosthesis to be equipped with the tactile sensors to sense pressure or feel the touch. Patients who use the current prosthesis have to operate their prostheses through visual feedback. Lot of times this makes very difficult for patients for even doing the simple work such as grabbing a cup as they cannot determine if they are grasping the cup strongly enough to hold it without breaking it. Developing the pressure sensors on the flexible substrate is the first step toward providing the tactile sensors to the prosthetic arms, making the wearer feel as though he or she has a real hand.

4.2 Fabrication

For the fabrication of pressure sensors on flexible substrates, initially 0.4- μm -thick silicon-nitride was deposited on clean silicon wafer using AJA ATC Orion series UHV sputter system at room temperature under 30 sccm of Argon and 5 sccm of N_2 gas flow with the chamber pressure of 2.8mT using 150 W RF power. This layer provides passivation as well as good adhesion for the subsequent polyimide layer. Next, a stack of six layers of PI 5878G (HD Microsystems) polyimide was spin coated on top of silicon-nitride layer at 1500 rpm for 60 seconds followed by bake at 110 °C for 5 minutes and repeated the same spin and bake recipe for each layer. Curing was done in nitrogen gas by ramping up the temperature to cure at 300 °C with a dwell time of 8 hours in nitrogen gas environment with a ramp up and ramp down rate of 1.5 °C/min, resulting in a final thickness of 40 μm . This layer acts as the flexible substrate which will be peeled off from the silicon nitride layer on top of silicon substrate when the device fabrication has been completed.

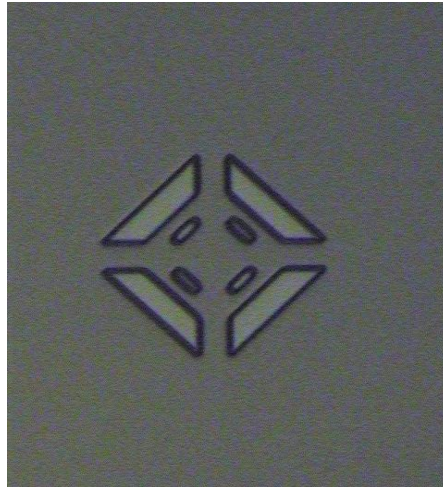


Figure 4.1 Membrane layer after liftoff.

Again, a layer of 0.4- μm -thick silicon-nitride was deposited on top of the flexible polyimide layer using AJA ATC Orion series UHV sputter system at room temperature under the gas flow of 30 sccm of argon and 5 sccm of N_2 with the chamber pressure of 2.8mT using 150 W RF power. This layer provides passivation as well as good adhesion for the subsequent polyimide layer. Next, 5 μm thick sacrificial polyimide is deposited using PI 2611 (HD Microsystems) by spin coating on top of the silicon nitrate layer at 4000rpm for 50 seconds followed by bake at 110 °C for 5 minutes on hot plate and cured at 300 °C for 8 hours in nitrogen gas environment with a ramp up and ramp down rate of 1.5 °C/min.

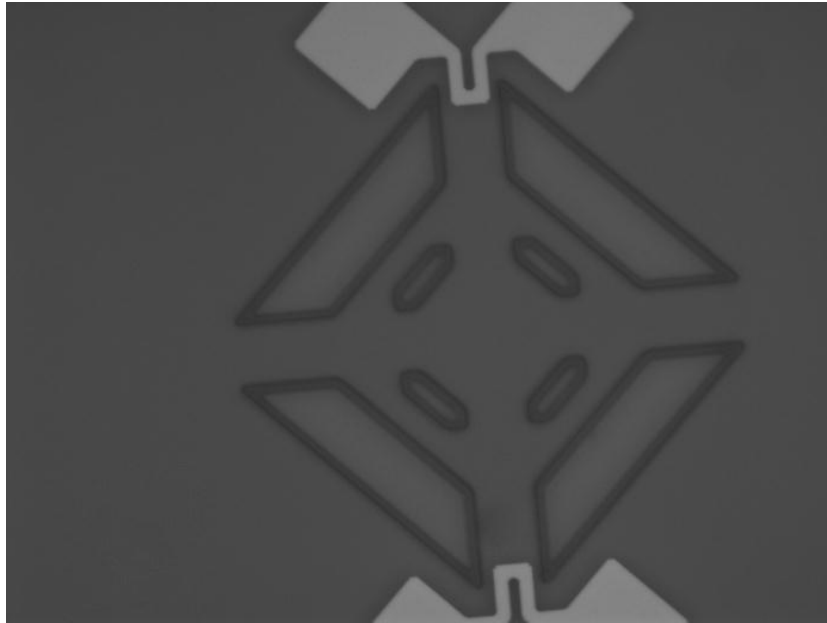


Figure 4.2 Piezoresistive layer after nichrome liftoff.

After the sacrificial layer, a 1.2- μm -thick aluminum oxide membrane layer was deposited using AJA ATC Orion series UHV sputter system at room temperature under the gas flow of 30 sccm of argon with the chamber pressure of 5mT using 150 W RF power and patterned using lift-off method by following the same recipe using in the fabrication of non-flexible substrate.

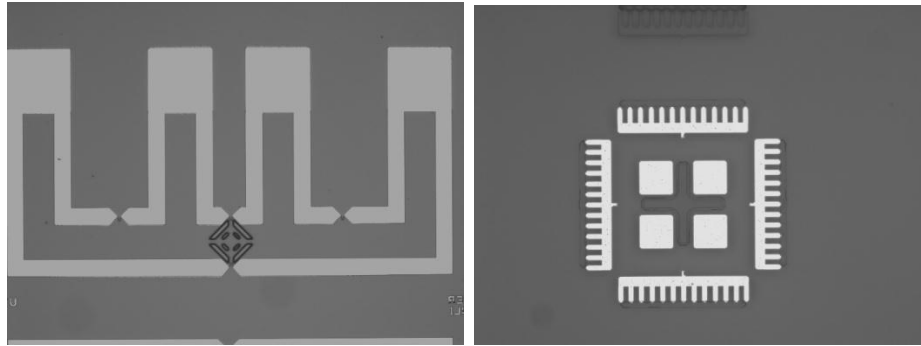
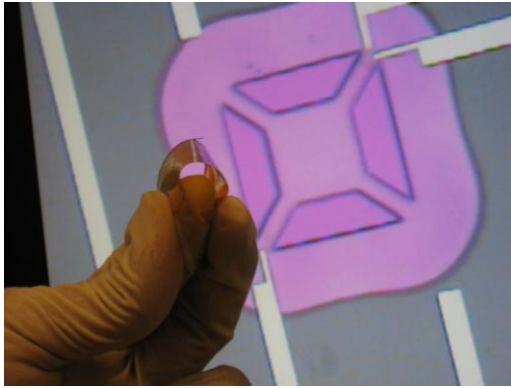


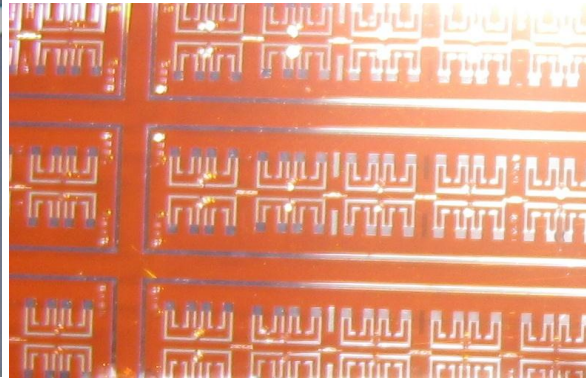
Figure 4.3 Contact layer after aluminum liftoff.



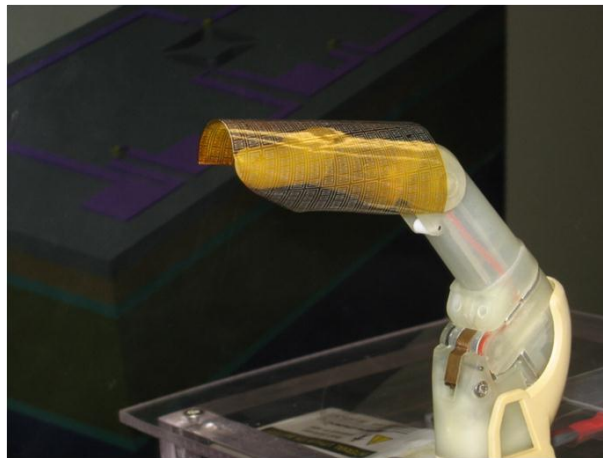
Figure 4.4 SEM image showing the suspended membrane structure after ashing.



a)



b)



c)

Figure 4.5 Device after peeling off from the silicon substrate a) and c) shows the flexibility of the device sample after peeling off, b) a closer look at the peeled off device sample.

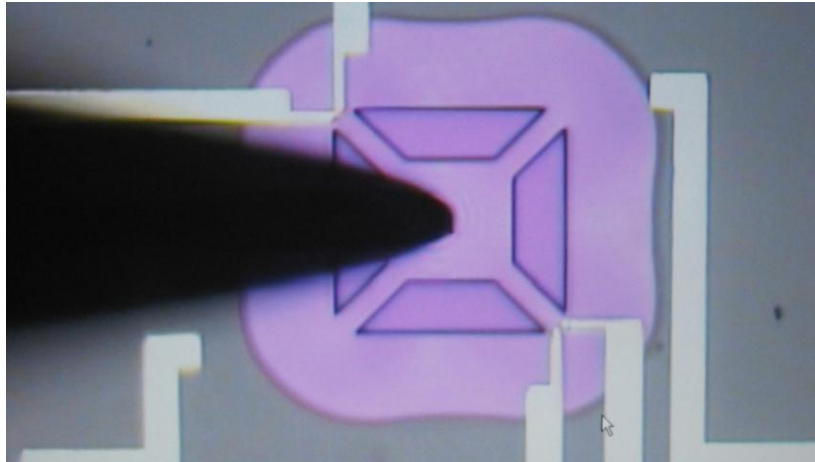
On top of this layer, NR-9 1500 PY (Futurrex) negative resist was spin coated and patterned with the piezoresistor layer mask. Then a very thin layer of 16-nm-thick nichrome (NiCr 80/20 wt.%) was deposited using RF magnetron sputtering (Home-built sputter

system) at 10 mTorr chamber pressure using 60 W RF power supply with the gas flow of 50 sccm of Argon. Then the deposited nichrome was patterned by doing the liftoff process using Microposit Remover 1165 to form the piezoresistor layer.

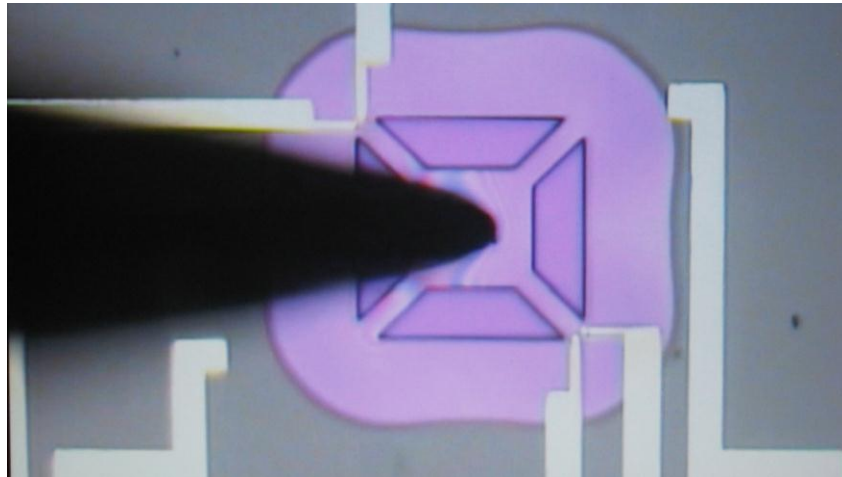
Then the metallization contact layer was formed first by patterning of NR-9 1500 PY resist using the contact layer mask and then depositing 300-nm-thick aluminum which was deposited by AJA ATC Orion series UHV sputter system at 2.8 mTorr chamber pressure using 150 W RF power with the gas flow of 30 sccm of argon. And finally, the aluminum layer is lifted off using Microposit Remover 1165 to form the interconnect layer. Then, the final layer of 100-nm-thick aluminum oxide which acts as the protective layer for nichrome piezoresistors during ashing is deposited and patterned using liftoff technique using NR-9 1500 PY photoresist as explained in chapter 3.

After this, the sample is ashed in the plasma asher (Diener Electronics Asher) for 100 hours with the gas flow of oxygen under the chamber pressure of 0.6 mBarr using 150 W RF power to release the suspended membrane structure top of polyimide.

After all the layers are fabricated the flexible polyimide is peeled off from the silicon substrate mechanically. After peeling off the flexible device, it can be used for the tactile sensing application for the prosthesis.



a)



b)

Figure 4.6 Picture of the live display on the screen during the membrane deflection a) before the membrane is deflected b) during the membrane deflection.

4.3 Characterization

Before testing the device, resistance of individual resistors, P1, A1, P2 and A2 is measured using Agilent 4155C Semiconductor Parameter Analyzer connected to a probe station. And the I-V characterizations were performed by probing bond pads and sweeping current between negative and positive 5×10^{-6} A using Agilent 4155C Semiconductor Parameter Analyzer connected to a probe station.

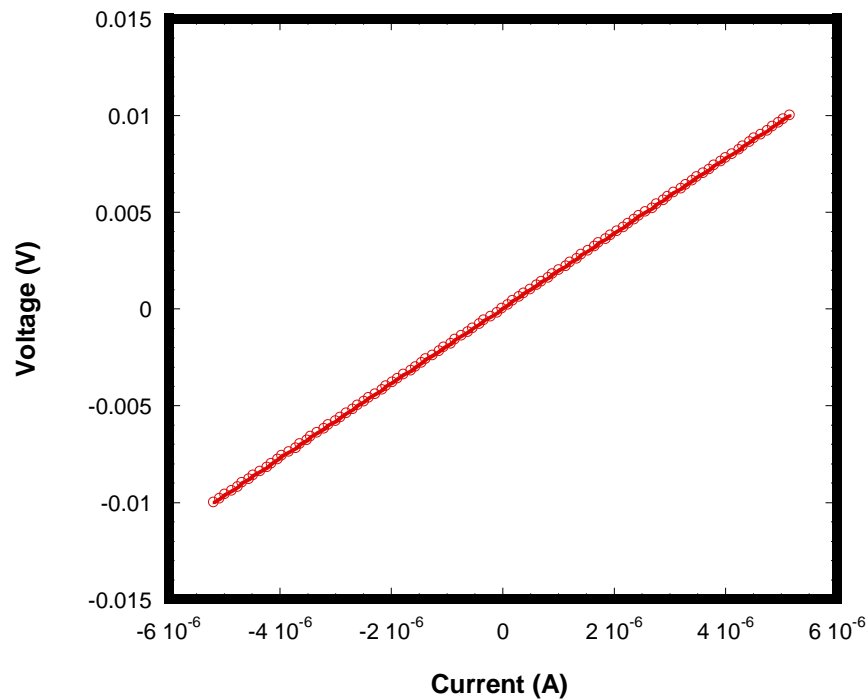


Figure 4.7 Typical plot showing liner I-V characterizations.

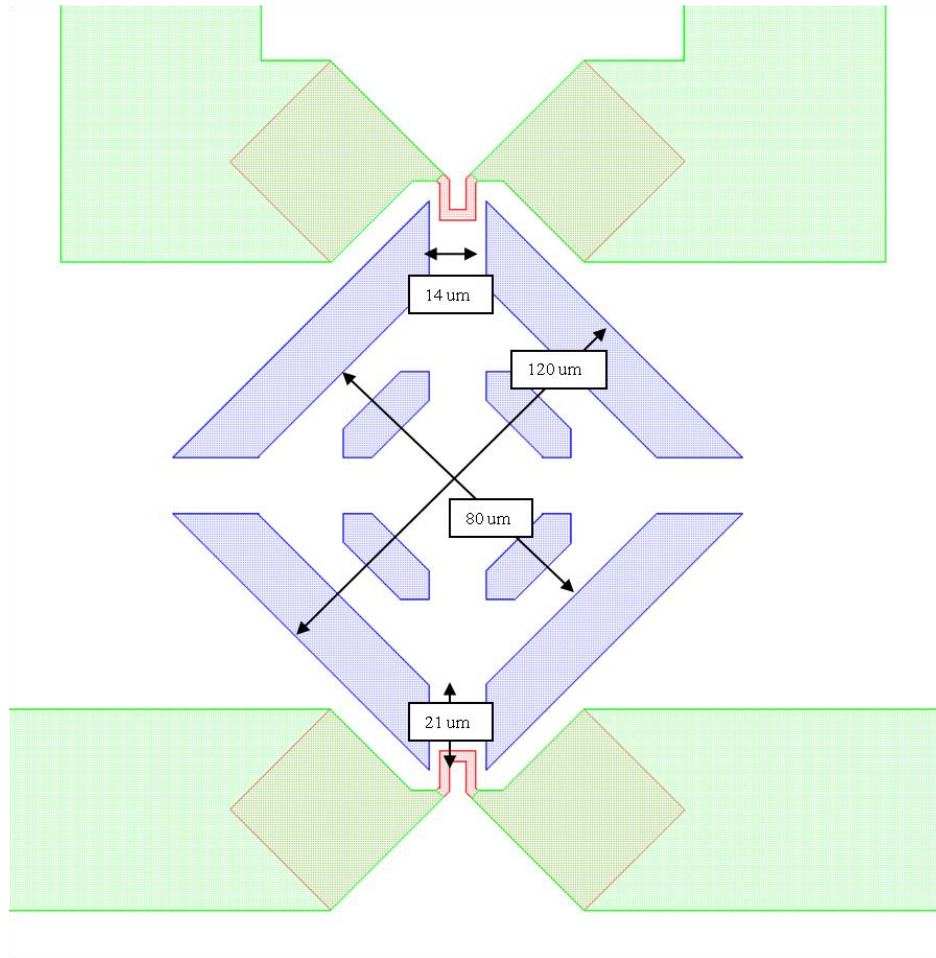


Figure 4.8 Description of the T3 device used for the characterization.

The resistance values were then found from the slope of obtained I-V charts. Resistances measured like this are denoted as total resistance since each direct measurement gives the resistance of the measured one in parallel with the series connection of other three. Then using a MathCAD code, the actual resistance values were calculated. I-V curve obtained using probe station is linear for all the resistance measurement and a

typical I-V curve is shown in Figure 4.7. The individual resistance values are shown in Table 4.1 and Table 4.2

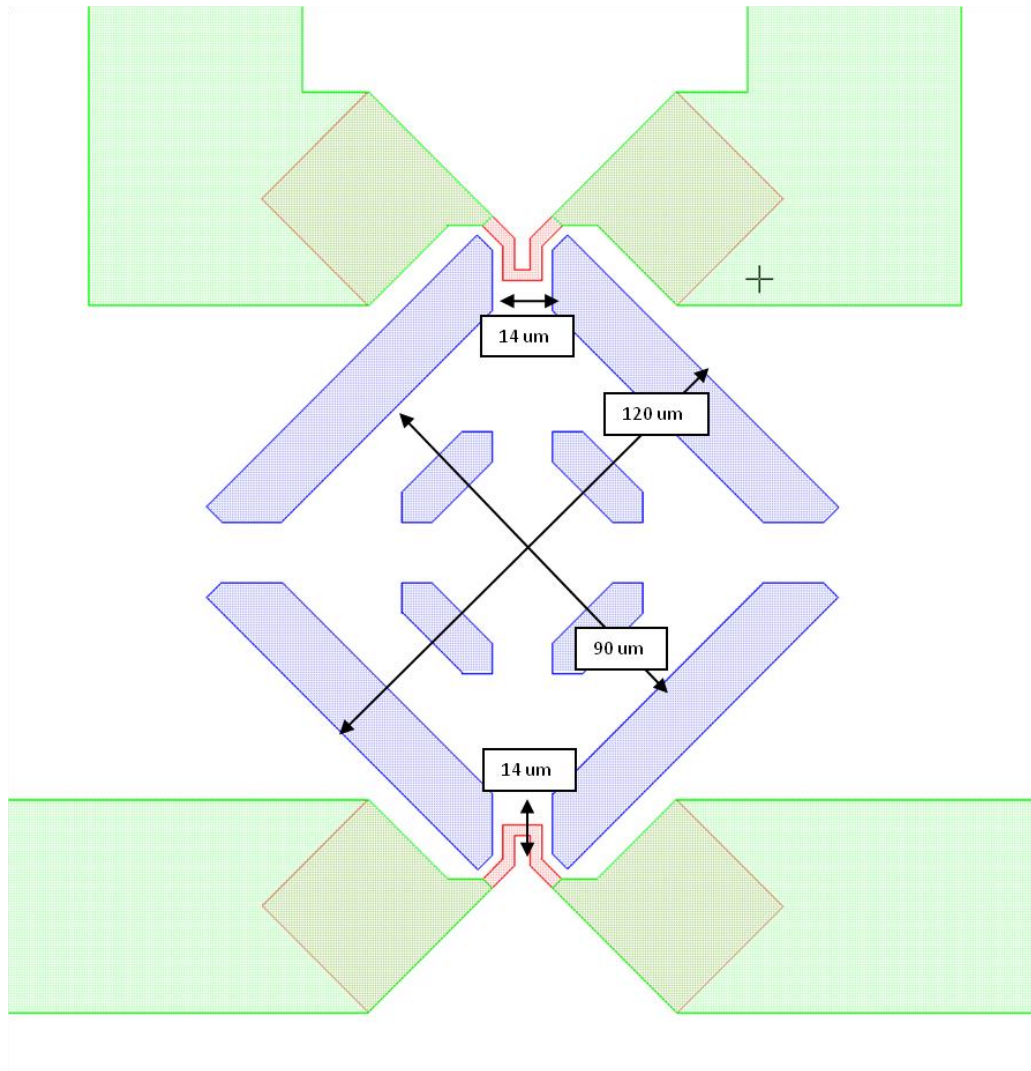


Figure 4.9 Description of the T4 device used for the characterization.

The testing of the fabricated pressure sensors is done using two different setups. One is using an electrical probe station and another using load cell setup. Two devices were tested and the device dimensions are given in Figure 4.8 and Figure 4.9. Each type of device is tested using two different methods similar to the non-flexible devices.

Using Probe station

Table 4.1 Complete description of the T3 device characterized.

Die Name	3.12	3.13	3.14	3.16	Average Resistance (Ω)	Standard Deviation/ Average Resistance
P1	2574	2610	2647	2863	2674	4.86%
A1	2622	2664	2715	2947	2737	5.30%
P2	2546	2572	2610	2790	2630	4.19%
A2	2635	2659	2726	2954	2744	5.30%
Average Resistance (Ω)	2594	2626	2675	2889	2696	4.92%
Standard Deviation	42	44	55	78	55	30.35%
Standard Deviation/Average Resistance (Ω)	1.60%	1.66%	2.07%	2.69%	2.00%	24.97%
V_{offset} (mV)	13.00	13.00	17.00	22.00	16.25	26.29%
V1 (mV)	13.45	13.91	17.33	22.23	16.73	24.24%
V2 (mV)	12.21	12.67	16.10	21.04	15.51	26.30%
ΔV (mV)	1.24	1.24	1.23	1.19	1.23	1.96%
ΔR	-142.43	-148.13	-187.51	-253.76	-182.96	-28.03%
$\Delta R/R$	-0.05	-0.06	-0.07	-0.09	-0.07	-22.27%
$\Delta R/R$	-5.40%	-5.60%	-6.90%	-8.60%	-6.63%	-22.27%
Average $\Delta R/R$	-6.63%					

The experimental setup is explained in chapter 3. The input bias voltage V_{BIAS} is given using Agilent E3620A Power supply with constant DC Voltage of 1V. The Output Voltage is

measured using Keithley 2182A Nanovoltmeter. Input and output terminals are connected to the device by probing to bond pads with the help of 10 μ m probe tips and also the membrane is deflected using the similar type of probes. The membrane deflection is witnessed with the help of live display of the microscopic image provided by the measurement setup and the display of image during membrane deflection is shown in Figure 4.6.

The calculation of ΔV and $\Delta R/R$ for the maximum membrane deflection is done the same way as in for non-flexible devices. In the calculation, it is assumed that the change in resistance of A1 and A2 is equal and is taken as ΔR . The offset voltage V_{offset} is calculated using the resistance values of P1, P2, A1 and A2 for the V_{BIAS} of 1V. The output voltage V_1 is obtained practically for 1V of V_{BIAS} before the load application and then compared with V_{offset} value. If both the voltages are equal, then the device is further tested with load application. ΔV and $\Delta R/R$ for the maximum deflection of the membrane is obtained for two different type of devices.

Table 4.2 Complete description of the T4 device characterized.

Die Name	3.12	3.13	3.14	3.16	Average Resistance (Ω)	Standard Deviation/ Average Resistance
P1	2892	2921	2956	3138	2977	3.72%
A1	3083	3010	3058	3286	3109	3.91%
P2	2860	2872	2944	3084	2940	3.50%
A2	2997	3004	3052	3310	3091	4.79%
Average Resistance (Ω)	2958	2952	3003	3205	3029	3.93%
Standard Deviation	102	67	61	111	85	29.19%
Standard Deviation/ Average Resistance	3.44%	2.27%	2.03%	3.45%	2.80%	27.07%
V_{offset} (mV)	28.00	19.00	17.00	29.00	23.25	26.37%
V1 (mV)	28.12	19.22	18.21	29.79	23.83	25.03%
V2 (mV)	26.77	17.79	16.83	28.48	22.47	26.75%
ΔV (mV)	1.35	1.43	1.38	1.31	1.37	3.74%
ΔR	-328	-227	-218	-375	-287.074	-26.81%
$\Delta R/R$	-0.108	-0.0760	-0.0710	-0.114	-0.09225	-23.72%
$\Delta R/R$	-10.80%	-7.60%	-7.10%	-11.40%	-9%	-24%
Average $\Delta R/R$	-9.23%					

The results obtained during characterization are listed in Table 4.1 and Table 4.2. Four different devices of each type T3 and T4 were tested and the consistency of the measured ΔV result was observed with the standard deviation/average ΔV of 1.96% in case of T3 device and 3.74% for device T4. The Average $\Delta R/R$ obtained is 6.63% and 9.23% for the device T3 and T4 respectively. The results showed the maximum ΔV obtained is 1.43 mV for the bias voltage of 1V and the maximum $\Delta R/R$ obtained is 11.4%.

Using Load Cell

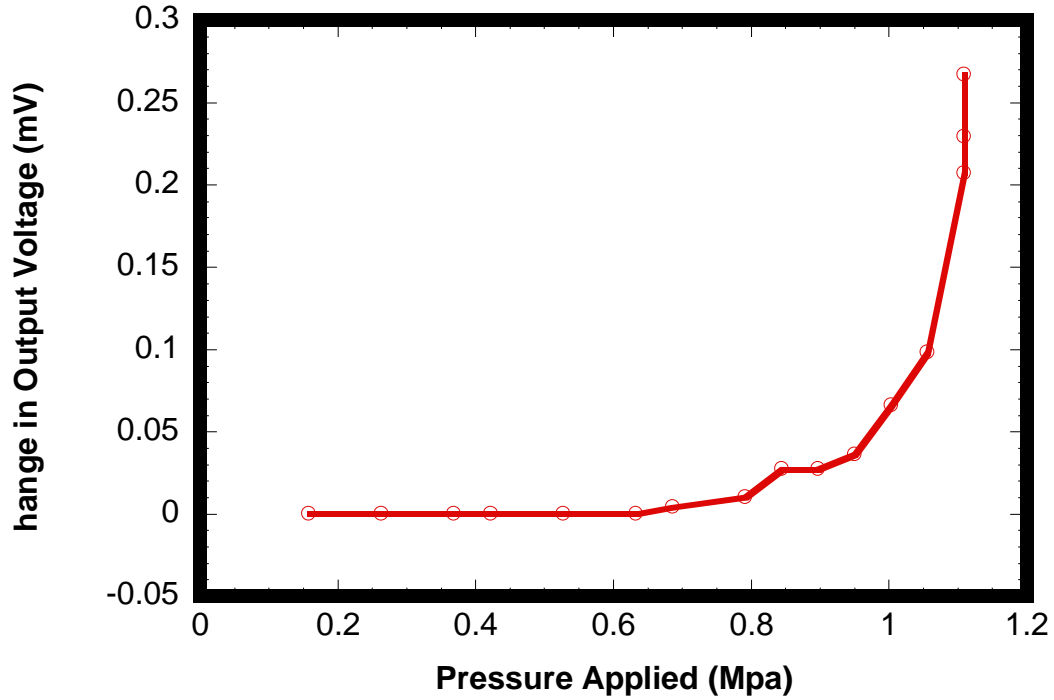


Figure 4.10 Load-cell result showing change in output voltage vs. pressure applied on the membrane for device T3.

The load cell measurement setup is explained in chapter 3. Similar to the non-flexible devices, the flexible devices were cut into individual dies and then bonded to the package the same way as explained in chapter 3 and the individual resistance is measured. Each time, with the help of nanopositioner, the probe tip is moved for $0.2\mu\text{m}$ in z-direction and the corresponding reading of mass applied on the membrane (in grams) was taken. Thus, the amount of force applied each time on the membrane is calculated by using the formula, $F = m \times a$ where 'F' is the force applied on the membrane, 'm' is mass of the load applied on the membrane and 'a' is acceleration due to gravity (9.81m/sec^2). The amount of pressure applied is then calculated using the formula $P = F/A$ where 'A' is the area of the

contact area between the probe-tip and the surface of the membrane similar to the method explained in the chapter 3.

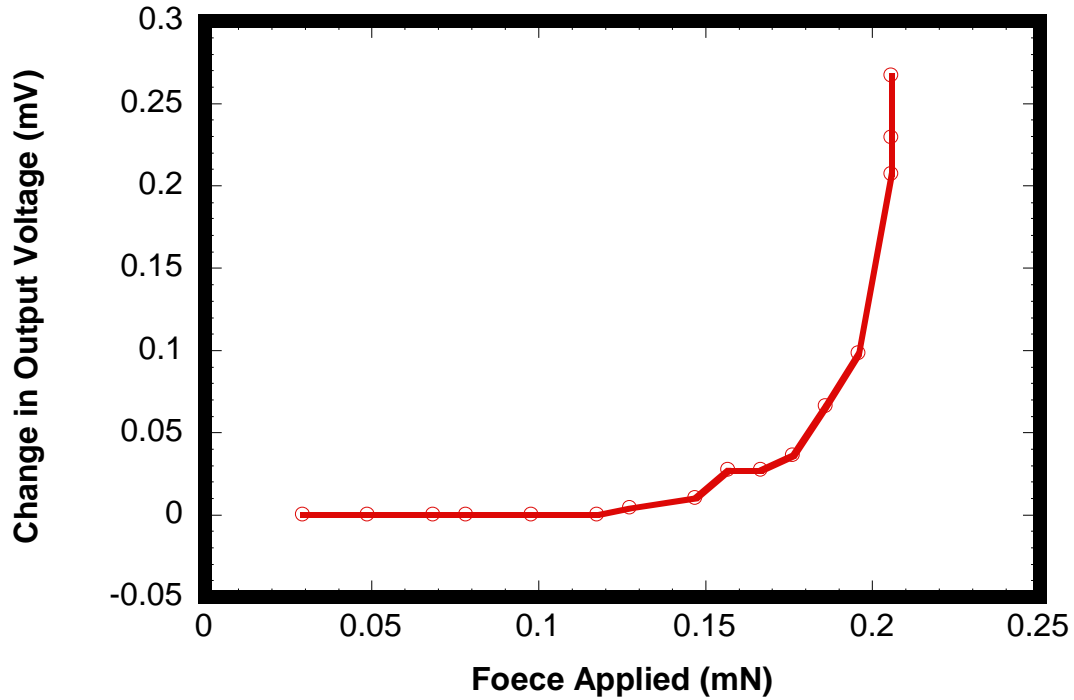


Figure 4.11 Load-cell result showing change in output voltage vs. force applied on the membrane for device T3.

The change in the output voltage versus the applied force and applied pressure was measured using load cell for 2 different types of devices. The sensitivity of the device can be calculated by taking the slope across the second linear region for the plots shown in Figure 4.10, Figure 4.11, Figure 4.12 and Figure 4.13. The device T3 has the sensitivity of 1.7155 mV/Mpa and 9.2538 mV/mN and device T4 has the sensitivity of 0.8766 mV/Mpa and 3.1152 mV/mN.

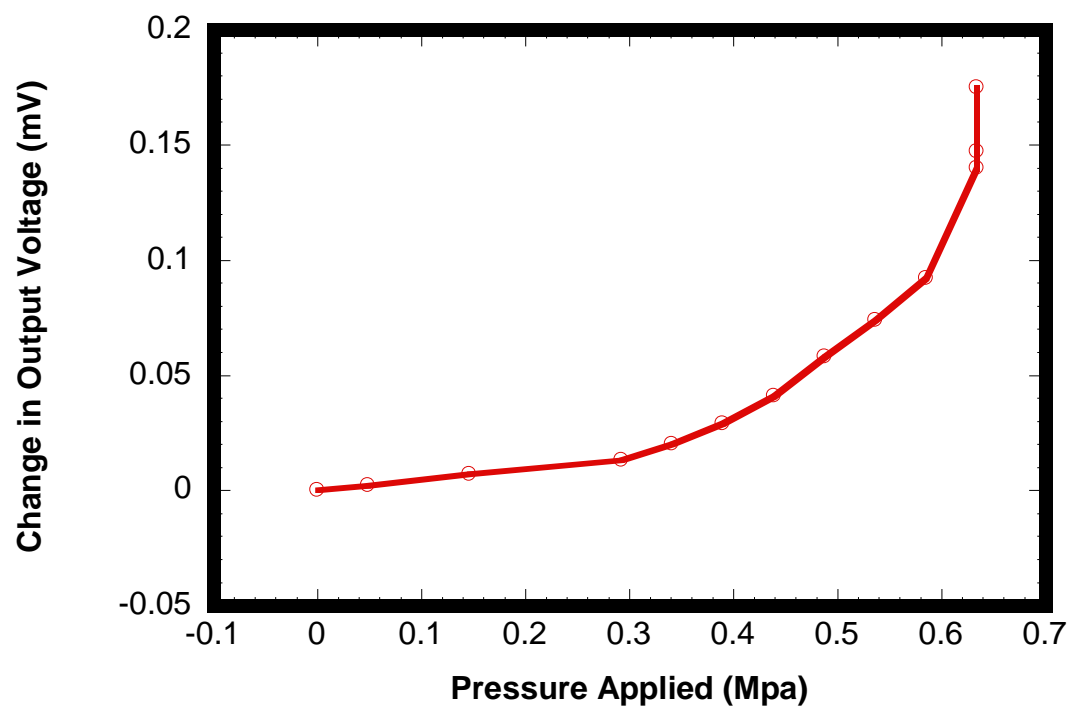


Figure 4.12 Load-cell result showing change in output voltage vs. pressure Applied on the membrane for device T4.

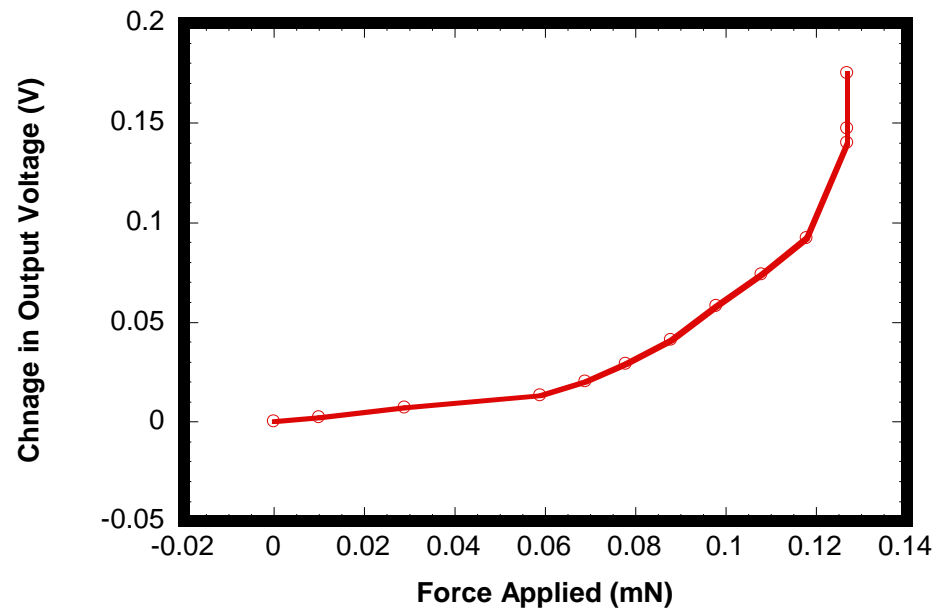


Figure 4.13 Load-cell result showing change in output voltage vs. force applied on the membrane for device T4.

CHAPTER 5

DEVELOPMENT OF MICRO PRESSURE SENSOR USING CNT/POLYMER NANOCOMPOSITES AS PIEZORESISTOR

5.1 Introduction

Since the discovery of the carbon nanotubes (CNTs) [45], many researchers are trying to understand and explore the use of CNTs in various fields. Due to its exceptional mechanical and physical properties, CNTs are likely candidates not only for composite structures but also for multifunctional CNT nanocomposites with tailored electrical and thermal properties. The challenges involved in the processing of CNT nanocomposites are homogeneous dispersion and creating strong interfacial bonding between CNT and polymer matrix [46]. CNTs due to their nanometer scale have strong van der Waals forces between them. And also CNTs get entangled with each other easily due to high aspect ratio in their structure.

This chapter explains the development of CNT/polymer nanocomposites for the pressure sensor application where some of the problems mentioned above are addressed. And also the fabrication of micro pressure sensor via surface micromachining where CNT/polymer nanocomposites were used as piezoresistor.

5.2 Methodology

Due to the mechanical force applied, CNT (carbon nanotube) composites undergo morphological changes in the network structure of the filler in the polymeric matrix resulting in change in resistivity. There will be a change in inter-particle separation between CNTs in the matrix, resulting in change in resistance in the conductive composites. [47]

5.3 Preparation of CNT/Nanocomposites

Using CNT and PVDF

The piezoresistive behavior of nanocomposites made of polyvinylidene fluoride (PVDF) and CNTs has been showed by Shailesh et. al [47] and the recipe involved in preparing the solution is explained in this paragraph. PVDF, which was in the powder form, was mixed with Dimethyl formamide (DMF) to get a liquid solution of PVDF/DMF which can be deposited on to the wafer using the spin coat method where the DMF gets evaporated instantly after the spin leaving PVDF on the sample. 6 grams of PVDF was added to 60 ml. of DMF and mixed together by continuously stirring at 150 rpm for 12 hours to form a homogenous mixture of PVDF/DMF. To this solution, MWCNTs are added by continuous stirring to form the solution of MWCNT/PVDF/DMF which was later deposited on to the wafer using the spin coat method. MWCNTs were added to the previously prepared PVDF/DMF solution, mixed thoroughly by stirring it at 150 rpm. Four different solutions of MWCNT/PVDF/DMF were prepared by varying the concentration of MWCNT each having 1,2,3 and 4 wt% of PVDF content.

The solution prepared like this was deposited on the sample by spin-coat method where DMF gets evaporated instantly after the spin leaving a layer of MWCNT/PVDF on the sample and the solution prepared was spun at different speeds in order to find the optimum spread of CNTs on the sample. After this, the CNT/PVDF film was etched using the Technics Micro-RIE (Reactive ion etching) with the RF power of 150 watts at the chamber pressure of 200 mtorr with the gas flow of 3 sccm of CF_4 and 7 sccm of oxygen as a test.

Pattern of MWCNT/PVDF layer

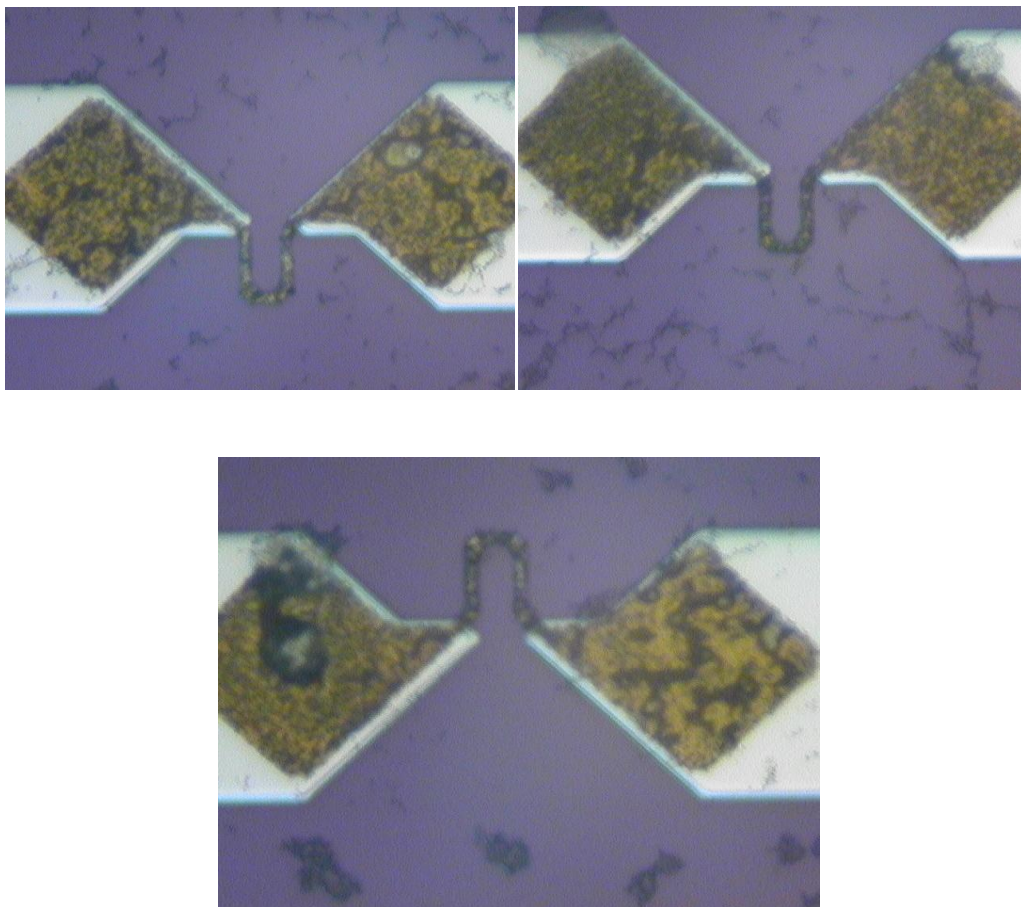


Figure 5.1 PVDF pattern after 90 min. of RIE etch.

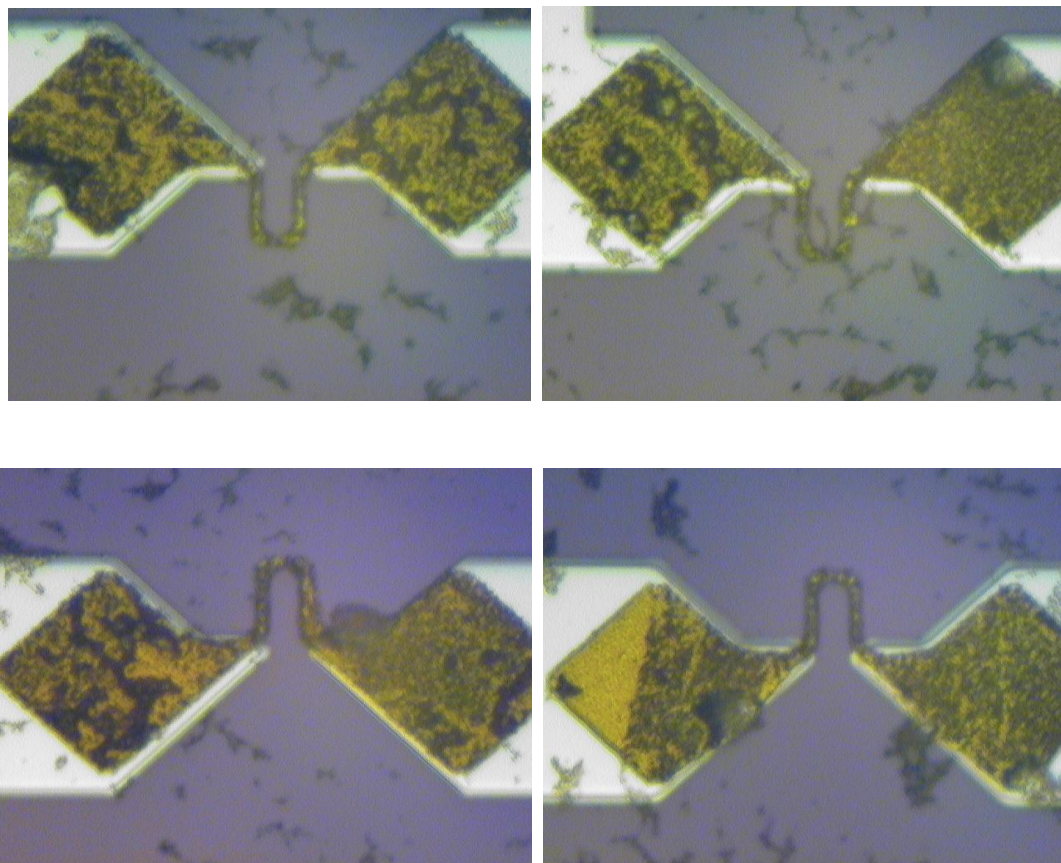


Figure 5.2 PVDF pattern after 120 min of RIE etch.

A test sample was prepared to try out the patterning of MWCNT/PVDF by depositing 500 nm thick aluminum oxide on top of the clean silicon wafer using AJA ATC Orion series UHV sputter system at room temperature under the gas flow of 30 sccm of argon with the chamber pressure of 5mT using 150 W RF power. Then a previously prepared solution of MWCNT/PVDF/DMF is spin coated on top aluminum oxide layer at 2000 rpm and let stand for 10 min to allow the DMF to evaporate completely leaving only MWCNT/PVDF structure. On top of this layer, NR-9 1500 PY (Futurrex) negative resist was spin coated and patterned with the metallization contact layer mask. Then a layer of 300-nm-thick gold was deposited

using RF magnetron sputtering (Home-built sputter system) at 10 mTorr chamber pressure using 60 W RF power supply with the gas flow of 50 sccm of Argon. Then the deposited gold was patterned by doing the liftoff process using Microposit Remover 1165 to form the piezoresistor liftoff layer. Then, the sample is etched using the RIE with an RF power of 150 watts at the chamber pressure of 200 mtorr with the gas flow of 3 sccm of CF_4 and 7 sccm of oxygen for 90 to 120 minutes as shown in Figure 5.1 and Figure 5.2. Later gold layer is removed by gold etchant leaving the pattern of CNT/PVDF. Even though the pattern was successful, the MWCNT/PVDF layer had problems as they were getting removed with the acetone or 1165 resist remover which made impossible to achieve the fabrication of other layers on top of MWCNT/PVDF layer due to involvement of liftoff technique.

Aggregation of CNT

Due to problems involved in the usage of CNT/PVDF, different polymer materials were tried to mix the CNTs. Among all the available polyimides, HD4110 (HD Microsystems) has been chosen along with thinner T-9039 (HD Microsystems). HD4110 is mixed with thinner T-9039 to make it less viscous and CNTs were added to the solution. But, the CNTs tend to get aggregated in polyimide; hence it was treated with DMF by mixing it at 150 rpm for 12 hours before adding polyimide.

Using CNT and Polyimide

Initially polyimide HD4110 (HD Microsystems) is made less viscous by adding thinner T-9039 (HD Microsystems) in 1:1 (Volume Ratio) and kept stirring for overnight. For the reference this solution is taken as 'A'.

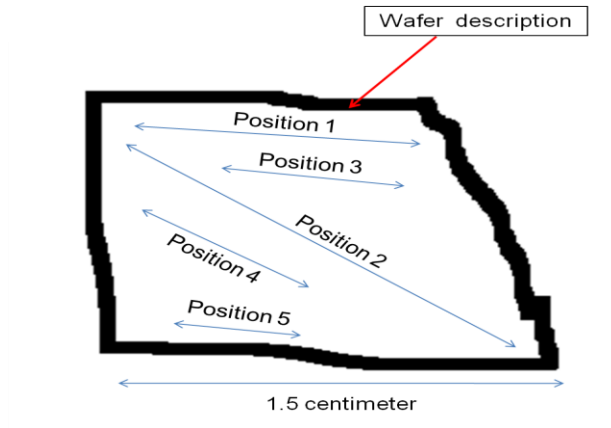
Then 40 ml of DMF is added to the 10 ml of solution 'A' and mixed thoroughly by stirring it for 12 hours. This solution is called 'B'.

0.8 grams of MWCNT is added to 10 grams of DMF mixed thoroughly by stirring for 24 hours at the speed of 150 rpm. DMF will break the MWCNTs into length and reduces the aggregation. For the reference this solution is taken as 'C'.

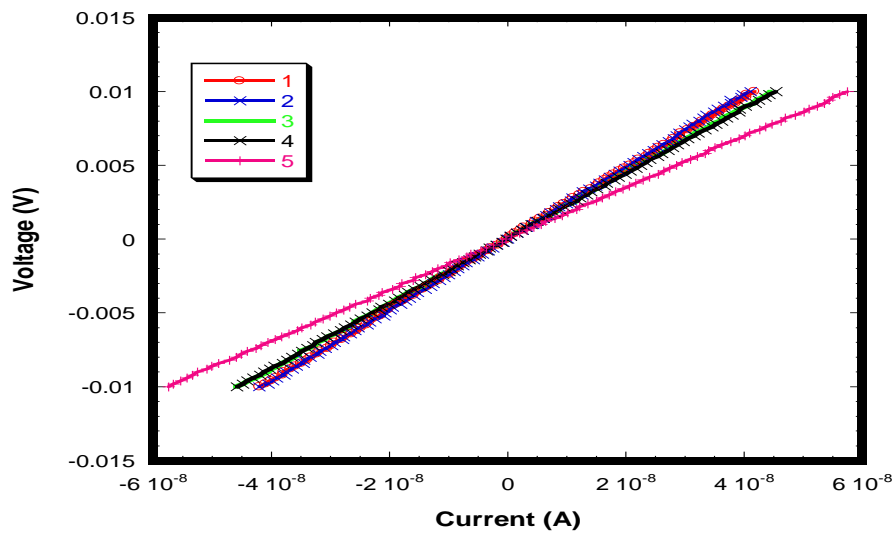
Both the solution 'B' and 'C' are mixed together by stirring continuously for 2 hours at 200 rpm. Then the solution is kept in ultrasonic agitation for 1 hour before the spin-coat.

Conduction of CNT/polyimide nanocomposite

Different compositions of CNTs were tried in the solution and also CNT/polyimide/DMF solution is spun at different speeds and each time the sample is tested for the conductivity to determine the spread of CNTs all over the sample. The Figure 5.3 shows the conductivity of CNT/polyimide nanocomposite deposited using spin-coat method and measured across the sample by probing at random areas on the sample.



(a)



(b)

Figure 5.3 CNT/polyimide conductivity test at different areas of the sample (a) wafer mapping (b) IV curve taken probing across different areas of sample after CNT/polyimide/DMF solution spin coat.

Pattern of CNT/Polyimide nanocomposite

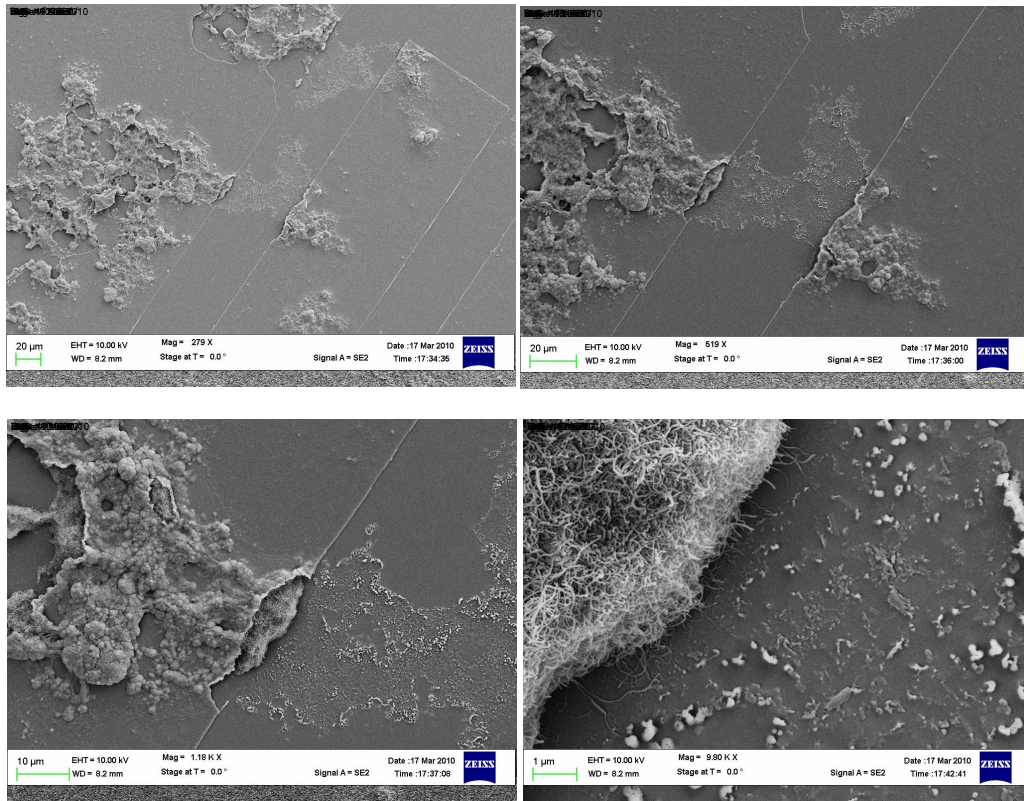


Figure 5.4 SEM images of device pattern in the increasing order of the magnification form top-left to bottom-right.

The CNT/polyimide etch was tried the same way as for the CNT/PVDF sample using the RIE with the gas flow of CF_4 and oxygen in the ratio 3:7 respectively. After getting the etch recipe, the pattern of CNT/polyimide was established by using thin layer of aluminum oxide as etch mask. A test sample is prepared by depositing 500nm aluminum oxide on top of the clean silicon wafer using AJA ATC Orion series UHV sputter system at room temperature under the gas flow of 30 sccm of argon with the chamber pressure of 5mT using 150 W RF power. Then, the CNT/polyimide/DMF solution was spin coated on top of the

aluminum oxide layer at 2000rpm for 25 seconds and cured at 200 °C for 4 hours in nitrogen gas environment with a ramp up and ramp down rate of 1.5 °C/min.

On top of this layer, NR-9 1500 PY (Futurrex) negative resist was spin coated and patterned with the contact layer mask. Then a layer of 100-nm-thick aluminum oxide membrane layer was deposited by AJA ATC Orion series UHV sputter system at room temperature under the gas flow of 30 sccm of argon with the chamber pressure of 5mT using 150 W RF power. Then the deposited aluminum oxide was patterned by doing the liftoff process using Microposit Remover 1165 to form the etch mask layer.

Then the sample is etched using RIE with the RF power of 300 watts at the chamber pressure of 300 mtorr with the gas flow of 4.2 sccm of CF₄ and 10 sccm of oxygen for 6 hours. During this the polyimide will be removed along with CNTs forming the pattern of piezoresistor layer which was protected by aluminum oxide mask.

The CNT/polyimide etched like this leaves some CNT residue after the etch and the sample was then cleaned in 1165 resist remover by ultrasonic agitation for 5 min followed by rinse in acetone, methanol and DI water each for 2 min. Though etch was good with the pattern formation of metallization layer, still some residue was left due to improper spread of CNTs on the sample during the spin coat of CNT/polyimide/DMF solution. Also it was observed that more CNTs get trapped in the trench areas of the sample during the spin coat. Hence a new technique with both the liftoff and etch was tried to pattern the CNT/polyimide layer successfully. Hence, a layer of chromium was deposited and patterned leaving a trench at the piezoresistor area. This enables the CNTs to get trapped into piezoresistor area during the CNT/polyimide/DMF spin coat and later after the CNT/polyimide etch, the chromium is removed by wet etch making it work like the lift-off technique. This technique

removed the residue of CNTs left behind after RIE etch as seen in Figure 5.4 which is etched using the contact layer mask explained in chapter 2.

5.4 Fabrication

Before fabrication, the wafers were degreased using trichloroethylene, followed by a rinse in acetone, methanol and DI water. After that, these wafers underwent acid cleaning in 3:1 $\text{H}_2\text{SO}_4:\text{H}_2\text{O}_2$ and 6:1 BOE followed by DI water rinse and dehydration bake at 100 °C for 5 minutes. Before each fabrication step, wafers were cleaned in acetone and methanol, followed by DI water rinse and dehydration bake. Sputtering at room temperature was used for thin film deposition while etch and lift-off techniques were used to pattern the structures. All photolithography was performed using OAI Model-806 i-line contact aligner.

Initially, 0.4- μm -thick silicon-nitride was deposited on the silicon wafer using an AJA ATC Orion series UHV sputter system at room temperature under the gas flow of 30 sccm of Argon and 5 sccm of N_2 with the chamber pressure of 2.8mT using 150 W RF power. This layer provides passivation as well as good adhesion for the subsequent polyimide layer. Next, the sacrificial polyimide PI 2611 (HD Microsystems) was spin coated at 4000rpm for 50 seconds followed by bake at 110 °C for 5 minutes on hot plate and cured at 300 °C for 8 hours in nitrogen gas environment with a ramp up and ramp down rate of 1.5 °C/min, resulting in a final thickness of 5 μm .

Before depositing the membrane layer, LOR 15B (Microchem) was spin coated at 2500 rpm for 40 seconds followed by hot plate bake at 150 °C for 3 minutes to act as the undercut resist. Then S1813 (Shipley) positive photoresist was spin coated on top of LOR 15B at 2500 rpm for 40 seconds and patterned using membrane layer mask. Then, the 1.2- μm -thick aluminum oxide membrane layer was deposited by AJA ATC Orion series UHV

sputter system at room temperature under the gas flow of 30 sccm of argon with the chamber pressure of 5mT using 150 W RF power. After the deposition of membrane, trenches were opened by lift-off in Microposit Remover 1165 (Shipley).

On top of this layer, NR-9 1500 PY (Futurrex) negative resist was spin coated and patterned with the metallization contact layer mask. Then a thin layer of 300-nm-thick aluminum was deposited by AJA ATC Orion series UHV sputter system at 2.8 mTorr chamber pressure using 150 W RF power with the gas flow of 30 sccm of argon. Then aluminum layer is lifted off using Microposit Remover 1165 to form the interconnect layer.

On top of this layer, S1813 (Shipley) positive photoresist was spin coated at 1000 rpm for 40 seconds and patterned with the piezoresistor layer mask. Then a layer of 600-nm-thick chromium was deposited using RF magnetron sputtering (Home-built sputter system) at 10 mTorr chamber pressure using 60 W RF power supply with the gas flow of 50 sccm of Argon. Then the deposited chromium was patterned by doing the liftoff process using Microposit Remover 1165 to form the piezoresistor liftoff layer as shown in Figure 5.5. This leaves the trench in the piezoresistor area and helps in trapping the CNTs during the spin-coat.

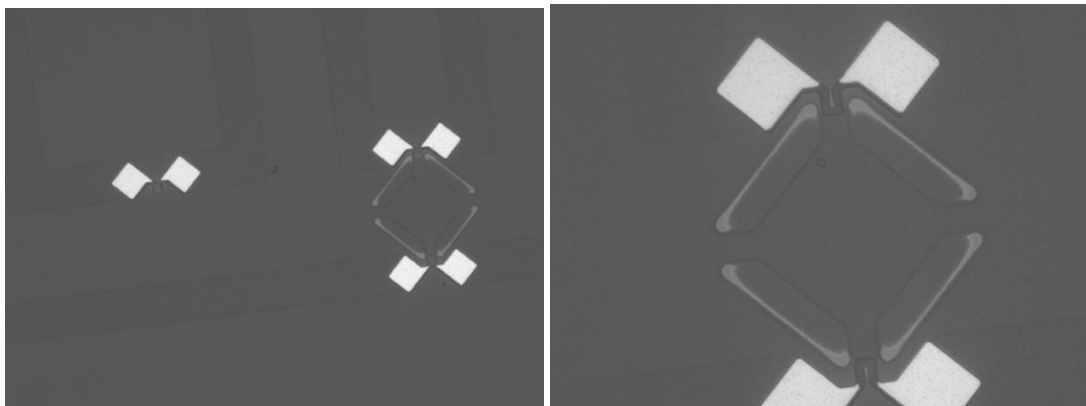


Figure 5.5 Chromium layer liftoff.

Then the solution containing CNT/polyimide and DMF was spin coated on top of this layer at 2000 rpm for 30 seconds followed by bake at 90 °C for 2 minutes on hot plate and cured at 200 °C for 4 hours in nitrogen gas environment with a ramp up and ramp down rate of 1.5 °C/min, resulting in a final thickness of 2μm.

On top of this layer, NR-9 1500 PY (Futurrex) negative resist was spin coated and patterned with the piezoresistor layer mask. Then a layer of 100-nm-thick aluminum oxide membrane layer was deposited by AJA ATC Orion series UHV sputter system at room temperature under the gas flow of 30 sccm of argon with the chamber pressure of 5mT using 150 W RF power. Then the deposited aluminum oxide was patterned by doing the liftoff process using Microposit Remover 1165 to form the piezoresistor etch mask layer as shown in Figure 5.6.

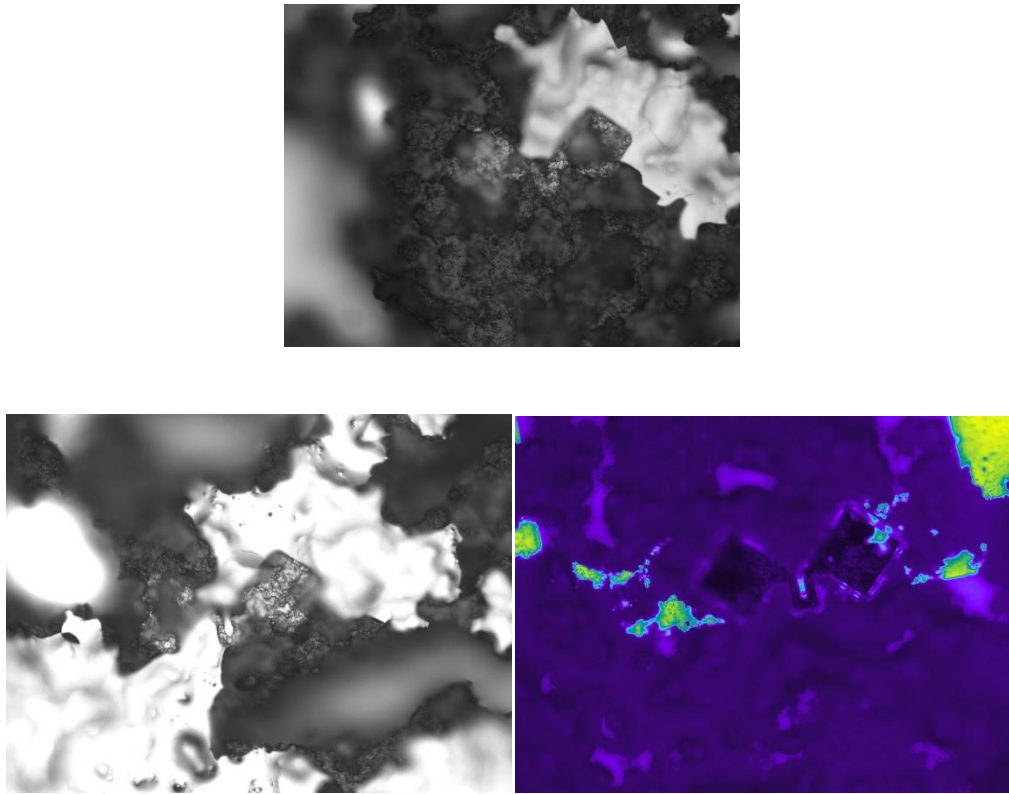


Figure 5.6 Aluminum oxide mask layer liftoff.

Then the sample is etched using RIE with RF power of 300 watts at the chamber pressure of 300 mtorr and the gas flow of 4.2 sccm of CF₄ and 10 sccm of oxygen for 2 hours. During this, the polyimide will be removed along with CNTs forming the pattern of piezoresistor layer which was protected by aluminum oxide mask as shown in Figure 5.7 and 5.8. Then the sample was cleaned in 1165 resist remover by ultrasonic agitation for 5 min followed by rinse in acetone, methanol and DI water each for 2 min. The CNT residue leftover will be removed by liftoff process where the exposed chromium is removed by wet etch using chromium etchant by ultrasonic agitation for 10 min and the microscopic image of

sample after the liftoff technique is shown in Figure 5.9. After this the sample is rinsed in DI water leaving the piezoresistor structure made of CNT/polyimide nanocomposite.

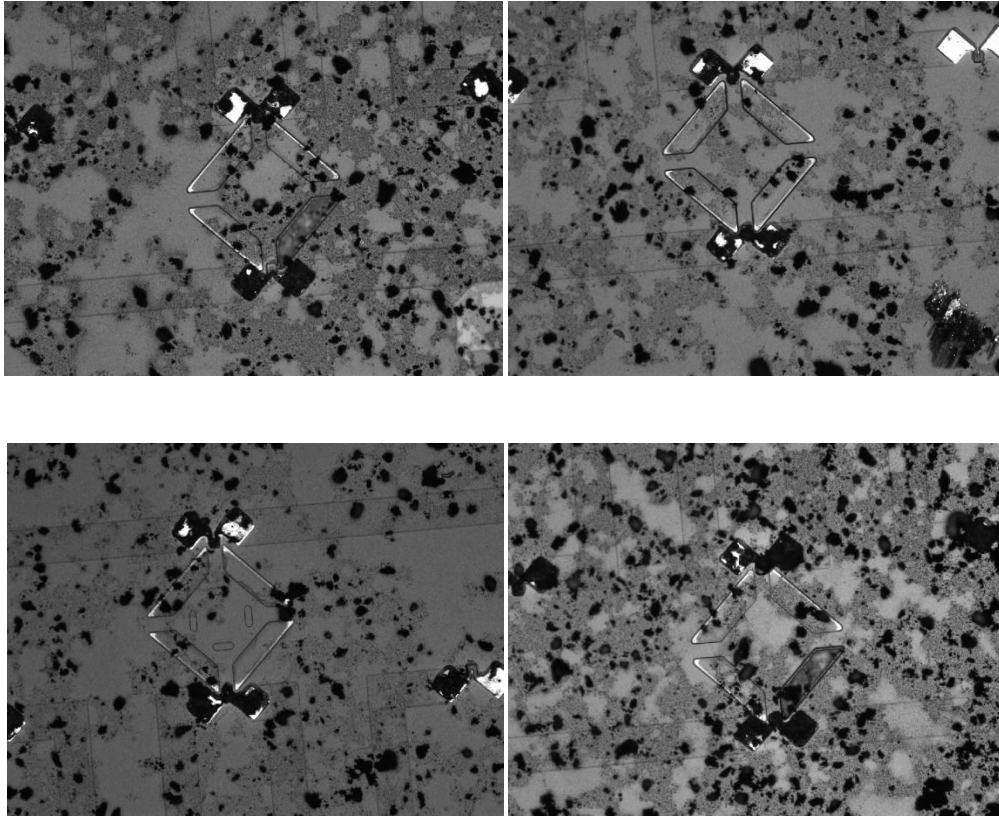


Figure 5.7 Confocal images of device sample at different areas on the sample showing different devices after 2 hours of RIE etch.

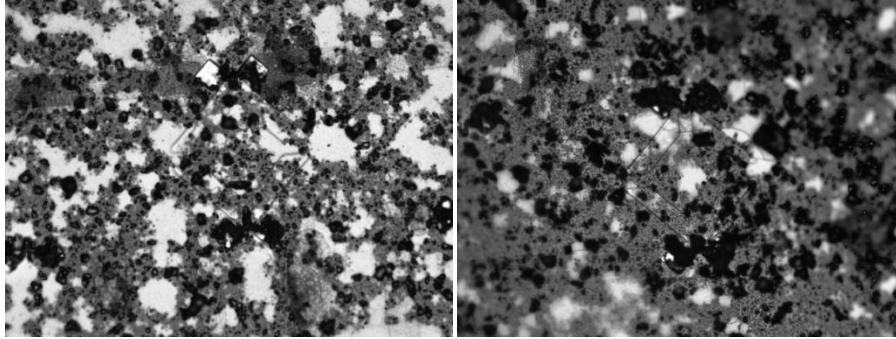


Figure 5.8 Another sample after 100 min. of RIE etch.

The sacrificial layer will be removed by the ashing step but during this step the CNT/polyimide will be getting removed where ever it is exposed to oxygen. Hence a thick layer of 2.2- μm -thick aluminum oxide is covered the surface of entire wafer except the trenches and the contact pads. This layer provides the covering to the piezoresistors even on the edges since the thickness of the piezoresistors is around 2 μm . This layer also covers the roughness created during the spin coat of CNT/polyimide.

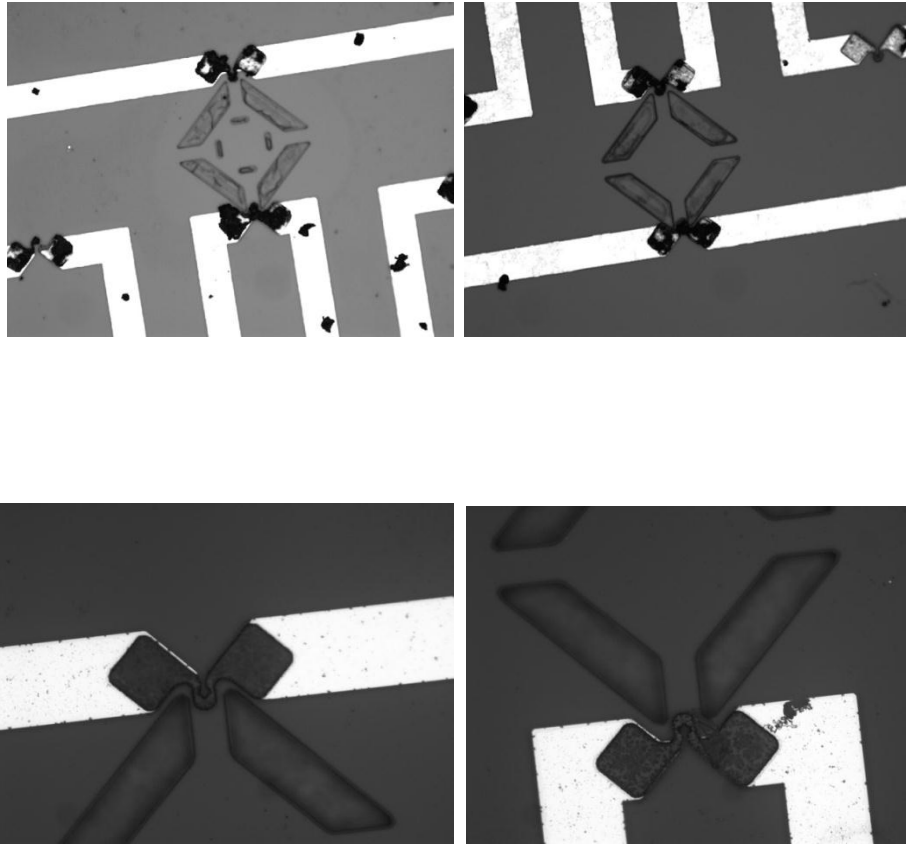


Figure 5.9 After 10 min of chromium etch used as liftoff technique.

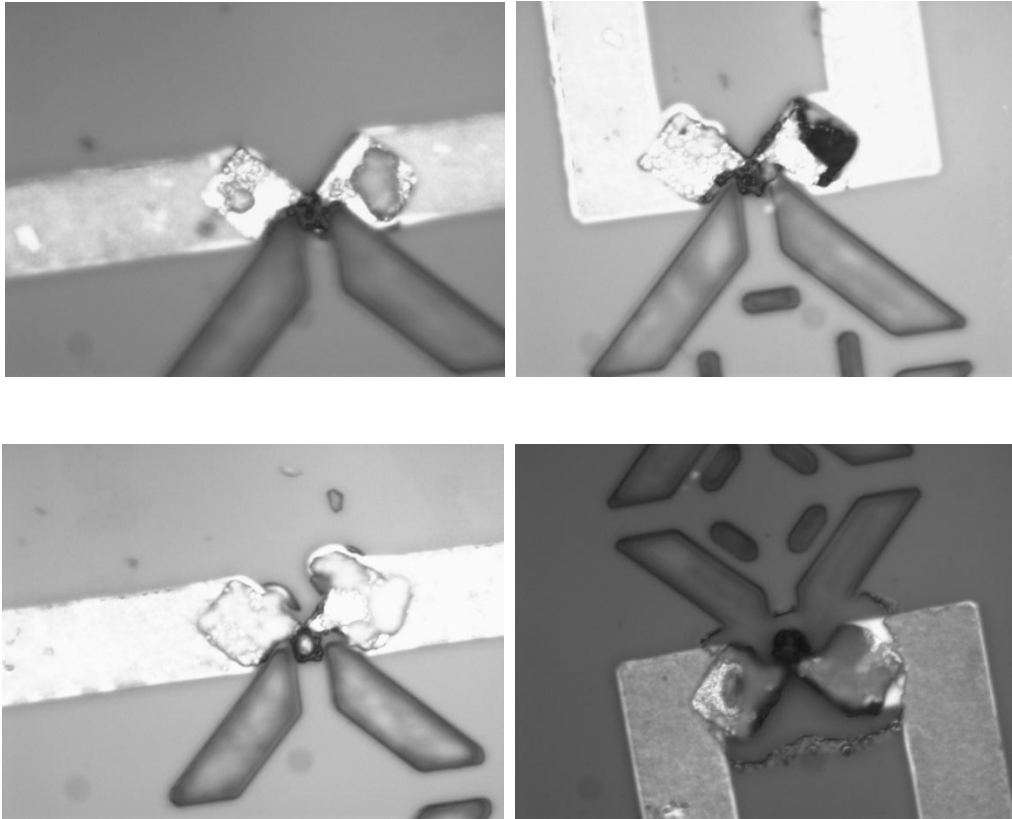
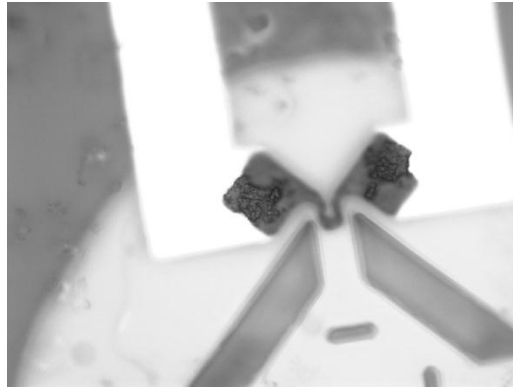


Figure 5.10 After complete device fabrication.

The fabrication of this layer involves the deposition and pattern of NR-9 1500 PY photoresist using ashing cover layer mask and deposition of aluminum oxide layer using AJA ATC Orion series UHV sputter system at 2.8 mTorr chamber pressure using 150 W RF power with the gas flow of 30 sccm of argon. Then the aluminum oxide is lifted off using Microposit Remover 1165 to form the structure covering the entire wafer except the trenches and the contact area. After this, the sample is ashed in the plasma asher (Diener Electronics Asher) with the gas flow of oxygen under the chamber pressure of 0.6 mbarr using 150 W RF power for 100 hours. During this the machine is stopped for few hours per every 10 hours of ashing. After this step membrane structure is released to form a suspended structure on top of polyimide layer. The IV curves of individual resistor across two complete devices are shown in Figure 5.11 and 5.12.

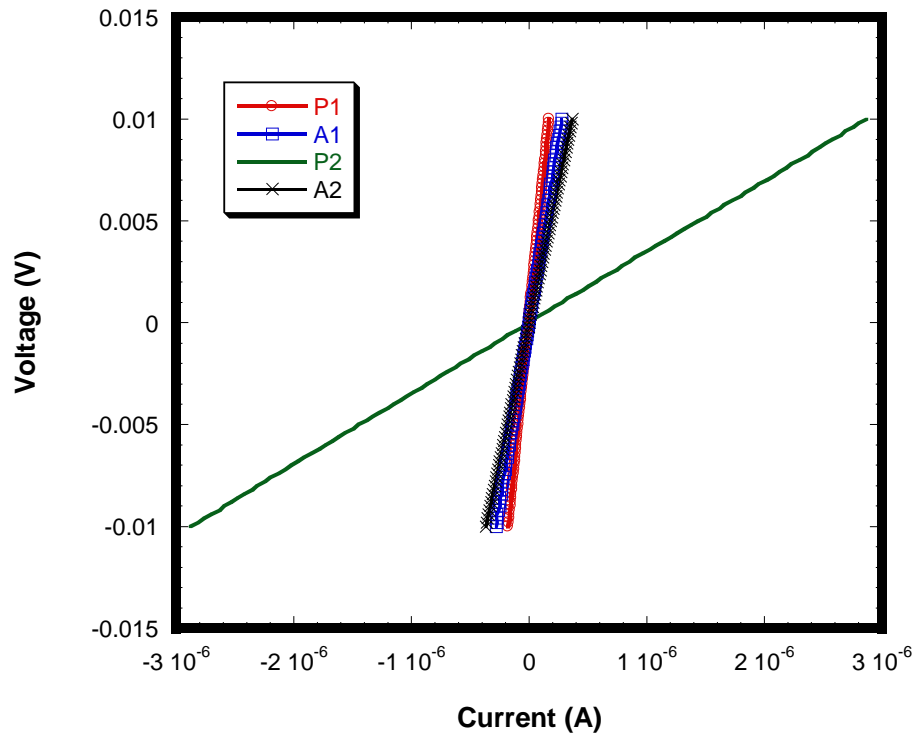


Figure 5.11 IV curve of individual resistors of device 1.

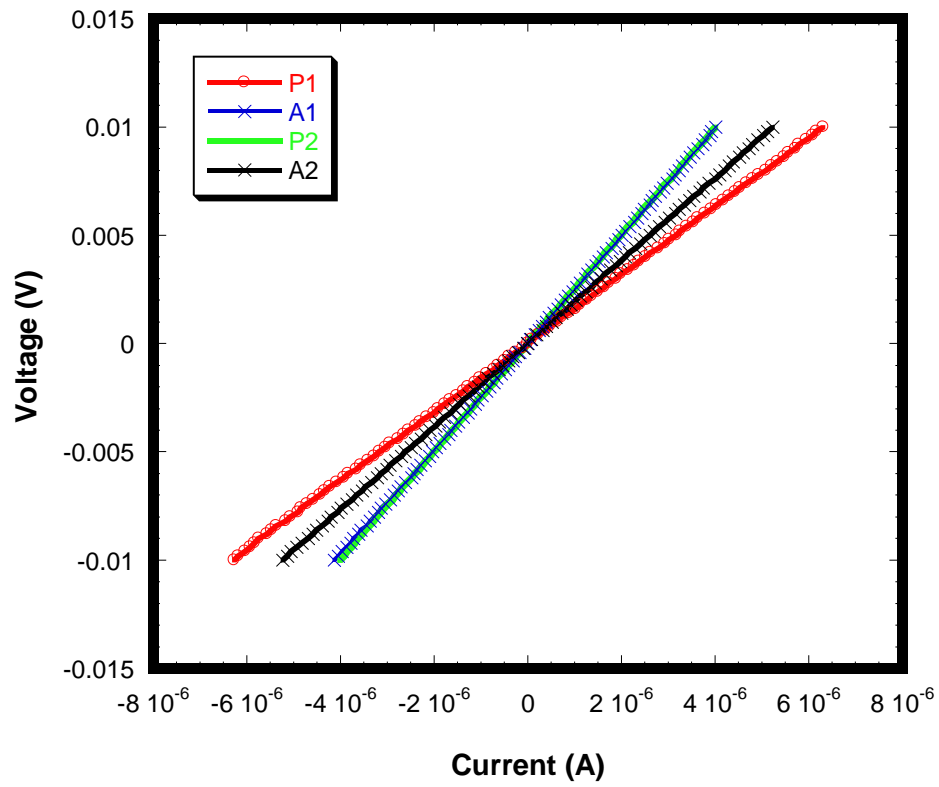


Figure 5.12 IV curve of individual resistors of device 2.

CHAPTER 6

CONCLUSIONS

Micro pressure sensors using nichrome as piezoresistor were fabricated on silicon substrate. The sensitivity of the fabricated devices was tested for 9 different designs which differ in dimensions of membrane and piezoresistor and also for three different thickness of piezoresistive material. The fabrication was performed via IC compatible surface micromachining process with a maximum process temperature of 300 °C. Characterization of the fabricated devices was done using two different types of testing. The first type of testing was performed using electrical probe station for full membrane deflection and the second type was using load cell measurement by varying the amount of pressure applied on top the membrane. The change in voltage (ΔV) for full deflection of membrane was obtained using probe station measurement. The device response for the force/pressure application on top of the membrane in terms of change in voltage (ΔV) was obtained using load cell measurement system. Using the measured ΔV , change in resistance (ΔR) is calculated. The repeatability and consistency of the ΔV was also observed when the load was applied on the device several times. The tested results showed the maximum change in resistance of 12% when the membrane is fully deflected. Gauge factor (GF) for the nichrome piezoresistor for the fabricated devices was obtained using the measured result and the simulated result.

The micro pressure sensors were then fabricated on flexible substrates using polyimide as substrate and nichrome as piezoresistor. The devices fabricated on flexible substrate were also tested using the probe station and load cell measurement system similar to the non-flexible devices. The device response ΔV and ΔR were obtained during the

measurement which was comparable to results obtained from non-flexible devices and GF of nichrome was also observed for nichrome for the devices fabricated on flexible substrate.

Nanocomposites using CNT and polyimide were developed for pressure sensing application and can be deposited using spin-coat method. Electrically conductive CNT/polyimide nanocomposites were achieved after depositing on the wafer using spin-coat method by varying the concentration of CNTs and polyimide. The challenge in developing the nanocomposites was aggregation of CNTs and was successfully reduced by treating CNTs with DMF before adding into the polyimide. Different compositions of CNTs were tried in the CNT/polyimide solution and also the spin speed was varied to achieve uniform and electrically conductive nanocomposites. The deposited CNT/polyimide nanocomposite was patterned using the combination of RIE as well as liftoff technique to form the piezoresistive structure on top of the aluminum oxide membrane. The micro pressure sensor using CNT/polyimide nanocomposites as piezoresistor was fabricated and the individual resistance of the piezoresistor across Wheatstone bridge network was measured.

REFERENCES

- [1] Mohamed Gad-el-Hak, MEMS Introduction and fundamentals, Taylor & Francis Group, LLC, 2006, pp, 2-3.
- [2] J. Engel, J. Chen, and C. Liu, "Development of polyimide flexible tactile sensor skin", J. Micromech. Microeng., vol.13, pp. 359-366, 2003.
- [3] Z. Celik-Butler and D. P. Butler, "Flexible sensors-A review", J. Nanoelectron. Opt., vol.1, pp. 194-202, 2006.
- [4] V. Vong and A. Salleo, Flexible electronics: Materials and applications, Springer Science and Business Media, New York, NY, USA, 2009
- [5] M. D. J. Auch, O. K. Soo, G. Ewald, and C. Soo-Jin, "Ultrathin glass for flexible OLED application", Thin Solid Films, vol. 417, no. 1-2, pp. 47-50, September 2002
- [6] Y. H. Kim, S. K. Park, D. G. Moon, W. K. Kim, and J. I. Han, "Organic thin film transistor-driven liquid crystal displays on flexible polymer substrate", Jap. J. Appl. Phys., vol. 43, no. 6a, pp. 3605-3608, 2004.
- [7] J. H. Cheon, J. H. Bae, and J. Jang, "Mechanical stability of poly-Si TFT on metal foil", Solid-State Electron., vol. 52, no. 3, pp. 473-477, 2008
- [8] S. U. Jen, C. C. Yu, C. H. Liu, and G. Y. Lee, "Piezoresistance and electrical resistivity of Pd, Au, and Cu films", Thin Solid Films, vol. 434, Iss. 1-2, pp. 316-322, June 2003
- [9] Julian W. Gardner, Vijay K. Vardan, Osama O. Awadelkarim, Microsensors, MEMS and Smart Devices, John Wiley & Sons, Inc., 2001, pp. 1-7.
- [10] S. U. Jen, C. C. Yu, C. H. Liu, and G. Y. Lee, "Piezoresistance and electrical resistivity of Pd, Au, and Cu films", Thin Solid Films, vol. 434, Iss. 1-2, pp. 316-322, June 2003
- [11] C. S. Smith, "Piezoresistance effect in germanium and silicon", Phys. Rev., vol. 94, no. 1, pp. 42-49, 1954
- [12] E. N. Adams, "Elastoresistance in p-type Ge and Si", Phys. Rev., vol. 96, no. 3, pp. 803-804, 1954.

- [13] C. J. Reilly and J. E. Sanchez, Jr, "The piezoresistance of aluminum alloy interconnect structures", J. Appl. Phys., vol. 85, no. 3, pp. 1943-1948, February 1999.
- [14] C. Hu, Y. Gao, and Z. Sheng, "The piezoresistance coefficients of copper and copper-nickel alloys", J. Mat. Sci., vol. 35, pp. 381-386, 2000.
- [15] A. A. Barlian, W. -T. Park, J. R. Mallon, Jr, A. J. Rastegar, and B. L. Pruitt, "Review: Semiconductor piezoresistance for Microsystems", Proc. IEEE, vol. 97, no. 3, pp. 513-552, March 2009.
- [16] A. L. Window and G. S. Holister, Strain gauge technology, Applied Science Publishers, London and New Jersey, 1982.
- [17] Stephen D. Senturia, Microsystem design, Kluwer academic publishers, 2001, pp 470-471
- [18] P. J. French and A. G. R. Evans, "Polycrystalline silicon as a strain gauge material", J. Phys. E.: Sci. Instrum., vol. 19, pp. 1055-1058, 1986
- [19] P.M. Ajayan, P. Redlich, M. Rühle; "Structure of carbon nanotube-based nanocomposites," Journal of Microscopy, vol 185, February 1997, 275-282.
- [20] H.J. Gao, B. H. Ji, I.L. Jäger, E. Arzt, P. Fartzl, "Materials become insensitive to flaws at nanoscale: Lessons from Nature," Proceedings of the National Academy of Sciences of the United States of America 100(10), May 13 2003, pp. 5597-5600.
- [21] P.J.F. Harris; "Carbon nanotubes and related related structures," Cambridge University Press, 2001.
- [22] Suresh G. Advani, Processing and properties of Nanocomposites, World Scientific Publishing Co. Pte. Ltd., 2007, pp 1-7.
- [23] T. Pancewicz, R. Jachowicz, Z. Gniazdowski, Z. Azgin, and P. Kowalski, "The Empirical Verification of the FEM Model of Semiconductor Pressure Sensor", Sensor and Actuators, 76, pp.260-265, 1999.
- [24] Lin, C. T., Peng, C. T., Lin, J. C. and Chiang, K. N., "Analysis and Validation of Sensing Sensitivity of a Piezoresistive Pressure Sensor", InterPACK2003 (IEEE/ASME), June 30 – July 5, Hawaii, USA.
- [25] James F. Shackelford, William Alexander, CRC Materials Science and Engineering Handbook, third ed., CRC Press, 2001 pp. 509.
- [26] James F. Shackelford, William Alexander, CRC materials science and engineering handbook, third ed., Press, 2001 pp. 538.

- [27] David T. Read, Yi-Wen Cheng, Robert R. Keller, and J. David McColskey, Tensile properties of free-standing aluminum thin films, *Scripta Materialia* 45 (2001) 583-589.
- [28] Tamayo J, Humphris A, Malloy A and Miles M, Chemical sensors and biosensors in liquid environment based on microcantilevers with amplified quality factor, *Ultramicroscopy* 86 (2001) 167-173.
- [29] Li J, Kahrizi M and Landsberger L Design, fabrication and characterization of CMOS-compatible optical microswitches, *IEEE Conf. Proc.*, 1 2003 319–22.
- [30] Kurt E. Petersen, Silicon as a Mechanical Material, *Proceedings of IEEE*, Vol. 70, No.5, (May 1982) pp.421.
- [31] Z. Xue, Y. Huang and M. Li, Particle size effect in metallic materials: a study by the theory of mechanism-based strain gradient plasticity, *Acta Materialia* 50 (2002) 149-160.
- [32] Vinayak Shamanna, Sharmita Das, Zeynep Celik-Butler, and Donald P. Butler, "Micromachined integrated pressure-thermal sensors on flexible substrates," *Journal of Micromechanics and Microengineering* 16, pp. 1984-1992 (2006).
- [33] Imam H.Kazi, P.M.Wild, T.N.Moore, M.Sayer, "The electromechanical behavior of nichrome (80/20 wt.%) film", *Thin Solid Films*, 433, pp.337–343, 2003.
- [34] Imam H.Kazi, P.M.Wild, T.N.Moore, M.Sayer, "The electromechanical behavior of nichrome (80/20 wt.%) film", *Thin Solid Films*, 433, pp.337–343, 2003
- [35] M.A. Angadi, R. Whiting, "Longitudinal and transverse strain sensitivity of nichrome films," *Mater.Sci. Eng.B* 7 , pp. L1–L4, 1990.
- [36] H.Aono, J.Shinohara, T. Chikata, Y. Hagiwara, "Measuring dynamic strain of a compressor blade," *Proceedings of the SEM Spring Conference on Experimental Mechanics: Las Vegas, Riviera Hotel, June 9–14, Brookfield Center, CT SEM*, 1985, pp.237–243.
- [37] O.S.Heavens, *Thin Film Physics*, Methuen & Co.Ltd, 1970, pp.110–122.
- [38] G.R. Witt, The electromechanical properties of thin films and the thin film strain gauge, *Thin Solid Films* 22 (1974) 133–156.
- [39] Suraj K. Patil, Zeynep Çelik-Butler and Donald P. Butler, "Characterization of MEMS Piezoresistive pressure sensors using AFM," *Ultramicroscopy*, pp. 1-7, 2010.
- [40] Vladimir J. Lumelsky, "Sensitive skin", *IEEE Sensors Journal*, Vol. 1, No. 1, pp. 41-51, June 2001.

- [41] A. Mahmood, D. P. Butler, and Z. Celik-Butler, "Miromachined bolometers on polyimide", *Sensors and Actuators A*, vol. 132, pp. 452-459, 2006.
- [42] Shadi A. Dayeh, Donald P. Butler and Zeynep Celik-Butler, "Micromachined infrared bolometers on flexible polyimide substrates," *Sensors and Actuators A* 118, pp. 49–56, 2005.
- [43] Vinayak Shamanna, Sharmita Das, Z. Celik-Butler, D. P. Butler and Kent L Lawrence, "Micromachined Integrated pressure-thermal sensors on flexible substrates", *Journal of Micromechanics and Microengineering*, 16 (2006).
- [44] Alan J. Surg, "Pare and Prosthetics: The early history of artificial limbs", *proceedings of the 2006 cowlshaw symposium*, 2007, pp. 1114-1119.
- [45] Sumio Iijima, "Helical microtubules of graphitic carbon," *Nature*, vol. 354, pp. 56-58, 1991.
- [46] Vincenzo Lordi, Nan Yao, "Molecular mechanics of binding in carbon-nanotube-polymer composites," *Journal of Materials Research*, vol. 15, pp. 2770-2779, 2000.
- [47] Shailesh Vidhate, Jaycee Chung, Vijay Vaidyanathan, Nandika D'Souza, "Time dependent Piezoresistive behavior of polyvinylidene fluoride/carbon nanotube conductive composite," *Materials Letters*, pp. 1-3, 2009.

BIOGRAPHICAL INFORMATION

Gaviraj Nadvi was born in Chitradurga, India. He received his B.Sc. (2005) in Electronics and Communication Engineering, from the Visvesvaraya Technological University, Belgaum, India. He completed his M.S degree in Electrical Engineering from the University of Texas at Arlington, in August 2010.

His research focused on design, fabrication and characterization of MEMS pressure sensors on flexible substrate. He is interested in MEMS, NEMS and Nanobiotechnology.